

分 类 号 \_\_\_\_\_

学号 \_\_\_\_\_ D201277241 \_\_\_\_\_

学校代码 10487

密级 \_\_\_\_\_

华中科技大学  
博士 学位 论文

太阳能光热梯级发电系统建模  
及其特性研究

学位申请人： 张成

学科专业： 热能工程

指导教师： 高伟 教授

Inmaculada Arauzo 教授

张燕平 副教授

答辩日期： 2018 年 1 月 20 日

A Thesis Submitted in Partial Fulfillment of the  
Requirements for the Ph.D

Cascade solar thermal power system modeling and  
research of the key features

Student : Cheng Zhang

Major : Thermal Engineering

Supervisor : Prof. Wei Gao

Prof. Inmaculada Arauzo

Associate Prof. Yanping Zhang

**Huazhong University of Science & Technology**

**Wuhan 430074, P. R. China**

**January 20, 2018**

## 独创性声明

本人声明所呈交的学位论文是我个人在导师的指导下进行的研究工作及取得的研究成果。尽我所知,除文中已标明引用的内容外,本论文不包含任何其他人或集体已经发表或撰写过的研究成果。对本文的研究做出贡献的个人和集体,均已在文中以明确方式标明。本人完全意识到本声明的法律结果由本人承担。

学位论文作者签名:

日期: 年 月 日

## 学位论文版权使用授权书

本学位论文作者完全了解学校有关保留、使用学位论文的规定,即:学校有权保留并向国家有关部门或机构送交论文的复印件和电子版,允许论文被查阅和借阅。本人授权华中科技大学可以将本学位论文的全部或部分内容编入有关数据库进行检索,可以采用影印、缩印或扫描等复制手段保存和汇编本学位论文。

本论文属于  保密口,在 \_\_\_\_ 年解密后适用本授权书。  
 不保密口。  
(请在以上方框内打“√”)

学位论文作者签名:

日期: 年 月 日

指导教师签名:

日期: 年 月 日

## 摘 要

随着化石能源消耗和环境污染问题的凸显,太阳能被广泛认为是未来最有潜力替代传统化石能源的清洁能源。本文以国家国际合作项目专项“太阳能梯级集热发电系统关键技术合作研究”为背景,目标是研究太阳能光热发电装置,利用各种传统型式的太阳能光热发电系统的优缺点以及热力特性,提出并组建、优化太阳能梯级集热发电系统,为探索出大规模低成本高效率利用太阳能的光热发电技术提供新的方案。主要研究内容包括:

提出了多种采用梯级集热和梯级发电的太阳能光热梯级发电系统。在梯级系统中,采用了多种型式的集热器,实现能量的梯级收集,采用多种形式的热功循环,实现能量的梯级利用。经过系统评估、参数选取、初步计算、方案比较,确定了两种具有代表性的梯级系统方案。

采用 EES、MATLAB 等工具,建立了梯级系统中各部件的机理模型,进而组建了梯级系统。采用面向对象的方法,充分利用了继承、多态等特性,保证了各部件之间既具有独立性又具有关联性。其中,斯特林机的建模过程中,考虑了多种不可逆过程及多类损失,建立了较为完善的斯特林机机理模型,并进行了模型验证分析。结果表明,所建立的斯特林机模型的精度要高于传统的经典斯特林机模型。

研究了太阳能光热梯级发电系统中斯特林机组不同排布方式对系统效率的影响。通过分析斯特林机组的各种不同的排布方式,发现串联连接是最佳的连接型式,斯特林机组具有最佳健壮性和最大的发电效率,梯级发电系统也具有最大的光热发电效率。

提出了分阶段加热的方法,有效降低了蒸汽发生系统中的烟损。在传统蒸汽发生系统的换热过程中,加热流体无相变,被加热流体有相变,两者存在较大的换热温差,换热过程有较大的烟损。本文提出分阶段加热的方法,通过改变加热流体的流量,减小换热温差,降低换热过程的烟损。

提出了太阳能光热梯级发电系统与传统型式太阳能光热发电系统的对比方法。本文针对新型梯级发电系统提出了其与传统型式太阳能光热发电独立系统的对比方法。梯级系统在一定的参数条件下,相比其对应的独立系统,具有更高的总体光电转换效率。

建立了太阳能集热发电试验平台,并开展了相关的试验工作。在相关试验条件下,槽式集热器的热效率在 60.1% 到 62.8% 之间,槽式集热器的热效率在 39.7% 到 63.3% 之间。试验还验证了建立的槽式集热器和碟式集热器模型。

# 华 中 科 技 大 学 博 士 学 位 论 文

---

**关键词：** 槽式集热器, 碟式集热器, 朗肯循环, 斯特林循环, 斯特林机组, 梯级发电

## Abstract

With the increasing awareness of the problem of fossil energy consumption and environmental pollution, solar energy is regarded as the best potential candidate of fossil energy. This research is based on the national cooperation project “Collaborative research on key technologies to produce electricity by cascade utilization solar thermal energy”. The objective of this project is to research the equipment of solar thermal power generation system, to propose, develop and optimize a solar thermal cascade system depending on the advantages and disadvantages of the solar thermal power generation technologies, and to explore a new feasible technology for large-scale solar thermal power generation. The main contents and conclusions of this thesis are as follows:

Multiple topological structures with cascade collection and cascade utilization of the cascade systems were proposed. In these systems, different types of collectors were used for cascade collection and different types of thermodynamic cycles were used for cascade utilization. After system evaluation, parameter selection, preliminary calculation and scheme comparison, two representative typical schemes were determined.

Mechanism models were established for the components of solar thermal power generation system by using EES and MATLAB. The modeling process uses an object-oriented approach, taking full advantage of inheritance, polymorphism and other characteristics, to ensure that each component has both independence and relevance. Among them, the Stirling machine modeling process, considering various irreversibilities and losses, established a more accurate Stirling mechanism model with verification analysis. The results show that the accuracy of the established Stirling model is higher than that of the classical classical Stirling engine models.

The effect of different arrangements of Stirling engines on the efficiency of the cascade system was studied. Through the analysis of different arrangements of Stirling engines, it was found that series connection is the best connection type for the best robustness and maximum efficiency of the Stirling engines, and the largest solar-to-electric efficiency of the cascade system.

A method of multistage heating was proposed, which can effectively reduce the exergy loss of steam generating system. During the entire heat exchange process of a conventional steam generating system, there is no phase change in the heating fluid and there is a phase

change in the heated fluid. There exist large heat transfer temperature differences between the two fluids in the heat exchangers, which makes large entropy production during the heat exchange process. In this thesis, a method of heating in stages is proposed, in which the flow rates of the heating fluid in different heat exchangers are controlled to reduce the heat transfer temperature difference and the exergy losses.

A comparison method of cascade system and traditional solar thermal power generation systems is proposed. In this thesis, corresponding independent systems of the cascade system was proposed for comparison. It is found that the cascade system has a higher overall solar-to-electric conversion efficiency under certain parameters compared to its corresponding independent systems.

A solar thermal power generation test platform was established, and the relevant experimental work was carried out. Under the relevant test conditions, the thermal efficiency of trough collectors is between 60.1% and 62.8%, and that of trough collectors is between 39.7% and 63.3%. The experiment also validated the established trough collector and dish collector models.

**Key words:** parabolic trough collector, parabolic dish collector, Rankine cycle, Stirling cycle, Stirling engine array, cascade solar thermal power

## Contents

|  |            |
|--|------------|
| <b>Abstract</b>                                    | <b>I</b>   |
| <b>List of Figures</b>                             | <b>XII</b> |
| <b>List of Tables</b>                              | <b>XV</b>  |
| <b>1 Introduction</b>                              | <b>1</b>   |
| 1.1 Research background and significance . . . . . | 1          |
| 1.2 State of the art . . . . .                     | 3          |
| 1.3 Literature summary . . . . .                   | 18         |
| 1.4 Research content . . . . .                     | 19         |
| <b>2 System topology</b>                           | <b>21</b>  |
| 2.1 System topology design . . . . .               | 21         |
| 2.2 System topology selection . . . . .            | 30         |
| 2.3 Selected system topology . . . . .             | 37         |
| 2.4 Conclusion . . . . .                           | 39         |
| <b>3 Modeling</b>                                  | <b>40</b>  |
| 3.1 Component modeling . . . . .                   | 40         |
| 3.2 Stirling engine array modeling . . . . .       | 62         |
| 3.3 Steam generating system modeling . . . . .     | 64         |
| 3.4 System modeling . . . . .                      | 66         |
| 3.5 Conclusion . . . . .                           | 68         |
| <b>4 Optimization of Stirling engine array</b>     | <b>69</b>  |
| 4.1 Connection types of SEA . . . . .              | 69         |
| 4.2 Modeling of the SEAs . . . . .                 | 70         |
| 4.3 Result analysis . . . . .                      | 72         |
| 4.4 Conclusion . . . . .                           | 80         |

|  |            |
|--|------------|
| <b>5 Optimization of steam generating system</b>             | <b>81</b>  |
| 5.1 Steam generating subsystem . . . . .                     | 81         |
| 5.2 Multistage exergy loss reduction system . . . . .        | 83         |
| 5.3 Comparison . . . . .                                     | 86         |
| 5.4 Conclusion . . . . .                                     | 89         |
| <b>6 Cascade system performance evaluation</b>               | <b>90</b>  |
| 6.1 System description . . . . .                             | 90         |
| 6.2 System parameters . . . . .                              | 92         |
| 6.3 System evaluation method . . . . .                       | 94         |
| 6.4 Stand-alone system selection . . . . .                   | 96         |
| 6.5 Comparison with stand-alone system . . . . .             | 98         |
| 6.6 Conclusion . . . . .                                     | 103        |
| <b>7 Experiment research on solar thermal power platform</b> | <b>104</b> |
| 7.1 Platform introduction . . . . .                          | 104        |
| 7.2 Experiments . . . . .                                    | 110        |
| 7.3 Result analysis . . . . .                                | 114        |
| 7.4 Conclusion . . . . .                                     | 123        |
| <b>8 Summaries and outlooks</b>                              | <b>124</b> |
| 8.1 Summaries . . . . .                                      | 124        |
| 8.2 Innovations . . . . .                                    | 127        |
| 8.3 Outlooks . . . . .                                       | 128        |
| <b>Acknowledge</b>   | <b>129</b> |
| <b>Bibliography</b>  | <b>131</b> |
| <b>Appendix A Heat transfer under constant temperature</b>   | <b>139</b> |
| <b>Appendix B Thermal gradient under constant heat flux</b>  | <b>141</b> |
| <b>Appendix C MATLAB code of class Stream</b>                | <b>143</b> |
| <b>Appendix D Publication</b>                                | <b>145</b> |

## Nomenclature

|                      |   |
|----------------------|---|
| $\dot{m}$            | Mass flow rate, $\text{kg}\cdot\text{s}^{-1}$   |
| $\overline{d}_{cav}$ | Effective diameter of the cavity, m   |
| $A$                  | Heat transfer area, $\text{m}^2$  |
| $A_{dr,1}$           | Heat transfer area of dish receiver between tube and air, $\text{m}^2$                                  |
| $A_{se,1}$           | Heat transfer area of Stirling engine at air side, $\text{m}^2$   |
| $A_{se,2}$           | Heat transfer area of Stirling engine at water side, $\text{m}^2$                                       |
| $c_p$                | Specific heat at constant pressure, $\text{J}\cdot\text{kg}^{-1}\cdot\text{K}^{-1}$                     |
| $c_r$                | Heat transfer correction factor of coiled tube of volumetric receiver                                   |
| $c_v$                | Specific heat at constant volume, $\text{J}\cdot\text{kg}^{-1}\cdot\text{K}^{-1}$                       |
| $d$                  | Diameter, m   |
| $d_i$                | Inner diameter of trough receiver, m  |
| $dep$                | Depth, m  |
| $e$                  | Regenerator effectiveness   |
| $f$                  | Focal length, m   |
| $J$                  | Annular gap cylinder displacer, m   |
| $K$                  | Dead volume factor  |
| $k$                  | Specific heat ratio ( $c_p/c_v$ ), thermal conductivity, $\text{W}\cdot\text{m}^{-1}\cdot\text{K}^{-1}$ |
| $m$                  | Mass of working fluid in Stirling engine, kg  |
| $n$                  | Number of collectors  |

|          |   |
|----------|---|
| $n_1$    | Number of columns of the Stirling engine array                                    |
| $n_2$    | Number of rows of the Stirling engine array                                       |
| $n_g$    | Amount of working gas in each Stirling engine, mol                                |
| $n_{se}$ | Number of Stirling engines in the Stirling engine array                           |
| $Nu$     | Nusselt number  |
| $P$      | Power of Stirling engine, W   |
| $p$      | Pressure, Pa  |
| $p_e$    | Extraction pressure of the steam turbine, Pa                                      |
| $Pr$     | Prandtl number  |
| $Q$      | Absorbed heat, J  |
| $q''$    | Heat flux, $\text{W}\cdot\text{m}^{-2}$   |
| $R$      | Gas constant, $\text{J}\cdot\text{kg}^{-1}\cdot\text{K}^{-1}$                     |
| $Re$     | Reynolds number   |
| $s_{se}$ | Speed of Stirling engine, Hz  |
| $T_H$    | Working fluid temperature in the hot space, K                                     |
| $T_L$    | Working fluid temperature in the cold space, K                                    |
| $T_R$    | Effective working fluid temperature in regenerator, K                             |
| $T_w$    | Wall temperature, K   |
| $U$      | Overall heat transfer coefficient, $\text{W}\cdot\text{m}^{-2}\cdot\text{K}^{-1}$ |
| $V_C$    | Compression volume, $\text{m}^3$  |
| $V_D$    | Total dead volume, $\text{m}^3$   |
| $V_E$    | Expansion volume, $\text{m}^3$  |

$V_{DC}$  Cold space dead volume, m<sup>3</sup>

$V_{DH}$  Hot space dead volume, m<sup>3</sup>

$V_{DR}$  Regenerator dead volume, m<sup>3</sup>

$W$  Output work, J

$x$  Dryness fraction

$y$  Extraction rate of steam turbine

$Z$  Displacer stroke, m

### Abbreviations

ANN Artificial neural network

CCHP Combined cooling, heating and power

CFD Computational fluid dynamics

CPC Compound parabolic collector

CRTEn Research and technologies centre of energy in Borj Cedria

DSG Direct Steam Generation

HTF Heat Transfer Fluid

ISCC Integrated Solar Combined Cycle

LFC Linear Fresnel Collector

LM Levenberge Marguardt

LSSVM Least squares support vector machine

MCRT Monte Carlo Ray Tracing

ORC Organic Rankine Cycle

PCG Pola-Ribiere Conjugate Gradient

PTC Parabolic Trough Collector

SCG Scaled Conjugate Gradient

SNL Sandia National Laboratory

SRC Steam Rankine Cycle

### Greek Symbols

$\beta$  Ratio of power of Stirling engines to the total output power of cascade system

$\delta$  Thickness, m

$\epsilon$  Emissivity

$\eta_{diff}$  Efficiency difference of cascade system and stand-alone systems,  $\eta_{cs} - \eta_s$

$\eta_{shading}$  Shading factor

$\gamma$  Intercept factor; compression ratio

$\gamma_H$  Space ratio in process 12

$\gamma_L$  Space ratio in process 34

$\lambda$  Thermal conductivity,  $\text{W}\cdot\text{m}^{-1}\cdot\text{K}^{-1}$

$\mu$  Viscosity,  $\text{kg}\cdot\text{m}^{-1}\cdot\text{s}^{-1}$

$\rho$  Reflectivity

$\theta_{dc}$  Dish aperture angle ( $0^\circ$  is horizontal,  $90^\circ$  is vertically down)

### Subscripts

$c$  Cooling fluid; counterflow

$cd$  Condenser

$cs$  Cascade system

$cw$  Cooler wall

华 中 科 技 大 学 博 士 学 位 论 文

---

- g* General solution  
*h* Heating fluid; homogeneous solution  
*hw* Heater wall  
*i* Inlet  
*insu* Insulating layer  
*o* Outlet  
*p* Parallel flow; particular solution; piston  
*pu* Pump  
*r* Regenerator  
*s* Stand-alone systems  
*se* Stirling engine  
*sea* Stirling engine array  
*th* Theoretical  
*w* Tube wall  
*x* Stirling engine in column *x*

## List of Figures

|             |   |    |
|-------------|---|----|
| Figure 1-1  | Examples of the three types of CSP technologies . . . . .                                 | 2  |
| Figure 1-2  | The SG3 400 m <sup>2</sup> dish in Australian National University . . . . .               | 9  |
| Figure 1-3  | Two-stage receiver system . . . . .   | 14 |
| Figure 1-4  | Simplified schematic of a proposed integrated CSP plant configuration . . . . .           | 15 |
| Figure 1-5  | The proposed ISCC scheme . . . . .  | 16 |
| Figure 1-6  | Schematic of the proposed ISCC with two bottoming cycles . . . . .                        | 17 |
| Figure 2-1  | Schematic diagrams of a parabolic trough system and a parabolic dish system . . . . .     | 21 |
| Figure 2-2  | Components in solar power systems . . . . .   | 22 |
| Figure 2-3  | Temperature-entropy diagram of an ideal working fluid . . . . .                           | 23 |
| Figure 2-4  | Schematic diagrams of two types of Rankine cycle solar system .                           | 24 |
| Figure 2-5  | Schematic diagram of a solar chimney power plant . . . . .                                | 26 |
| Figure 2-6  | Schematic diagram of a combined solar trough and chimney power system . . . . .           | 26 |
| Figure 2-7  | Schematic diagram of a cascade system using collector series connection . . . . .         | 27 |
| Figure 2-8  | Schematic diagram of a typical solar trough using DSG . . . . .                           | 28 |
| Figure 2-9  | Schematic diagram of a solar system using air-oil heat exchanger .                        | 28 |
| Figure 2-10 | Schematic diagrams of two kinds of solar systems using air-water heat exchanger . . . . . | 29 |
| Figure 2-11 | Diagram of a typical heat engine . . . . .  | 30 |
| Figure 2-12 | Diagram of three cycles used in solar energy . . . . .                                    | 31 |
| Figure 2-13 | Efficiency variation with operating temperature . . . . .                                 | 31 |
| Figure 2-14 | Schematic diagram of a solar power tower using collector series connection . . . . .      | 34 |
| Figure 2-15 | Schematic diagram of a solar system using air-oil heat exchanger                          | 35 |

|             |   |    |
|-------------|---|----|
| Figure 2-16 | Schematic diagrams of two kinds of solar systems using air-water heat exchanger . . . . . | 35 |
| Figure 2-17 | Two configurations with heat recovery between thermodynamic cycles . . . . .              | 37 |
| Figure 2-18 | Two selected typical cascade systems . . . . .  | 37 |
| Figure 2-19 | A calculation example of cascade system shown in Figure 2-18b .                           | 38 |
| Figure 3-1  | Some of the optical parameters of a parabolic trough . . . . .                            | 42 |
| Figure 3-2  | Schematic diagram of the absorber pipe . . . . .  | 42 |
| Figure 3-3  | The structure of the dish receiver . . . . .  | 44 |
| Figure 3-4  | Thermal network of dish receiver . . . . .  | 45 |
| Figure 3-5  | $T-s$ diagram of a Stirling cycle . . . . .   | 49 |
| Figure 3-6  | $T-s$ diagram of the water circuit and $h-s$ diagram of the process 2a-2b . . . . .       | 58 |
| Figure 3-7  | $T-s$ diagram of water and a typical organic fluid in Rankine cycles                      | 61 |
| Figure 3-8  | The schematic diagram of an ORC system with regenerator . . .                             | 61 |
| Figure 3-9  | Layout of Stirling engines . . . . .  | 62 |
| Figure 3-10 | Heat transfer diagrams of parallel flow and counterflow . . . . .                         | 63 |
| Figure 3-11 | An example of steam generating system in a cascade system . . .                           | 65 |
| Figure 3-12 | The steam generating process . . . . .  | 66 |
| Figure 4-1  | Five basic connection types of SEA . . . . .  | 70 |
| Figure 4-2  | An instance of connection type of an SEA . . . . .  | 71 |
| Figure 4-3  | Flowcharts of the SEA model for performance analysis of the SEAs                          | 73 |
| Figure 4-4  | Influence of $T_{i,h}$ on efficiency and power of SEA . . . . .                           | 75 |
| Figure 4-5  | Influence of $\dot{m}_h c_{p,h}$ on efficiency and power of SEA . . . . .                 | 76 |
| Figure 4-6  | Influence of $\dot{m}_c c_{p,c}$ on efficiency and power of SEA . . . . .                 | 77 |
| Figure 4-7  | Influence of $n_{se}$ on efficiency and power of SEA . . . . .                            | 79 |
| Figure 5-1  | A typical solar parabolic trough system . . . . .   | 81 |
| Figure 5-2  | The steam generating process in counterflow heat exchangers . .                           | 82 |
| Figure 5-3  | The tradeoff to choose $\dot{m}_3$ . . . . .  | 83 |
| Figure 5-4  | Change $\dot{m}_3$ in the heat exchangers to reduce the temperature difference . . . . .  | 84 |

|             |  |     |
|-------------|--|-----|
| Figure 5-5  | The schematic diagram of the MELRS . . . . .   | 84  |
| Figure 5-6  | $T_{3b}$ in the $T$ - $Q$ diagram of the heat transfer processes . . . . .                                 | 88  |
| Figure 6-1  | Sketch of the cascade system . . . . .   | 91  |
| Figure 6-2  | Diagrams of water circuit and $2e-2f$ process . . . . .  | 92  |
| Figure 6-3  | Sketch of the stand-alone systems . . . . .  | 96  |
| Figure 6-4  | Curve fits of efficiency difference $\eta_{diff}$ versus $I_r$ . . . . .                                   | 99  |
| Figure 6-5  | Curve fits of efficiency difference $\eta_{diff}$ versus $\beta$ . . . . .                                 | 100 |
| Figure 6-6  | Parallel flow: Temperature series of two fluids and efficiency of Stirling engines in column $x$ . . . . . | 101 |
| Figure 6-7  | Counterflow: Temperature series of two fluids and efficiency of Stirling engines in column $x$ . . . . .   | 102 |
| Figure 6-8  | Efficiency of Stirling engine array with different $q_{2,m}$ . . . . .                                     | 103 |
| Figure 7-1  | Schematic structure of the platform . . . . .  | 105 |
| Figure 7-2  | Trough collector of the platform . . . . .   | 107 |
| Figure 7-3  | Dish collector of the platform . . . . .   | 108 |
| Figure 7-4  | ORC system of the platform . . . . .   | 109 |
| Figure 7-5  | Control screen of the ORC system . . . . .   | 109 |
| Figure 7-6  | Influence of solar irradiance on the thermal efficiency . . . . .  | 116 |
| Figure 7-7  | Influence of inlet flow rate on the thermal efficiency . . . . .   | 117 |
| Figure 7-8  | Influence of inlet temperature on the thermal efficiency . . . . .   | 118 |
| Figure 7-9  | Influence of solar irradiance on the thermal efficiency . . . . .  | 120 |
| Figure 7-10 | Simulation results of influence of solar irradiance on the thermal efficiency . . . . .                    | 120 |
| Figure 7-11 | Influence of inlet flow rate on the thermal efficiency . . . . .   | 121 |
| Figure 7-12 | Influence of inlet temperature on the thermal efficiency . . . . .   | 122 |
| Figure 1-1  | Diagram of heat transfer under constant temperature . . . . .  | 139 |
| Figure 2-1  | Diagram of heat transfer with one constant temperature heat source and constant heat flux . . . . .        | 141 |

## List of Tables

|           |   |     |
|-----------|---|-----|
| Table 2.1 | Saturated steam pressure at the corresponding temperature . . . . .   | 25  |
| Table 2.2 | Results of SEA models under specified parameters . . . . .  | 33  |
| Table 3.1 | Key parameters of the dish collector . . . . .  | 45  |
| Table 3.2 | Design specifications of the GPU-3 Stirling engine <sup>[1,2]</sup> . . . . .   | 53  |
| Table 3.3 | Thermal efficiency of the models and experimental data (at $T_{hw} = 922\text{ K}$<br>and $T_{cw} = 288\text{ K}$ ) . . . . . | 54  |
| Table 3.4 | Output power of the models and experimental data (at $T_{hw} = 922\text{ K}$<br>and $T_{cw} = 288\text{ K}$ ) . . . . .       | 55  |
| Table 4.1 | Parameters of SEA models . . . . .  | 72  |
| Table 4.2 | Results of SEA models under specified parameters . . . . .  | 74  |
| Table 5.1 | Main parameters used for SGSS and MELRS . . . . .   | 86  |
| Table 5.2 | Simulation results of SGSS and MELRS . . . . .  | 87  |
| Table 6.1 | Main parameters of LS-3 . . . . .   | 93  |
| Table 6.2 | Basic design parameters of the cascade system . . . . .   | 95  |
| Table 6.3 | Some important results using design parameters . . . . .  | 98  |
| Table 6.4 | Results of Stirling engine array with two different flow types . . .  | 101 |
| Table 7.1 | Key parameters of the designed dish collector . . . . .   | 106 |
| Table 7.2 | Designed cases of the solar trough system . . . . .   | 111 |
| Table 7.3 | Designed cases of the solar dish system . . . . .   | 114 |
| Table 7.4 | Experiment results of Case 1 to Case 10 of the trough collector . .   | 115 |
| Table 7.5 | Experiment results of Case 11 to Case 15 of the trough collector .  | 116 |
| Table 7.6 | Experiment results of Case 16 to Case 20 of the trough collector .  | 117 |
| Table 7.7 | Experiment results of Case 1 to Case 10 of the dish collector . . .   | 119 |
| Table 7.8 | Experiment results of Case 11 to Case 15 of the dish collector . .  | 121 |
| Table 7.9 | Experiment results of Case 16 to Case 20 of the dish collector . .  | 122 |

## Chapter 1 Introduction

### 1.1 Research background and significance

Renewables are now established around the world as mainstream sources of energy. Rapid growth, particularly in the power sector, is driven by several factors, including the improving cost-competitiveness of renewable technologies, dedicated policy initiatives, better access to financing, energy security and environmental concerns, growing demand for energy in developing and emerging economies, and the need for access to modern energy.

Solar energy, which has the advantages of widely distribution, huge amount, inexhaustible and no pollution, has received much attention by many countries and been regarded as the best potential candidate of the fossil energy. The International Energy Agency projected in 2014 that under its “high renewables” scenario, by 2050, solar photovoltaics and concentrating solar thermal power would contribute about 16 and 11 percent, respectively, of the worldwide electricity consumption, and solar would be the world’s largest source of electricity.<sup>[3]</sup>

Concentrating solar thermal power generation is another form of power generation technology except solar photovoltaic power generation. Concentrating Solar Power (CSP) system uses mirrors to converge sunlight onto a receiver that absorbs the solar energy and transfer it to a heat transfer fluid (HTF) such as a synthetic oil, molten salt or air. The HTF then directly or indirectly used as the heat source in a power cycle. Compared to solar photovoltaic, solar thermal power is gaining more attention for its advantages as higher energy density, smooth power generation, good grid compatibility, easy to integrate with existing fossil power plant.

Concentrating solar power technologies use different mirror configurations to concentrate the sun’s light energy onto a receiver and convert it into heat. The heat is collected for power generation or used as industrial process heat. There are three types of CSP technologies being commercially applied: parabolic trough, parabolic dish and power tower. Figure 1-1 shows examples of the three types of CSP technologies.

A parabolic trough is a type of solar thermal collector whose mirror type is straight in one dimension and curved as a parabola in the other two. The reflector follows the sun during the daylight hours by tracking along a single axis. The energy of sunlight is reflected by the



Parabolic trough



Parabolic dish



Power tower

Figure 1-1 Examples of the three types of CSP technologies

mirror and focused on the pipe positioned at the focal line. HTF (e.g. synthetic oil) runs through the pipe to absorb the heat generated by the focused sunlight, then used as the heat source for power generation or heating process.

A parabolic dish is a type of solar thermal collector whose mirror type is part of a circular paraboloid, which can converge the incoming sunlight traveling along the axis to the focus. Two-axis tracking system keeps it always directly towards the sun without cosine loss. It can obtain high concentration ratio and hence high temperature. Typically, a receiver or a Stirling engine is put at the focal point to absorb the converged energy.

Solar power tower is a type of solar furnace using a tower to receive the focused sunlight.

It uses an array of flat, movable mirrors (called heliostats) to focus the sun's rays upon a collector tower. The heliostats track the sun on two axes (east to west and up and down). The receiver absorbs concentrated solar radiation and converts the solar energy into heat. The heat is then transferred to an HTF that carries the heat to a thermodynamic cycle for power generation.

Among the three solar thermal power technologies, parabolic trough is the most mature and commercially deployed technology. However, it has a low concentration ratio, the receiver's temperature is relatively low, the solar-to-electric efficiency is relatively low. Parabolic dish can obtain high temperature thermal energy, its solar-to-electric efficiency is higher than parabolic trough. Besides, one advantage of parabolic dish is that it requires much less water for power generation. However, solar parabolic dish is not a large-scale application, it's mainly applied for distributed power generation for its compact structure and easy installation. Solar power tower has a very high concentration ratio when more heliostats are used, the receiver's temperature can be very high and it can be applied for large-scale application. However, it has some disadvantages such as high investment and high system complexity. It is currently in rapid development stage.

It is very important to find out a way to utilize the advantages of existing solar thermal power technologies and overcome their disadvantages. In other words, to find out a new technology with higher efficiency and lower cost is urgent. This research is trying to achieve this by proposing a cascade system that uses different solar collectors and different thermodynamic cycles, which may be a new and feasible technology to realize large-scale, higher efficiency and lower cost solar thermal power generation.

## 1.2 State of the art

Solar thermal power technologies are getting more and more attention. Many researchers have done lots of work to research and investigate it to increase its performance or reduce its cost.

### 1.2.1 Parabolic trough

Parabolic trough solar technology is the most proven and lowest cost large-scale solar power technology available.<sup>[4]</sup>

Many of these works have concentrated on experimental work aimed at testing the mechanical and thermal performance of parabolic trough collectors. Dudley et al.<sup>[5]</sup> tested the collector efficiency and thermal losses of the LS-2 type trough collector. Burkholder and Kutscher<sup>[6]</sup> tested the heat losses of Solel's UVAC3 and Schott's 2008 PTR70 parabolic trough collectors. A correlation to estimate the thermal efficiency of the collectors as a function of the absorber temperature was developed. Reddy et al.<sup>[7]</sup> developed and investigated six different receiver configurations of trough collectors for performance comparison. Experimental tests were carried out for a 15 m<sup>2</sup> collector according to ASHRAE 93-1986 test procedure. Li et al.<sup>[8]</sup> carried out experiments to verify the feasibility of proposed end loss compensation methods. A fan-shaped plane mirror was put at one end of the trough collectors to compensate the end loss effect. Results prove that the compensation methods are feasible and effective. It is well known that experimental studies are the most accurate and convincing method for parabolic trough collector research. However, this method is not only investment required and also time consuming. In order to reduce the R&D cost and time, parabolic trough collectors are usually modeled.

Some researchers investigated the optical model of the parabolic trough solar collectors. Wang et al.<sup>[9]</sup> proposed a mathematical model for optical efficiency of the trough collector and selected three typical regions of solar thermal utilization in China for the model. The model is validated by comparing the test results in parabolic trough power plant, with relative error range of 1% to about 5%. Zou et al.<sup>[10]</sup> investigated the influences of sunshape and incident angle on the optical performance of the trough collectors. It is found that the sunshape has significant effect on the optical efficiency and should be taken into consideration in practice. Larger aperture with smaller absorber diameter leads to more end loss caused by incident angle. It is also found that optimal focal length exists for the optical efficiency. Lüpfert et al.<sup>[11]</sup> introduced the specific techniques to analyze the geometry and optical properties of trough collectors and summarized results in collector shape measurement, flux measurement, ray tracing, and thermal performance analysis for parabolic troughs. It is shown that the measurement methods and the parameter analysis give consistent results, which can provide references for the next generation trough collector relevant improvements. Xu et al.<sup>[12]</sup> analyzed the optical efficiency of a PTC with horizontal north-south axis and proposed a method to compensate the end loss effect of the PTC. The calculation formula of the optical end loss rate and the increased optical efficiency for the system using the compensation

method were derived. A five-meter experimental system was built to verify the feasibility of the compensation method proposed. The increased thermal efficiency of the experimental system was measured, and it was proved that the proposed compensation method is feasible. Huang et al.<sup>[13]</sup> proposed an analytical model for optical performance which employed a modified integration algorithm to simulate the performance of trough collectors. The analytical equation of the optical efficiency of each point of the reflector was deduced to obtain the optical efficiency of the system by integration algorithm.

Some researchers investigated the exergy performance of the parabolic trough collectors. Padilla et al.<sup>[14]</sup> performed a comprehensive exergy balance of a parabolic trough collector based on the previous heat transfer model<sup>[15]</sup>. The results shown that inlet temperature of heat transfer fluid, solar irradiance, and vacuum in annulus have a significant effect on the thermal and exergetic performance, but the effect of wind speed and mass flow rate of heat transfer fluid is negligible. It was obtained that inlet temperature of heat transfer fluid cannot be optimized to achieve simultaneously maximum thermal and exergetic efficiency because they exhibit opposite trends. Finally, it was found that the highest exergy destruction is due to the heat transfer between the sun and the absorber while for exergy losses is due to optical error. Guo et al.<sup>[16]</sup> investigated the energy efficiency and exergy efficiency of the parabolic trough collector. The result shown that there exists an optimal mass flow rate of working fluid for exergy efficiency, and the thermal efficiency and exergy efficiency have opposite changing tendencies under some conditions.

Some researchers are dedicated to developing more accurate models using new methods. Behar et al.<sup>[17]</sup> developed and validated a novel parabolic trough solar collector model. The model has been compared with models made by Lab. SNL and NREL. The proposed model has a better accuracy of thermal performance prediction. Padilla et al.<sup>[15]</sup> performed a detailed one dimensional numerical heat transfer analysis of a PTC (Parabolic Trough Collector). To solve the mathematical model of heat transfer of the PTC model, the partial differential equations were discretized and the nonlinear algebraic equations were solved simultaneously. The numerical results was validated to the data from Sandia National Laboratory (SNL). Hachicha et al.<sup>[18]</sup> presented a detailed numerical heat transfer model based on the finite volume method for the parabolic trough collector. This model is based on finite volume method and ray trace techniques and takes into account the size of the Sun. The model is thoroughly validated with results from the literature and it shows a good agreement

with experimental and analytical results. Guo and Huai<sup>[19]</sup> implemented a multi-parameter optimization of parabolic trough solar receiver based on genetic algorithm where Exergy and thermal efficiencies were employed as objective function. Boukelia et al.<sup>[20]</sup> investigated the feed-forward back-propagation learning algorithm with three different variants; Levenberge Marguardt (LM), Scaled Conjugate Gradient (SCG), and Pola-Ribiere Conjugate Gradient (PCG), used in artificial neural network (ANN) to find the best approach for prediction and techno-economic optimization of parabolic trough solar thermal power plant integrated with fuel backup system and thermal energy storage. Liu et al.<sup>[21]</sup> developed a mathematical model of PTC using the least squares support vector machine (LSSVM) method. Numerical simulations were implemented to evaluate the feasibility and efficiency of the LSSVM method, where the sample data derived from the experiment and the simulation results of two solar collector systems with 30 m<sup>2</sup> and 600 m<sup>2</sup> solar fields, and the complicated relationship between the solar collector efficiency and the solar flux, the flow rate and the inlet temperature of the heat transfer fluid (HTF) is extracted. Lobon et al.<sup>[22]</sup> introduced a computational fluid dynamic simulation approach to predict the behavior of a solar steam generating system, which is located at the Plataforma Solar de Almeria, Spain. The CFD package STAR-CCM+ code has been used to implement an efficient multiphase model capable of simulating the dynamics of the multiphase fluid in parabolic-trough solar collectors. Numerical and experimental data are compared in a wide range of working conditions. To understand the thermal performance of the collector and identify the heat losses, Mohamad et al.<sup>[23]</sup> analyzed the temperature variation of the working fluid, tube and glass along the collector. It is found that using double glazing cover enhances the thermal efficiency of the collector operating at high temperature. However, when the collector length is 10 m or less, it is more economical to use a single glass cover for the collector than a double glazing cover. Also, it is clearly shown that increasing the diameter of absorbing tube enhances the rate of heat transfer losses, consequently decreasing the thermal efficiency of the collector. Guo et al.<sup>[24]</sup> developed a nonlinear distribution parameter model to model the dynamic behaviors of direct steam generation parabolic trough collector loops under either full or partial solar irradiance disturbance.

Some researchers have proposed some new types of solar trough systems. Ashouri et al.<sup>[25]</sup> coupled a small scale parabolic trough collector and a thermal storage tank along with an auxiliary heater to a Kalina cycle to study the performance of the system throughout

the year, both thermodynamically and economically. Bader et al.<sup>[26]</sup> developed a numerical model of a tubular cavity-receiver that uses air as the heat transfer fluid. Four different receiver configurations are considered, with smooth or V-corrugated absorber tube and single- or double-glazed aperture window. The different types of energy loss by the collector have been quantified, and the temperature distribution inside the receiver has been studied. The pumping power required to pump the HTF through the receiver has been determined for a 200 m long collector row. Good et al.<sup>[27]</sup> proposed solar trough concentrators using air as heat transfer fluid at operating temperatures exceeding 600°C. It consists of an array of helically coiled absorber tubes contained side-by-side within an insulated groove having a rectangular windowed opening. Secondary concentrating optics are incorporated to boost the geometric concentration ratio to 97×. Kaloudis et al.<sup>[28]</sup> investigated a PTC system with nanofluid as the HTF in terms of Computational Fluid Dynamics (CFD). Syltherm 800 liquid oil was used as the HTF, and Al<sub>2</sub>O<sub>3</sub> nanoparticles with the concentrations ranges from 0% to 4% was investigated. A boost up to 10% on the collector efficiency was reported for Al<sub>2</sub>O<sub>3</sub> concentration of 4%. Al-Sulaiman et al.<sup>[29]</sup> proposed a novel system based on PTC and ORC for combined cooling, heating and power (CCHP). Performance assessment, including efficiency, net electrical power, and electrical to heating and cooling ratios, of the system shown that when CCHP is used, the efficiency increases significantly. This study reveals that the maximum electrical efficiency for the solar mode is 15%, for the solar and storage mode is 7%, and for the storage mode is 6.5%. The maximum CCHP efficiency for the solar mode is 94%, for the solar and storage mode is 47%, and for the storage mode is 42%.

### 1.2.2 Parabolic dish

The solar parabolic dish system is known for its highest efficiency of all solar technologies (around 30%). It is suitable for distributed power generation for its compact structure and easy installation.

Many researchers conducted experiments to investigate the solar parabolic dish system or to validate proposed models. To investigate the heat loss of semi-spherical cavity receiver applied for solar parabolic dish system, Tan et al.<sup>[30]</sup> conducted experiments with different fluid inlet temperatures, receiver inclination angles and aperture sizes. Correlations of Nusselt number as a function of Grashof number were developed by the experiment results. Chaudhary et al.<sup>[31]</sup> investigated a solar cooker based on dish collector with phase change

thermal (PCM) storage unit. Three cases have been considered for the investigation: ordinary solar cooker, solar cooker with outer surface painted black, and solar cooker with outer surface painted black along with glazing. It was observed that the last case shows the best performance, which can store 32.3% and 26.8% more heat for the PCM compared with the first and second cases respectively. Mawire and Taole<sup>[32]</sup> investigated the thermal performance of a cylindrical cavity receiver for an SK-14 parabolic dish concentrator. The receiver exergy rates and efficiencies are found to be appreciably smaller than the receiver energy rates and efficiencies. The exergy factor is found to be high under conditions of high solar radiation and high operating temperatures. An optical efficiency of around 52% for parabolic dish system is determined under high solar radiation conditions. Zhu et al.<sup>[33]</sup> conducted an experimental investigation of a coil type solar dish receiver. The solar irradiance is about 650 W/m<sup>2</sup>, while the concentrated solar flux at the aperture is approximately 1000 kW/m<sup>2</sup>. The energy and exergy performance of the receiver was analyzed and the experimental results show that, at steady state, the energy efficiency is maintained around 80%, and the exergy efficiency is around 28%. CRTEn developed a solar dish system using four types of absorbers: flat plat, disk, water calorimeter and solar heat exchanger.<sup>[34]</sup> For the different types of absorbers, experiments were conducted to obtain the mean concentration ratio and both energy and exergy efficiency. Results shown that thermal energy efficiency of the system varies from 40% to 77%, the concentrating system reaches an average exergy efficiency of 50% and a concentration factor around 178. Thirunavukkarasu et al.<sup>[35]</sup> carried out an experimental study to investigate the thermal performance of a cavity receiver for a dish concentrator. The overall system efficiency of the solar collector is 69.47%. The average exergy efficiency of the receiver is found to be 5.88% with a peak value of 10.35%. Pavlovic et al.<sup>[36]</sup> performed the experimental study of a solar dish system. In this system, different working fluids (water, thermal oil and air) were used to validate the numerical models developed in EES (Engineering Equation Solver). It was found that water is the most appropriate working fluid for low-temperature applications, while thermal oil is the most appropriate working fluid for higher-temperature applications.

Some researchers focused on the dish concentrator, many proposed different shapes of concentrators. The perfect concentrator has a parabolic shape, but for some considerations (better production, safer transportation, less cost and so on), some solar concentrators are composed of multiple spherically shaped mirrors. A large dish solar concentrator, SG3,

which is about  $400 \text{ m}^2$ , was designed and demonstrated in Australian National University in 1994 as shown in Figure 1-2.<sup>[37]</sup> It successfully proved the technical viability of a concentrator that is approximately three times bigger than any other produced. Berumen et al.<sup>[38]</sup>

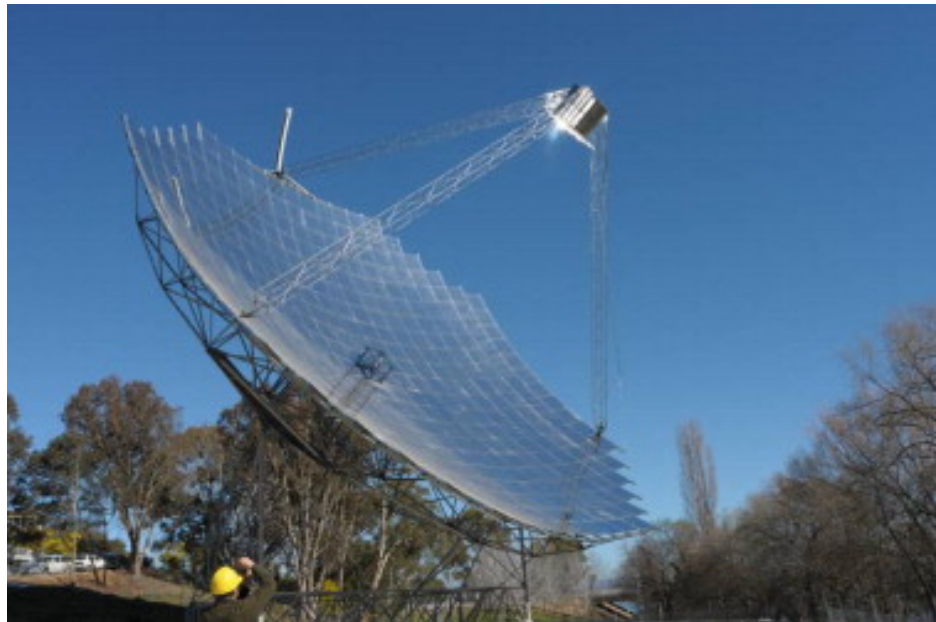


Figure 1-2 The SG3  $400 \text{ m}^2$  dish in Australian National University

developed a reflector consists of 12 facets made of fiberglass with a reflecting surface made of aluminum sheet with reflectance of 86%. Pavlovic et al.<sup>[39]</sup> presented a procedure to design a square facet concentrator for laboratory-scale research on medium-temperature thermal processes. A parabolic collector made up of individual square mirror panels (facets) were investigated. These facets can deliver up to 13.604 kW radiative power over a 250 mm radius dish receiver with average concentrating ratio exceeding 1200. Hijazi et al.<sup>[40]</sup> designed a low cost parabolic solar dish concentrator with small-to moderate size for direct electricity generation and special attention is given to the selection of the appropriate dimensions of the reflecting surfaces. Ma et al.<sup>[41]</sup> designed a solar dish concentrator based on triangular membrane facets. A 600-facet concentrator with focal-diameter ratio of 1.1 will achieve 83.63% of radiative collection efficiency over a 15 cm radius disk located in the focal plane, with a mean solar concentration ratio exceeding 300. A 3.6-meter diameter stretched-membrane optical facet for a parabolic dish has been successfully designed and demonstrated under contract with Sandia National Laboratories.<sup>[42]</sup> Twelve facets identical to them will be used

to make the lightweight reflector of the dish. The project goal of 2.5 mrad surface accuracy was met with each of the two full-sized prototypes, and accuracies of as low as 1.1 mrad were achieved.

Many researches investigated the flux distribution and thermal performance of the solar dish receiver. Shuai et al.<sup>[43]</sup> developed a flux distribution measurement system for dish concentrators. A charge coupled device camera was applied to obtain the contours of the flux distribution for target placements with different location. Further, the measured flux distributions are compared with a Monte Carlo-predicted distribution. The results can be a valuable reference for the design and assemblage of the solar collector system. Mao et al.<sup>[44]</sup> simulated the flux distribution of a dish receiver using MCRT method. The impacts of incident solar irradiation, aspect ratio (the ratio of the receiver height to the receiver diameter), and system error on the radiation flux of the receiver are investigated. Li et al.<sup>[45]</sup> used the Monte-Carlo ray-tracing method for the radiation flux distribution of the solar dish receiver system. The result was validated by experiment and used as the boundary conditions of a CFD receiver model. The fluid flow and conjugate heat transfer in the receiver was numerically simulated and validated by experiments. Wang and Laumert<sup>[46]</sup> used the ray-tracing methodology to investigate the effects of cavity surface materials on the flux distribution for an impinging receiver. Five cavity surface materials and their combinations have been studied. The results show that the flux distribution and the total optical efficiency are much more sensitive to the absorptivity on the cylindrical surface than on the bottom. Blazquez et al.<sup>[47]</sup> studied the optimization of the concentrator and receiver cavity geometry of parabolic dish system. Ray-tracing analysis has been performed with the open source software Tonatiuh, a ray-tracing tool specifically oriented to the modeling of solar concentrators. Reddy et al.<sup>[7,48]</sup> performed the theoretical thermal performance analysis of a fuzzy focal solar parabolic dish concentrator with modified cavity receiver. Total heat loss from the modified cavity receiver was estimated considering the effects of wind conditions, operating temperature, emissivity of cavity cover and thickness of insulation. Time constant test was carried out to determine the influence of sudden change in solar radiation at steady state conditions. The daily performance tests were conducted for different flow rates. Vikram and Reddy<sup>[49]</sup> used a three-dimensional numerical model to investigate the total heat losses of three modified cavity with three configurations for parabolic dish receiver. The effects of cavity diameter ratio, tilt angle, operating temperature, insulation thickness and emissivity on the heat loss of the

modified cavity receiver were studied. Based on artificial neural network (ANN) modeling, an improved Nusselt number correlation was proposed for convection, radiation and total heat loss calculation.

Some researchers focused on the solar tracking system. Patil et al.<sup>[50]</sup> described the development of automatic dual axis solar tracking system for solar parabolic dish. Five light dependent resistors were used to sense the sunlight and two permanent magnet DC motors are used to move the solar dish. A controller software were developed to control the motors using the data sensed by the resistors. Raturi et al.<sup>[51]</sup> proposed a solar tracking system based on gravity which does not require any external source of power. The prototype test results and analysis show that the system can run successfully. Kuang and Zhang<sup>[52]</sup> developed new design and implementation of tracking system to improve tracking accuracy for dish solar based on embedded system that mixes active and passive tracking. Jin et al.<sup>[53]</sup> described a two-axis sun tracking system with PLC (programmable logic controller) controlled and a combinative tracking method combined active and passive tracking methods for higher accuracy. Shanmugam and Christraj<sup>[54]</sup> presented a method of intermittent tracking of the sun in the north-south direction with no tracking in the east-west direction for less energy yield and the frequency of tracking in the north-south direction determined by variations in solar altitude angle and size of the absorber in paraboloidal dish concentrator.

### 1.2.3 Power tower

Solar power tower technology is gaining more and more interest for its large scale, high concentration ratio and high operating temperature. It is widely regarded as the most promising solar thermal power technology.

Advances in the power tower technology are mainly the component update as well as system improvement. Some researchers focused on the choice of HTF that used in the power tower. One already standardized commercial plant cycle is the solar tower with conventional steam cycle.<sup>[55]</sup> Steam is used as both HTF and working fluid in the Rankine cycle. Steam is directly generated in the receiver and flows into the steam turbine for power generation.<sup>[56–60]</sup> Many researchers concerned about using other fluids (molten salt, air) as HTF. Toto et al.<sup>[61]</sup> proposed an idea of a hybrid power tower using air as the working fluid of a topping Brayton cycle and HTF of a bottoming Rankine cycle. Rold<sup>[62]</sup> proposed an idea of using supercritical CO<sub>2</sub> as HTF. A simplified CFD model has been built to analyze the feasibility of supercritical

$\text{CO}_2$  as HTF in solar towers. It was found that it is a promising alternative for both better operating conditions and lower maintenance cost. Joshi et al.<sup>[63]</sup> used the dynamic simulation technology to evaluate a molten salt central receiver design and control strategies.

Many researchers concerned about the heliostats to reach high tracking accuracies under wind loads and thermal stress situations. On the other hand, trade-off between higher land utilization and lower block ratio is also a hot spot. Thalange et al.<sup>[64]</sup> presented the protocol and results of systematic structural analysis of tripod heliostats to reduce the cost and enhance the mechanical behavior. Besarati and Yogi<sup>[65]</sup> developed a new and simple method to improve the calculation speed and accuracy for shading and blocking computation of the heliostat field. The Sassi method<sup>[66]</sup> is used for the shading and blocking efficiency. A 50 MWth heliostat field in Daggett, California, USA was used as a case study for the proposed method. Wei et al.<sup>[67]</sup> proposed a new method for the design of the heliostat field layout for solar tower power plant. Based on the new method, a new code for heliostat field layout design (HFLD) has been developed and a new heliostat field layout for the PS10 plant at the PS10 location has been designed using the new code. Compared with current PS10 layout, the new designed heliostats has the same optical efficiency but with a faster response speed.

Some researchers concerned about the performance of central receiver of power tower. Kim et al.<sup>[68]</sup> investigated the heat loss of solar central receiver. Numerical simulations using CFD (Computational Fluid Dynamics) with the consideration of four different receiver shapes were carried out to get the influence on convection and radiation heat losses. Different opening ratio between cavity aperture area and receiver aperture area, receiver temperatures, wind velocities and wind directions (head-on and side-on) were considered for the simulations. Results were used to get a simplified correlation model which gets the fraction of convection heat loss. The correlation obtained shows good agreements with the simulation results. The correlation was also validated with experimental data from three central receiver systems (Martin Marietta, Solar One and Solar Two). Lara et al.<sup>[69]</sup> presented a novel modeling tool for calculation of central receiver concentrated flux distributions. The modeling tool is based on a drift model that includes different geometrical error sources in a rigorous manner and on a simple analytic approximation for the individual flux distribution of a heliostat.

Some researchers devoted on the simulation of power tower plants. Franchini et al.<sup>[70]</sup> developed a computing procedure for solar tower system under both nominal and part load

conditions. A Siemens gas turbine product, SGT-800, was applied for the Integrated Solar Combined Cycle (ISCC) as a study case for the solar tower system. The turbine has a dual pressure heat recovery steam generator, which can be used for the Integrated Solar Combined ISCC plant. A model of Solar Rankine Cycle (SRC) driven by power tower was also developed for comparison. A highest solar-to-electric efficiency of 21.8% can be achieved by the designed ISCC plant. And in all conditions, the global solar energy conversion efficiency of the ISCC is higher than that of the SRC. Xu et al.<sup>[71,72]</sup> created a model of the 1 MW Dahan solar thermal power tower plant using the modular modeling method. The dynamic and static characteristics of the power plant are analyzed based on these models. Response curves of the system state parameters are given for different solar irradiance disturbances. Conclusions in this paper are good references for the design of solar thermal power tower plant. Benamar et al.<sup>[73]</sup> developed a mathematical model based on energy analysis for solar tower power plants. A general nonlinear mathematical model of the studied system has been presented and solved using numerical optimization methods. The analysis of these results shows the existence of an optimal receiver efficiency value for each steam mass flow, receiver surface temperature and receiver surface area.

### 1.2.4 Cascade solar system

To fully utilize the features of components of solar thermal power system, cascade solar systems are researched by many researchers. There are mainly two directions of the research of cascade solar systems. One is cascade collection, the other is cascade utilization.

#### 1.2.4.1 Cascade collection

Some researchers have investigated the combination of different types of collectors for CSP to achieve cascade solar collection. Suzuki<sup>[74]</sup> analyzed the solar thermal systems with two different types of collectors connected in series. A value of the collectors, the product of the collector efficiency factor and the optical efficiency, was revealed to be the key factor to determine whether a cascade system is better than either one of the collectors alone. If the value of the lower concentration ratio collector is larger than that of the higher concentration ratio, the cascade system is more effective. Furthermore, it was found that to obtain the maximum energy gain, there exists the optimum operating conditions.

Kribus et al.<sup>[75]</sup> proposed an idea of using separate aperture stages for different irradia-

ance distribution. The working fluid is gradually heated when it flows through the receiver elements with increasing irradiance levels. A two-stage system was set up to demonstrate this principle at the Weizmann Institute's Solar Tower. Air was used as the HTF to obtain 750°C after the low-temperature stage and 1000°C after the high-temperature stage. Figure 1-3 shows the two-stage receiver system.

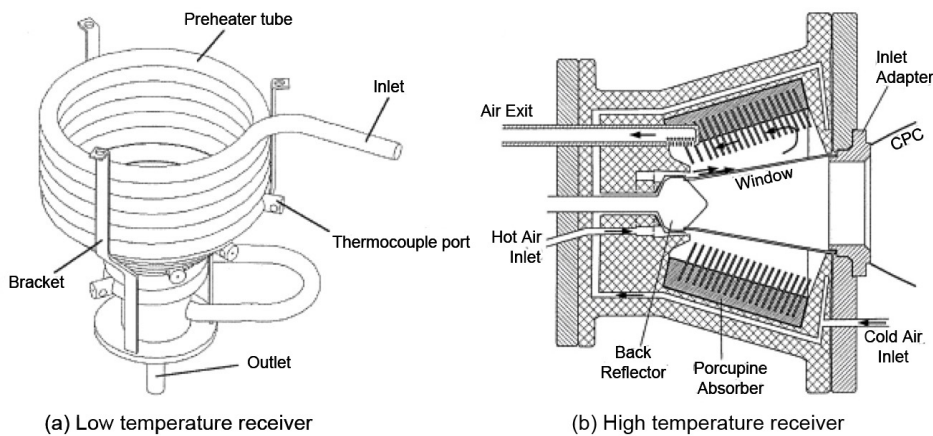


Figure 1-3 Two-stage receiver system

Gordon and Saltiel<sup>[76]</sup> presented an analytic method for predicting the long-term performance of solar energy systems with more than one collector brand (“multistage” systems). This procedure enables the designer to determine the most cost-effective method of combining different collector brands for a given load. The analytic method is illustrated by a solved example which shows that significant savings can be realized by combining different collector brands for a given application (multi-staging).

Oshida and Suzuki<sup>[77]</sup> presented the idea of optical cascade heat collection of solar energy. Two absorbers, one warm and the other hot, are used in the cascade system. The warm absorber is heated by the Fresnel lenses and the hot absorber is heated by CPC. HTF flows into the warm absorber firstly and then flows into the hot absorber. The temperature of HTF can increase more effectively by the cascade heating design.

Desai et al.<sup>[78]</sup> presented an integrated CSP plant configuration with the combination of both PTC and LFC. Thermo-economic comparisons between PTC-based, LFC-based and integrated CSP plant configurations, without hybridization and storage, were analyzed. Figure 1-4 shows a simplified schematic of a proposed integrated CSP plant configuration. It is demonstrated that the cost of energy of an integrated CSP plant is 9.6% cheaper than PTC-

based CSP plant and 13.5% cheaper than LFC-based CSP plant.

Coco et al.<sup>[79]</sup> developed four different line-focusing solar power plant configurations integrated both direct steam generation and Brayton power cycle. In these configurations, collectors are divided into different solar fields to supply different heat demands. This provides the ability to use different types of collectors (parabolic trough and linear Fresnel) in the systems.

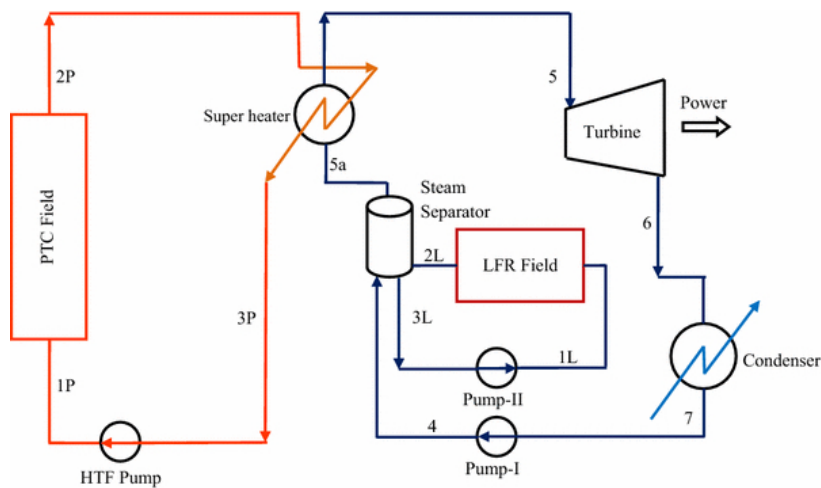


Figure 1-4 Simplified schematic of a proposed integrated CSP plant configuration

#### 1.2.4.2 Cascade utilization

Many researchers have done the work on the combination of different thermodynamic cycles for CSP. Lots of the work focused on integrated solar combined cycle (ISCC) with parabolic trough, where Rankine cycle is used as the bottom cycle.

Li and Yang<sup>[80]</sup> proposed a novel two-stage ISCC system that could reach up to 30% of the net solar-to-electricity efficiency as shown in Figure 1-5. In their research, the impact on the system overall efficiencies of how and where solar energy is input into ISCC system was investigated.

Gülen<sup>[81]</sup> used the exergy concept of the second law of thermodynamics to simplify the optimization process of ISCCS. After the exergy analysis, physics-based, user-friendly guidelines were provided for ISCC designs.

Shaaban<sup>[82]</sup> introduced a novel ISCC with steam and organic Rankine cycles. The ORC was used in order to intercool the compressed air and produce a net power from the received

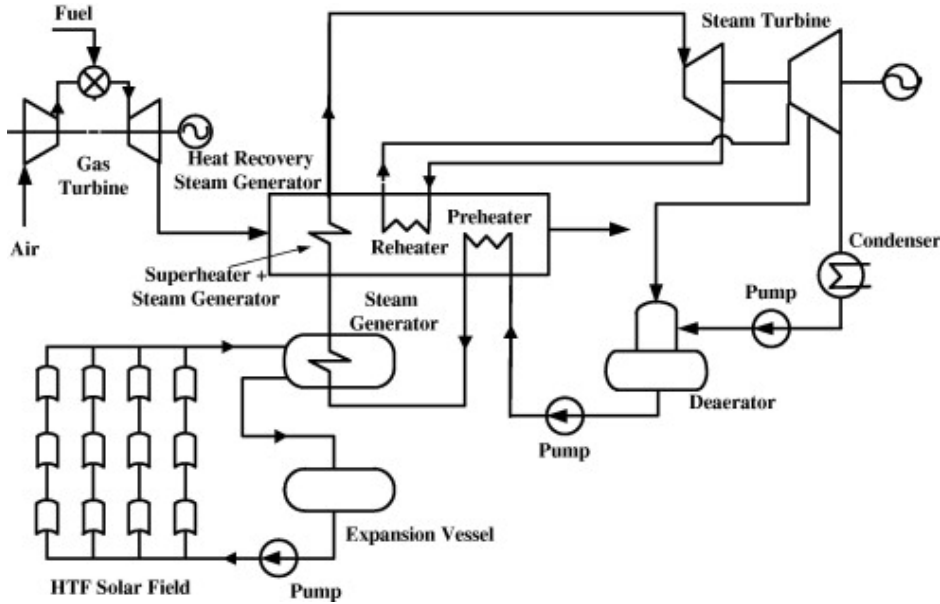


Figure 1-5 The proposed ISCC scheme

thermal energy. The proposed cycle performance was studied and optimized with different ORC working fluids. Figure 1-6 shows the schematic of the proposed ISCC.

Alqahtani and Dalia<sup>[83]</sup> quantified the economic and environmental benefits of an ISCC power plant relative to a stand-alone CSP with energy storage, and a natural gas-fired combined cycle plant. Results show that integrating the CSP into an ISCC reduces the LCOE of solar-generated electricity by 35-40% relative to a stand-alone CSP plant, and provides the additional benefit of dispatch ability.

Manente<sup>[84]</sup> developed a 390 MWe three pressure level natural gas combined cycle to evaluate different integration schemes of ISCC. Both power boosting and fuel saving operation strategies were analyzed in the search for the highest annual efficiency and solar share. Result shown that, compared to power boosting, the fuel saving strategy shows lower thermal efficiencies of the integrated solar combined cycle due to the efficiency drop of gas turbine at reduced loads.

Turchi et al.<sup>[85]</sup> represented two new conceptual hybrid designs for ISCC with parabolic trough. In the first design, gas turbine waste heat is supplied for both heat transfer fluid heating and feed water preheating. In the second design, gas turbine waste heat is supplied for a thermal energy storage system.

Mukhopadhyay and Ghosh<sup>[86]</sup> presented a conceptual configuration of a solar power

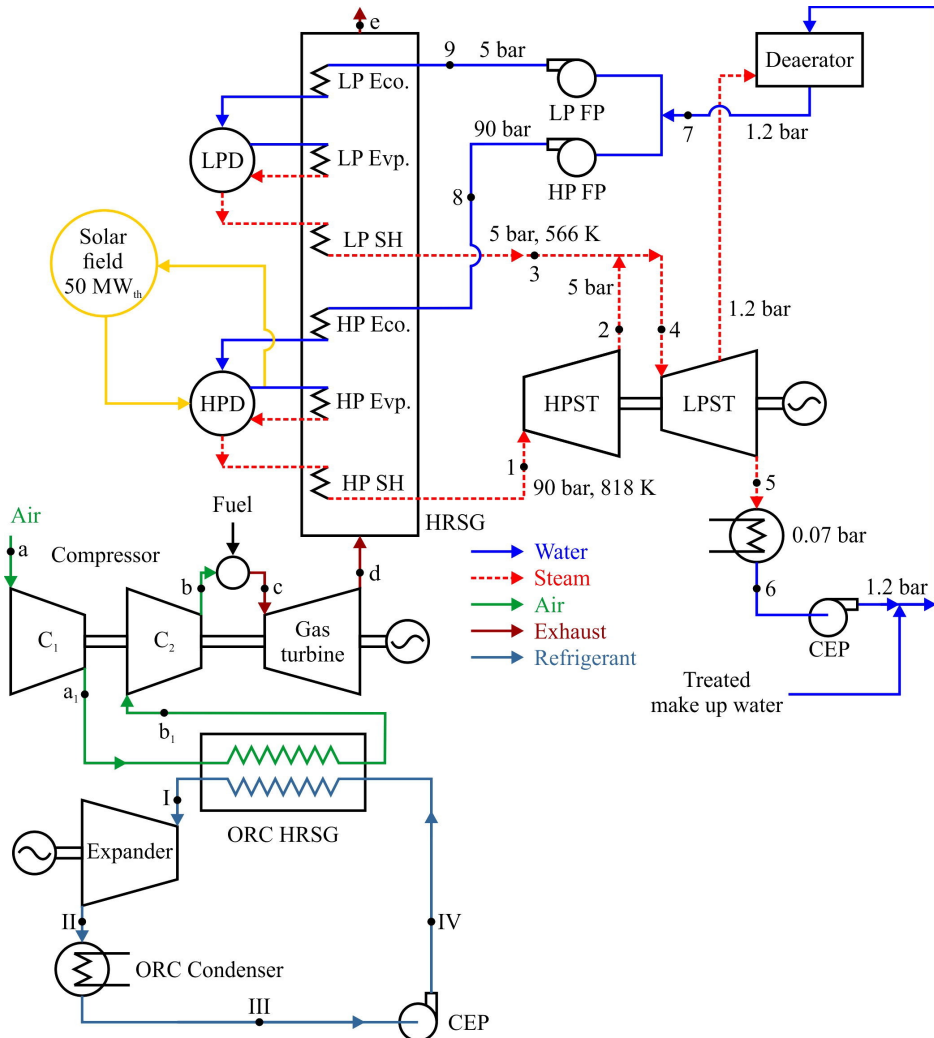


Figure 1-6 Schematic of the proposed ISCC with two bottoming cycles

tower combined heat and power plant with a topping air Brayton cycle. The conventional gas turbine combustion chamber is replaced with a solar receiver. A simple downstream Rankine cycle with a heat recovery steam generator and a process heater have been considered for integration with the solar Brayton cycle.

Li et al.<sup>[87]</sup> presented a novel cascade system using both steam Rankine cycle and organic Rankine cycle. Screw expander is employed in the steam Rankine cycle for its good applicability in power conversion with steam-liquid mixture. The heat released by steam condensation is used to drive the organic Rankine cycle.

Al-Sulaiman<sup>[88]</sup> compared the produced power of an SRC-ORC combined cycle with

traditional SRC cycle. The SRC is driven by parabolic trough solar collectors, and the ORC cycle is driven by the condensation heat of the SRC.

Dunham and Lipi<sup>[89]</sup> proposed a single Brayton and a combined Brayton-Rankine power cycle for distributed solar power generation and compared its theoretical efficiency to a single Brayton cycle. Different working fluids were examined as working fluids in the bottoming Rankine cycle. It is found that the combination of the Brayton topping cycle using carbon dioxide and the Rankine bottoming cycle using R-245fa gives the highest combined cycle efficiency of 21.06%, while a single Brayton cycle is found to reach a peak cycle efficiency of 15.31% with carbon dioxide at the same design point conditions.

Bahrami et al.<sup>[90]</sup> proposed a combined ORC power cycle. An ORC was used as the cold-side heat rejector of a Stirling engine. The operating temperatures of the ORC are between 80°C and 140°C and the combined system can achieve 4% to 8% higher efficiency compared with a standard Stirling cycle.

Thierry et al.<sup>[91]</sup> proposed a nonlinear optimization formulation of multistage Rankine cycle with two types of configurations. Both cascade style and series style of the ORC are considered. The results show that for some cases the multistage configurations can achieve higher efficiency at low temperature.

Bahari et al.<sup>[92]</sup> considered the optimization of an integrated system using organic Rankine cycle to utilize the heat released by the Stirling cycle. However, the integrated system is a primitive design and it takes no consideration of the application in CSP.

### 1.3 Literature summary

Reviewing the former literatures concerning solar thermal power it can be found that most of the research works have focused on specific solar thermal power technologies to increase efficiency or reduce costs.

A small number of researchers have also studied the cascade collection or cascade utilization of solar energy.

There is no literature on the combination of cascade collection and cascade utilization in one cascade solar thermal power system. No systematically analysis of the cascade system has been found.

## 1.4 Research content

This research is based on the international cooperation project "Collaborative research on key technologies to produce electricity by cascade utilization solar thermal energy" as the background. The objective of this project is to research the equipment of solar thermal power generation system, to propose, develop and optimize a solar thermal cascade system depending on the advantages and disadvantages of the solar thermal power generation systems, and to explore a new feasible technology for large-scale solar thermal power generation. The main research contents of this thesis are as follows:

- (1) Selecting reasonable topologies for cascade solar thermal power generation systems. According to the thermodynamic characteristics and operating behaviors of components in thermal power generation systems, reasonable topologies are selected. These topologies should be able to embody the benefits of cascade systems and help to improve the performance of solar thermal power system.
- (2) Establishing the mechanical model of each component in solar thermal power generation system. Based on the governing equations and operating characteristics of each component, a mechanism model will be established. Object-oriented features will be applied to create component models easy to combine, extend, and replace.
- (3) System modeling for each proposed cascade system scheme. Based on the mechanism models of the components, a software that provides the functions of system topology arrangement, component connection, parameter setting and environment selection will be developed for the system investigation.
- (4) Optimizing the subsystem of the cascade system. Specifically, a staged heating method will be analyzed for the optimization of the steam generating system. Different layouts of Stirling engines will be analyzed to find out best layouts of the Stirling engines in the cascade system.
- (5) Finding out the conditions conductive for cascade solar thermal power application. Selecting appropriate stand-alone systems for comparative analysis of the cascade systems. Analysis of the influences of various parameters on the efficiency difference between cascade system and its corresponding stand-alone systems will be conducted.
- (6) Building a solar thermal power generation test platform to carry out experimental works for solar thermal power generation. Special experiment cases considering the

features of solar irradiance need to be designed to investigate the impact of different factors on the system performance. Influences of different factors on the performance of components will be investigated. Thermal performances of trough collectors and dish collectors will be analyzed, and the simulation models will be validated.

## Chapter 2 System topology

### 2.1 System topology design

The objective of this research is to investigate the equipment of solar thermal power generation system, to propose, develop and optimize a cascade solar thermal system depending on the advantages and disadvantages of existing solar thermal power generation technologies.

Three solar thermal power generation technologies are commercially proven – parabolic trough, parabolic dish and solar tower. Considering the future deployment of solar cascade demo system, two solar thermal technologies, parabolic trough and parabolic dish, are chosen as the basic systems for the design of cascade solar thermal power system. For the cascade utilization of the high temperature heat obtained from the parabolic dish receiver, air (or nitrogen) is used as the HTF to transfer the heat collected. Figure 2-1 shows the schematic diagrams of a parabolic trough system and a parabolic dish system. To make the system structure diagrams in this thesis more clearly and consistent, legends of the components that may appear in solar power systems are listed in Figure 2-2.

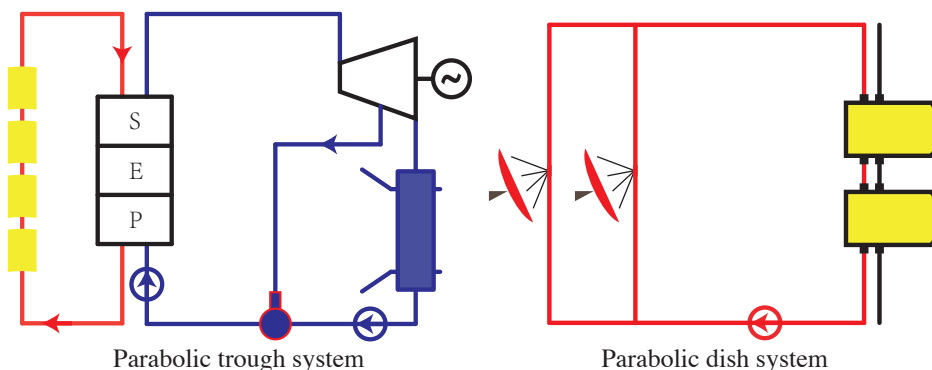


Figure 2-1 Schematic diagrams of a parabolic trough system and a parabolic dish system

With different considerations (such as water Rankine cycle or ORC, combination of different systems, connection types of collectors, etc) of the cascade system topology, multiple combination topologies may be used for cascade systems. To get the most suitable system topology, these considerations will be analyzed in the following sections.

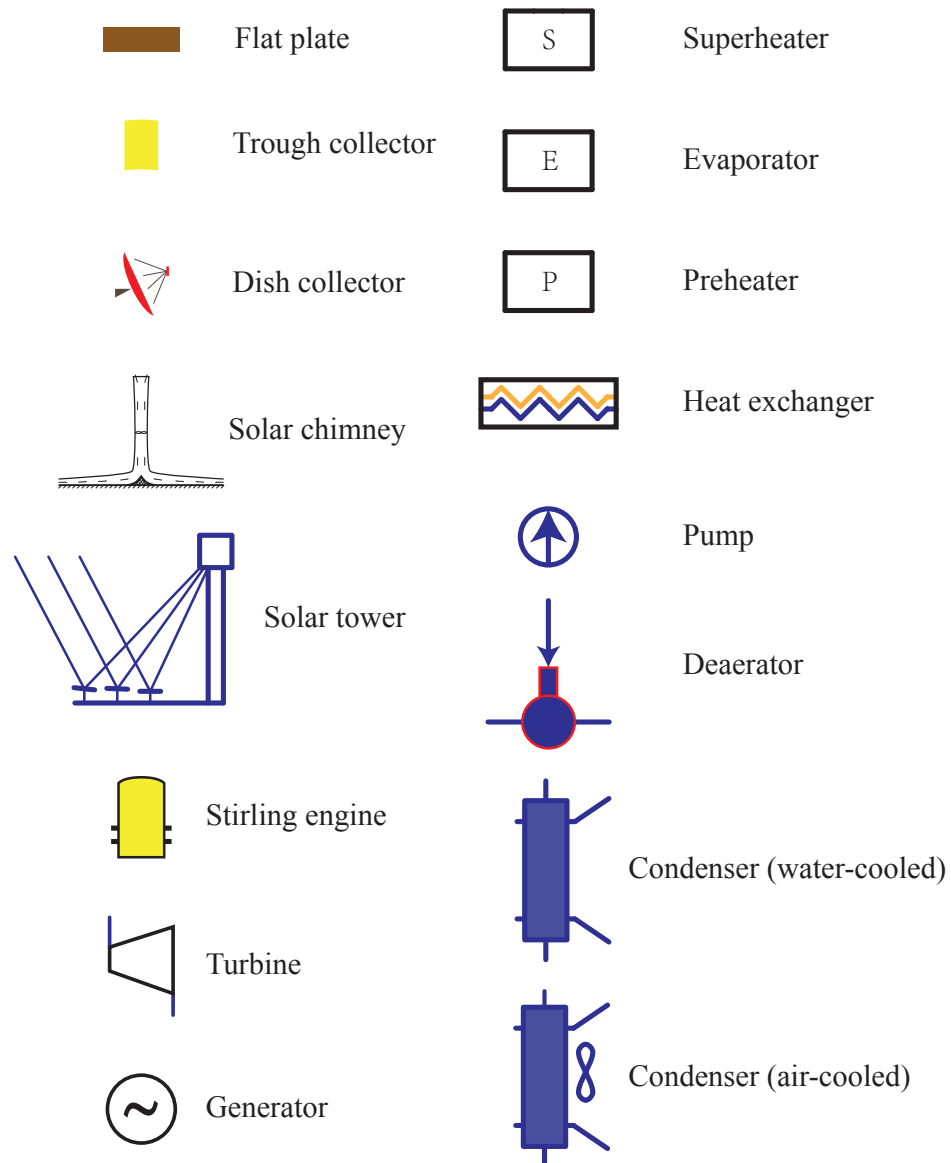


Figure 2-2 Components in solar power systems

### 2.1.1 Rankine cycle fluid

An ideal working fluid for Rankine cycle would have the temperature-entropy diagram given in Figure 2-3. The following characteristics listed by Abbin and Leuenberger<sup>[93]</sup> describe this fluid:

- The heat capacity of the liquid phase should be small. This makes the curve 22' in Figure 2-3 almost vertical.

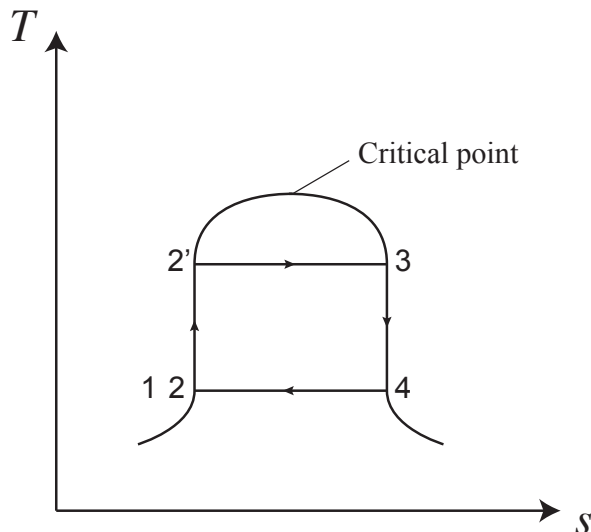


Figure 2-3 Temperature-entropy diagram of an ideal working fluid

- The critical point should be above the highest operating temperature to allow all heat to be added at that temperature.
- The vapor pressure at the highest operating temperature should be moderate for safety reasons and to reduce the cost of the equipment.
- The vapor pressure at the condensing temperature should be above atmospheric pressure to prevent air leakage into the system.
- The specific volume of the vapor at state 4 should be small to avoid large-diameter turbine wheels, casings, and heat exchangers.
- The saturated vapor curve 3-4 in Figure 2-3 should be vertical to avoid expansion into the wet vapor region ( $ds/dT < 0$ ) or expansion into the superheat region ( $ds/dT > 0$ ).
- For low-power turbine applications, the fluid should have a high molecular weight to minimize the rotational speed and/or the number of turbine stages and to allow for reasonable mass flow rates and turbine nozzle areas.
- The fluid should be liquid at atmospheric pressure and temperature for ease of handling and containment.
- The freezing point should be lower than the lowest ambient operating temperature.
- The fluid should have good heat-transfer properties, be inexpensive, thermally stable at the highest operating temperature, nonflammable, noncorrosive, nontoxic, and so

on.

Water is the most commonly used fluid for Rankine cycle, it is more mature to design Rankine cycle components for steam systems than any other liquid. It is inexpensive to use (although boiler-grade water must be highly distilled and thus costs more than tap water), sealing of the high-pressure portions of a Rankine cycle using steam is not critical. Non-flammability and ready availability of steam are additional advantages. Because it has a critical temperature and pressure of 374°C and 22.1 MPa, it can be used for systems operating at fairly high temperatures with most of the heat addition (at constant temperature) and at moderate pressure. Figure 2-4a shows the schematic diagram of a typical steam Rankine cycle solar system.

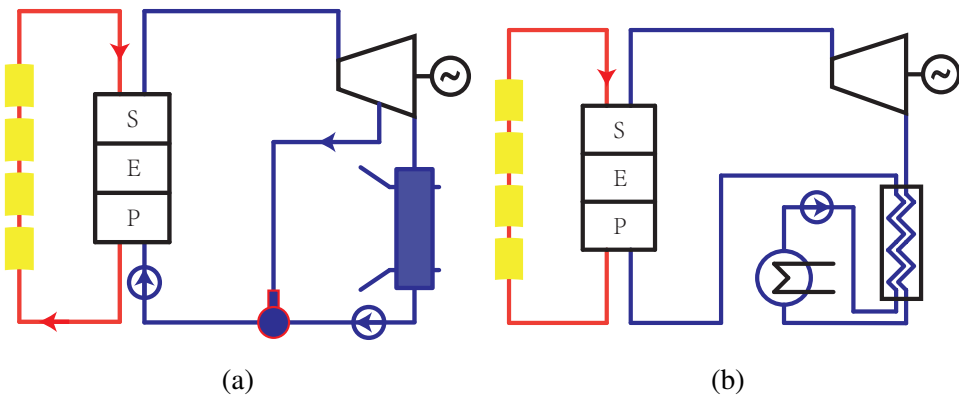


Figure 2-4 Schematic diagrams of two types of Rankine cycle solar system

There are some disadvantages for steam as the Rankine cycle fluid. The low temperature characteristics of steam are not ideal because the steam has a low vapor pressure and a very low density at ambient temperature (see Table 2.1). Therefore, sealing air from low pressure components is a major design problem.

The organic Rankine cycle can be used in the solar parabolic trough technology in place of the usual steam Rankine cycle. The ORC allows power generation at lower capacities and with a lower collector temperature, and hence the possibility for low-cost, small scale decentralized CSP units. Most organic fluids used in organic Rankine cycle are drying fluids. The vapor leaving the expander still contains heat that can be transferred to the compressed liquid stream because the turbine outlet temperature is above the condenser temperature. A

Table 2.1 Saturated steam pressure at the corresponding temperature

| $T(K)$         | 373.15 | 363.15 | 353.15 | 343.15 | 333.15 | 323.15 | 313.15 | 303.15 | 293.15 |
|----------------|--------|--------|--------|--------|--------|--------|--------|--------|--------|
| $p(Pa)$        | 101322 | 70117  | 47373  | 31176  | 19932  | 12344  | 7381   | 4246   | 2339   |
| $\rho(kg/m^3)$ | 0.5982 | 0.4239 | 0.2937 | 0.1984 | 0.1304 | 0.0831 | 0.0512 | 0.0304 | 0.0173 |

vapor-to-liquid heat exchanger, known as a regenerator, is typically used for this purpose. Figure 2-4b shows the schematic diagram of a typical organic Rankine cycle solar system.

Compared with steam for the Rankine cycle, it has the following advantages:

- Small turbine head allows for moderate shaft speed and a single- or two-stage design.
- Low volume ratio facilitates the flow path design.
- High volume flow and low velocity of sound results in reasonable flow areas.
- Low temperature drop during expansion reduces thermal stress problems.
- Dry expansion avoids blade erosion caused by vapor wetness.
- Low system pressure facilitates housing design.

### 2.1.2 Solar chimney

Solar chimney, also known as solar updraft tower, directly (without concentration) uses the sun's heat to generate power. It uses solar radiation to increase the internal air temperature to form a flow to the chimney located at the middle of the roof. Figure 2-5 shows the schematic diagram of a typical solar chimney power plant. In this plant, air is heated by the green house effect under the translucent roof. As the roof is open at its periphery, air flows into the plant due to different density distribution. Hot air flows into the chimney because of buoyancy. An electricity-generating turbine is set in the path of the air current to convert the kinetic energy of the air flow into electricity.

The solar chimney can use the low temperature (low grade energy) for power generation. So the combination of parabolic trough system and solar chimney is considered an effective way for energy cascade utilization. In the combined system, the condenser in the Rankine cycle is air cooled. The fan blows the hot air that has cooled the condenser into the solar chimney power plant from its periphery. The hot air stream converges at the bottom of

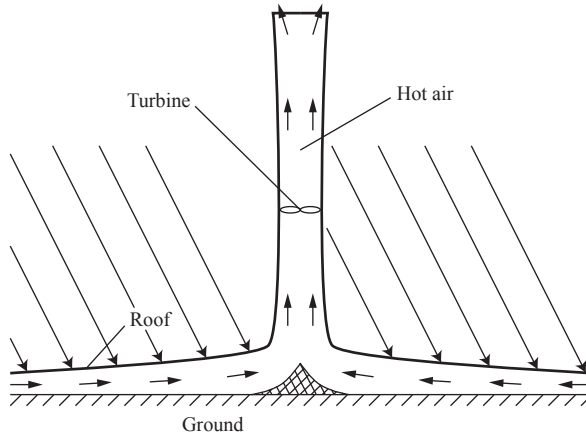


Figure 2-5 Schematic diagram of a solar chimney power plant

chimney, flows upward with the action of buoyancy and drives the turbine in the chimney. Energy of the hot air can be utilized by the solar chimney. Figure 2-6 shows an example of the combined system.

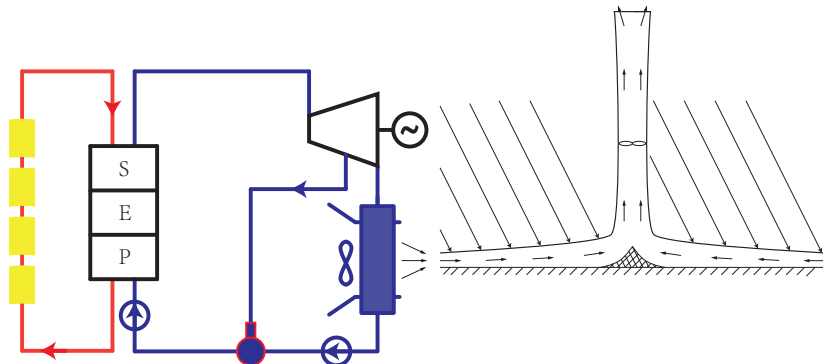


Figure 2-6 Schematic diagram of a combined solar trough and chimney power system

### 2.1.3 Collector series connection

Considering different heat collecting temperatures of different types of collectors, series connection of different types of collectors can be a feasible choice for solar cascade collection. Trough collectors and Fresnel collectors have better performance and lower cost for lower temperature heat collection. Dish collectors and solar towers are more suitable for higher temperature heat collection. Serial connection utilize the advantages of different types of collectors. Figure 2-7 shows an example of a cascade system using collector series

connection. In this system, air, the HTF, is preheated by parabolic collectors before it flows into the parabolic dish collectors.

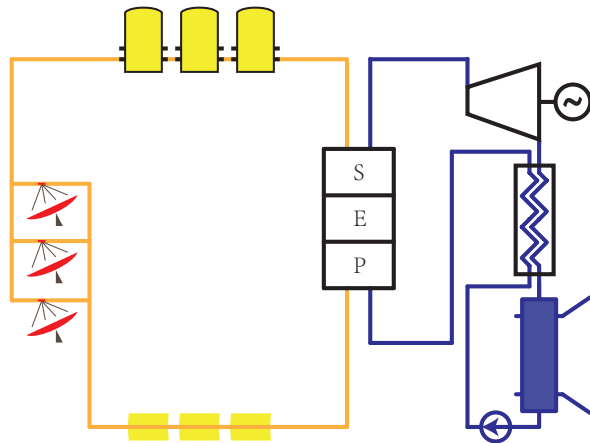


Figure 2-7 Schematic diagram of a cascade system using collector series connection

#### 2.1.4 Direct steam generation

Direct steam generation (DSG) in parabolic troughs is considered as an attractive option for both economic and efficiency improvement of for solar thermal electricity generation applications.<sup>[94,95]</sup> It allows higher cycle temperatures and, consequently, higher Rankine cycle efficiencies.<sup>[96]</sup> In conventional parabolic trough solar plants, HTF (typically synthetic oil or melton salt) is used in the solar field. It leads to high pressure drop, limits the HTF related equipment operation, maintenance and cost. Besides, the highest temperature of the Rankine cycle is limited by HTF temperature, and large temperature difference exists between the HTF and working fluid of the Rankine cycle. So generating steam in the receiver tubes (direct steam generation, DSG) of the solar collector is one of the directions to reduce the cost and increase the efficiency of the parabolic trough systems. Figure 2-8 shows the schematic diagram of a typical DSG solar system.

#### 2.1.5 Heat exchanger between circuits

Heat transfer between different circuits can be applied for cascade utilization of the heat collected. Depending on the two basic solar system as shown in Figure 2-1, there are two types of heat exchangers that can be applied in the cascade solar system.

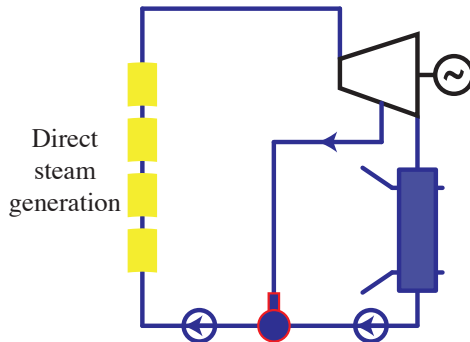


Figure 2-8 Schematic diagram of a typical solar trough using DSG

For the first type, air-oil heat exchanger is applied to transfer heat between the air circuit and the oil circuit. Figure 2-9 shows an example of solar system using this type of heat exchanger. In this system, after providing heat for the Stirling engines, the hot air flows through the air-oil heat exchanger and provides heat for the oil.

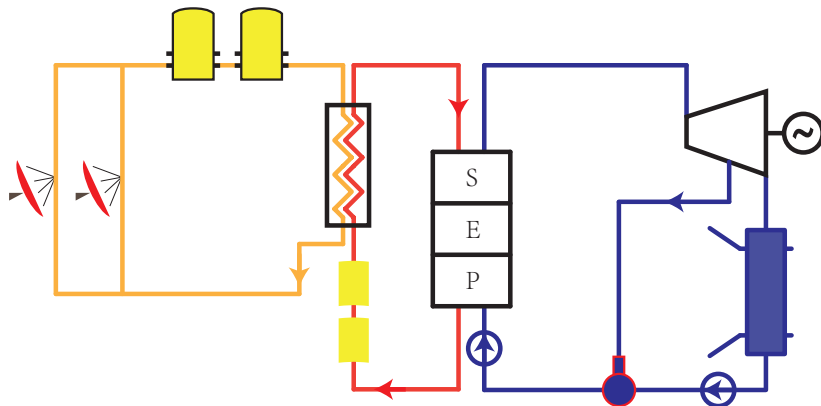


Figure 2-9 Schematic diagram of a solar system using air-oil heat exchanger

In the second type, air-water heat exchanger is applied to transfer heat between the air circuit and the water circuit. Figure 2-10a and Figure 2-10b show two different kinds of cascade solar systems using this type of heat exchanger. In Figure 2-10a, after providing heat for the Stirling engines, hot air flows through the air-water heat exchanger and provides heat for superheating. In Figure 2-10b, after providing heat for the Stirling engines, the hot air flows through the air-water heat exchanger and provides heat for preheating.

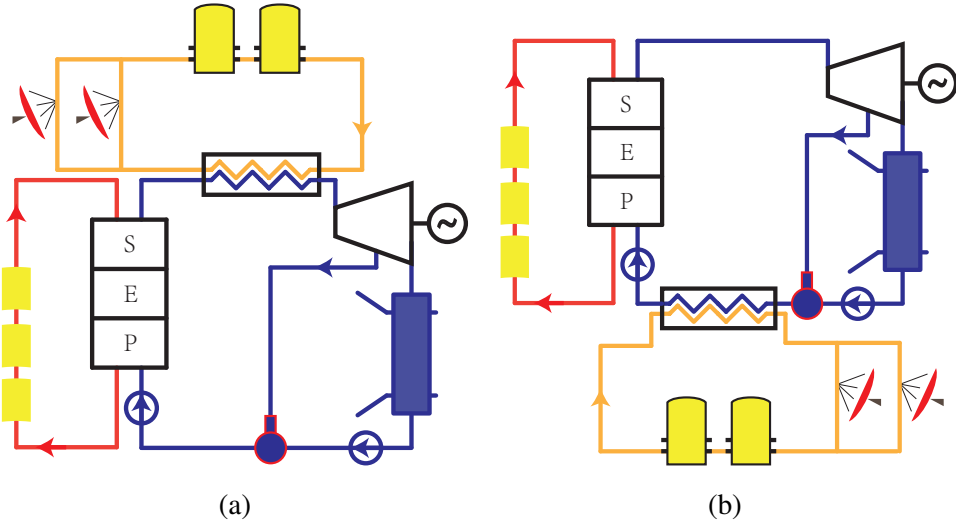


Figure 2-10 Schematic diagrams of two kinds of solar systems using air-water heat exchanger

### 2.1.6 Heat recovery between cycles

According to the second law of thermodynamics, it is impossible for any device that operates on a cycle to receive heat from a single reservoir and produces a net amount of work. For a heat engine, it requires both a hot source and a cold sink to convert heat energy to mechanical energy. Figure 2-11 shows the  $T - s$  diagram of a typical heat engine. In a thermodynamic cycle, heat is absorbed from the hot source, only part of it can be converted into mechanical work by the engine. The conversion ratio related to the temperatures of hot source and cold sink is fundamentally limited by Carnot's theorem.

Only those engines suitable for external heating are usually considered for solar applications. Unlike an internal combustion engine that generates heat within the working fluid, an externally heated engine needs external heat to be added to the working fluid by a heat exchanger.

Three types of engines are designed to accept external heat and have been used for solar heat sources: the Rankine, the Stirling, and the Brayton cycles<sup>[97]</sup>. The Rankine and Brayton cycles are both suitable for constant-pressure heat-addition. The original Brayton engine uses piston compressors and piston expanders, but more modern gas turbines and airbreathing jet engines also follow the Brayton cycle. Although the cycle is usually an open system, in order to carry out thermodynamic analysis, usually it is assumed that exhaust gases are reused as the intake so that the whole process can be analyzed as a closed cycle. The Stirling machine uses

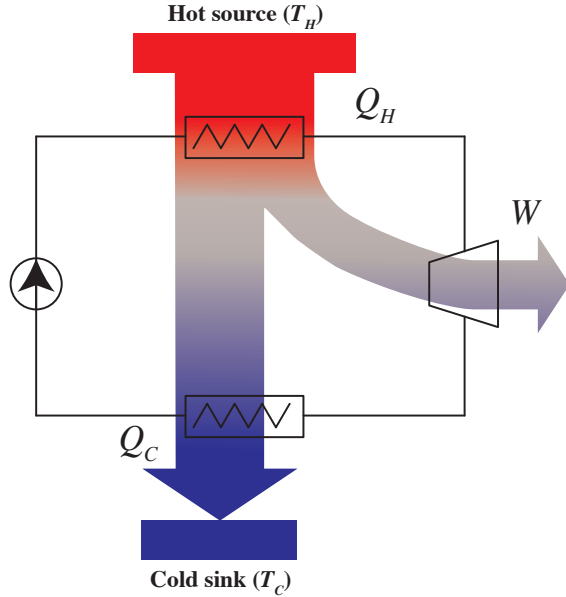


Figure 2-11 Diagram of a typical heat engine

a reciprocating piston design that allows external heating to be combined into its constant-temperature heat-addition process. In a Rankine cycle, the pressurized liquid enters a heat exchanger where it is heated at constant pressure by an external heat source to become vapor.

These three kinds of cycles work at different optimum operating temperatures. Rankine cycle works with the lowest hot source temperature and Brayton works with the highest. Figure 2-12 shows the diagram of the three cycles used in solar energy. The heat released by these cycles may be recovered by another cycle (as a bottom cycle).

## 2.2 System topology selection

### 2.2.1 Rankine cycle fluid

There are two important aspects to consider when selecting the working fluid of the Rankine cycle solar power system:

1. Select the working fluid that is conducive to the optimization of the cycle efficiency. For a Rankine cycle solar system, the collector efficiency reduces with operating temperature, and the Rankine cycle efficiency increases with operating temperature, there exists an optimal operating temperature as illustrated in Figure 2-13. The working

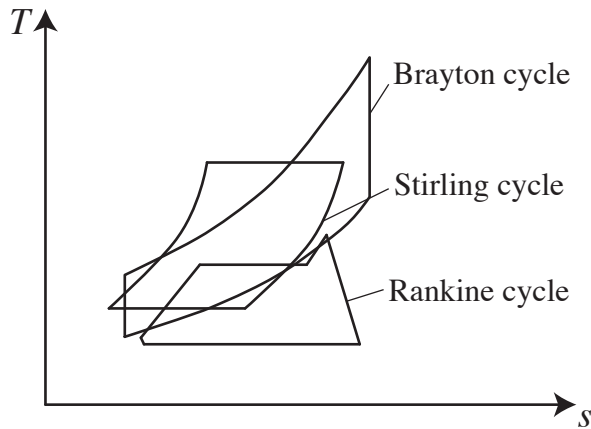


Figure 2-12 Diagram of three cycles used in solar energy

fluid should be conducive to achieve the optimal operating temperature.

2. The working fluid state matches the heat transfer fluid state, if heat transfer fluid is used. On the one hand, the operating temperature of the working fluid should be lower than the collecting temperature of the HTF. On the other hand, the operating temperature of the working fluid should not be much lower than the collecting temperature of the HTF to avoid large exergy loss during the heat exchange process.

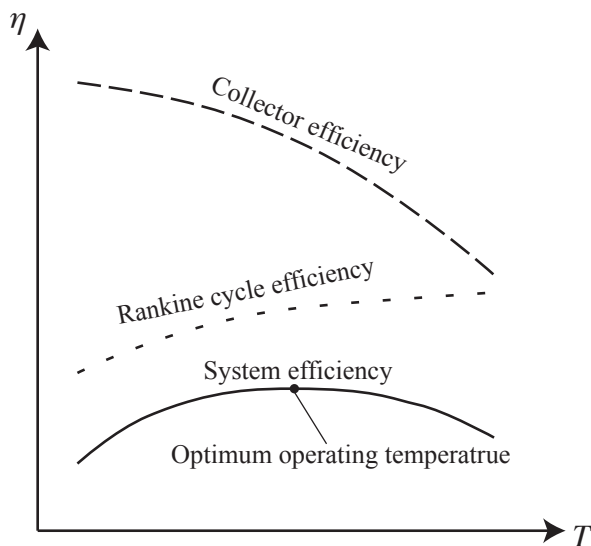


Figure 2-13 Efficiency variation with operating temperature

Based on the advantages and disadvantages of water and organic fluid as the working

fluid of Rankine cycle, it is clear that, for low operating temperature and small capacity distribution power generation, organic fluid will be a better choice, otherwise water is the better one. Bao and Zhao<sup>[98]</sup> presented a comprehensive review of working fluid selection (including pure fluids and mixtures). In this review, many factors such as operating conditions, working fluid characteristics, equipment structures and environmental safety considerations were considered. It has to be mentioned that the types of working fluids (mainly dry or wet) will affect the operation and layout of the system.

### 2.2.2 Solar chimney

Section 2.1.2 shows the idea of coupling solar chimney to concentrated solar thermal power generation technologies. However, the efficiency of current solar chimney system is very low. Primary design data of solar chimney power plants with different location, different chimney height and collector height are shown in Table 2.2<sup>[99]</sup>. The preliminary design parameters are selected and determined for a nominal solar irradiation intensity of  $1000 \text{ W/m}^2$  and the nominal plant power of 5 MW. From the table, it can be found that the chimney efficiency and total efficiency are very low and the technology is still in the developing stage.

Besides, a solar chimney is costly and requires vast land, which is adverse to the future deployment of solar cascade demo system. With these considerations, the solar chimney plans are not adopted for the cascade system.

### 2.2.3 Collector series connection

Each type of collector has its own suitable temperature range. It is feasible to heat the HTF step by step using different types of collectors with series connection.

A collector series connection is proposed in Section 2.1.3 (see Figure 2-7) depending on the basic systems. In this configuration, air is heated in the trough collectors and dish receivers consequently. After providing heat for the Stirling engines, the hot air flows into the heat exchanger to provide heat for the Rankine cycle. In this topology, air is used as the HTF for the solar trough, this idea is only numerically and experimentally studied,<sup>[27,100]</sup> no commercial applications can be found up to now. This technology is mainly constrained by the low conductivity and low heat capacity of air, which leads to low system efficiency. For this consideration, this topology is not adopted due to the air parabolic trough technology.

Table 2.2 Results of SEA models under specified parameters

|   | Ottawa | Winnipeg | Edmonton | Schlach |
|---|--------|----------|----------|---------|
| Collector diameter (m)                        | 1110   | 1110     | 1110     | 1110    |
| Collector area ( $m^2$ )                      | 950000 | 950000   | 950000   | 950000  |
| Chimney height (m)                            | 123    | 60       | 35       | 547     |
| Collector height (m)                          | 848    | 975      | 1024     | -       |
| Chimney diameter (m)                          | 54     | 54       | 54       | 54      |
| Temperature rise in collector ( $^{\circ}C$ ) | 25.9   | 25.9     | 25.9     | 25.9    |
| Updraft velocity (m/s)                        | 9.1    | 9.1      | 9.1      | 9.1     |
| Total pressure head (Pa)                      | 518.3  | 518.3    | 518.3    | 383.3   |
| Average efficiency                            |        |          |          |         |
| Collector (%)                                 | 56.00  | 56.00    | 56.00    | 56.24   |
| Chimney (%)                                   | 1.82   | 1.82     | 1.82     | 1.45    |
| Turbine (%)                                   | 77.0   | 77.0     | 77.0     | 77.0    |
| Whole system (%)                              | 0.79   | 0.79     | 0.79     | 0.63    |

It can be a good choice to apply flat plate solar collectors and parabolic trough collectors in traditional solar power tower plant that uses water as the HTF (such as Solar One). As demonstrated in Figure 2-14, condensed water is heated by the flat plate solar collectors and feedwater is heated by the parabolic trough collectors. Flat plate collectors and parabolic trough collectors have much lower unit thermal cost compared to solar power tower. The addition of flat plate collectors and parabolic trough collectors can effectively reduce the cost of the system. Although this scheme is promising and deserves further research, the cascade system in this thesis will not consider it for the requirement of solar power tower is adverse to the deployment of cascade demo system.

#### 2.2.4 Direct steam generation

Direct steam generation for solar thermal power generation has the advantages of having fewer components and no temperature drop due to an intermediate transfer. Besides, it is clear

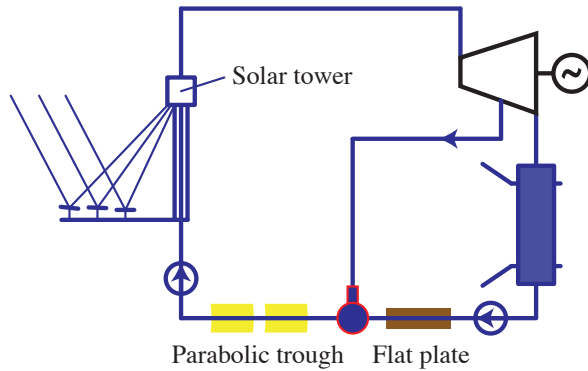


Figure 2-14 Schematic diagram of a solar power tower using collector series connection

that water is characterized by lower environmental risk than thermal oil so that leakages in a DSG power plant do not represent an environmental hazard<sup>[101]</sup>. Water has a lower freezing temperature than thermal oil and solar salt: the efforts required to ensure adequate anti-freezing protection are significantly reduced. Water is also less corrosive than solar salt<sup>[102]</sup>.

However, all the CSP commercial plants already built apply indirect steam generation, with the exception of the 5 MWe DSG Thai Solar One (TSE-1) plant in Thailand (Thailand, 2012)<sup>[103]</sup>. The reason for this universally accepted choice must be found in the difficulties related to the flow control and manufacturing of equipment to be used in the presence of a two-phase flow in the absorber tubes. The behavior of the two-phase flow inside the absorber tubes of a parabolic-trough collector forces the implementation of a complex and expensive control system and the use of fast water streams in order to avoid stratified flow.

Besides, the receiver should be designed with care to ensure that the flux in the regions of vapor is less than the regions where boiling is taking place. This is because the liquid's heat transfer coefficient is significantly higher than superheated steam. For similar solar flux values, burnout of the receiver may occur in the region where vapor exists on the other side of the receiver wall. Many concentrating collector designs require the receiver to change its attitude while tracking the sun. This change of attitude increases the possibility of high flux in the steam-containing receiver section.

Another problem related to DSG is the high value of the steam pressure inside the receiver tubes that must match the turbine inlet pressure. Indeed, handling of movable and flexible parts forming the collector's receiver tube at high pressure values is one of the major problems that the DSG technology faces at its early stages.

Applying direct steam generation may be a better choice in the cascade system in the

future, however, it is not adopted for the cascade system for its immaturity.

### 2.2.5 Heat exchanger between circuits

Section 2.1.5 introduces two types of heat exchangers that may be applied in the solar thermal cascade system – the air-oil heat exchanger (see in Figure 2-15) and the air-water heat exchanger (see in Figure 2-16).

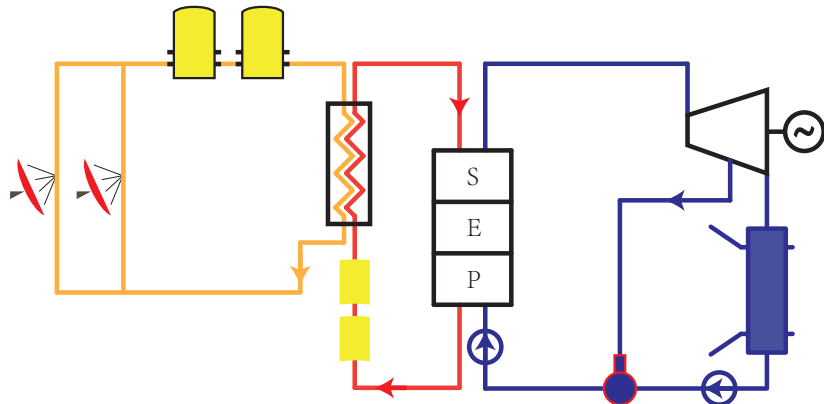


Figure 2-15 Schematic diagram of a solar system using air-oil heat exchanger

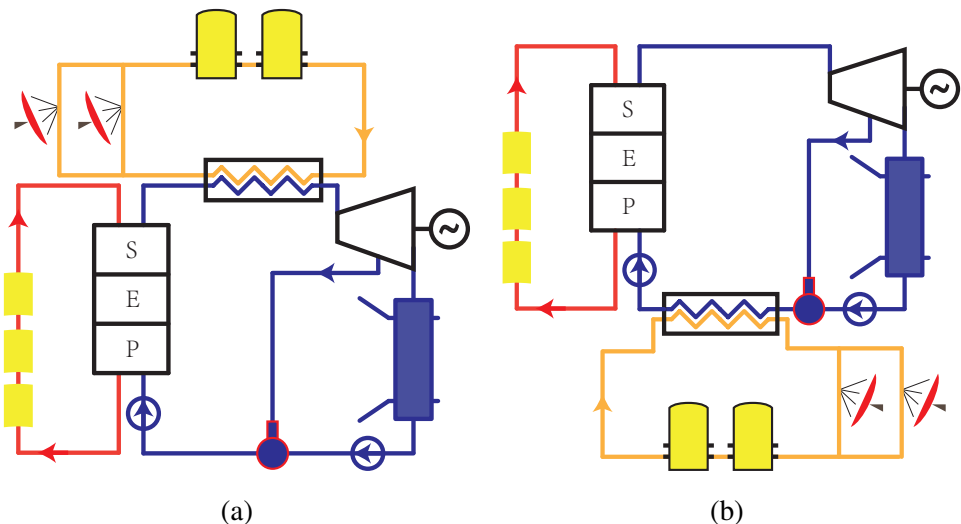


Figure 2-16 Schematic diagrams of two kinds of solar systems using air-water heat exchanger

For the first type, air provides heat for oil. It is not economic for several reasons. First,

The temperature of the heat transfer oil can not be further increased. The temperature of the oil is not limited by the parabolic trough collectors. The temperature of the oil is constrained by the oil properties and heat collecting temperature of the trough collectors can exceed this value. In high temperature conditions, oil may deteriorate, evaporation, decompose, which has a negative impact on the stable and safe operation of the system. Second, using dish to provide heat for the oil is not suitable since the dish is designed for higher temperature collections and it's less cost-effective compared with parabolic trough.

For the second type, air provides heat for water. Two kinds of solar systems using air-water heat exchanger can be found in Figure 2-16. Figure 2-16a shows the scheme that air after the Stirling engine is used to overheat the steam. It's feasible since the air can increase the average temperature of the endothermic process of the water to increase the efficiency of Rankine cycle. On the other hand, in a conventional solar trough system, the main steam temperature is limited by the oil, which is not conductive to Rankine cycle efficiency. In this proposed cascade system, the main steam temperature of the Rankine cycle can be raised to be higher than 400°C to eliminate the negative effect of the oil. This is the scheme that will be discussed in detail in the next few chapters. Figure 2-16b shows the scheme that air after the Stirling engine is used to preheat the feed water. It is not a good choice since the temperature difference of the heat transfer process is large and it provides no benefits to increase the inlet temperature of the steam turbine.

### 2.2.6 Heat recovery between cycles

As it is mentioned in Section 2.1.6, different thermodynamic cycles work at different optimum working temperatures. Since each thermodynamic cycle has endothermic and exothermic processes, a bottoming cycle may use the released heat of a topping cycle.

In our basic systems (see Figure 2-1), Rankine cycle and Stirling cycle can be coupled for cascade usage. Figure 2-17 shows two configurations of the cascade systems with heat recovery between cycles. For a traditional Stirling engine, to enhance the performance, cooling water is used to absorb the heat released by the engine. The absorbed heat is wasted without reuse. In Figure 2-17a, condensate of the Rankine cycle is used to cool the Stirling engine. Rejected heat of the Stirling cycle can be recycled by Rankine cycle. For organic Rankine cycles, different working fluids determine the working temperature zones. It is feasible to

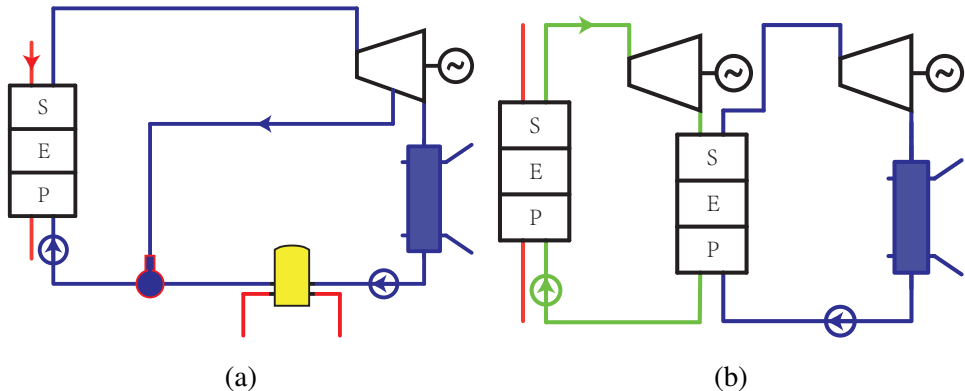


Figure 2-17 Two configurations with heat recovery between thermodynamic cycles

reuse the condensation heat of an organic Rankine cycle by another organic Rankine cycle. In Figure 2-17b, two organic Rankine are coupled together for power generation. The bottoming cycle uses the condensation heat of the topping cycle for preheating, evaporation and superheating.

### 2.3 Selected system topology

Considered all the conditions in Section 2.1 and Section 2.2, two system topologies are chosen for this research as shown in Figure 2-18.

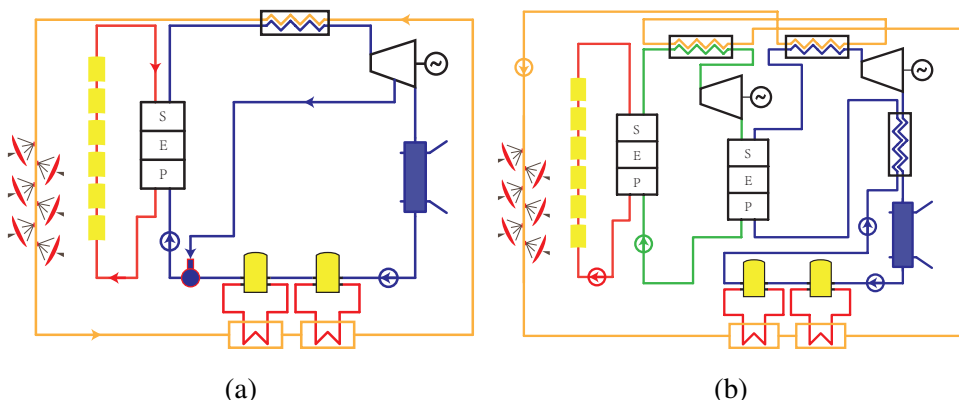


Figure 2-18 Two selected typical cascade systems

In Figure 2-18a, the cascade system has the following features:

- *Multiple types of collectors.* Trough collectors are applied for lower temperature heat collection and dish collectors are applied for higher temperature heat collection. This helps to reduce the cost and improve the efficiency.
- *Multiple types of thermodynamic cycles.* Rankine cycle is applied for lower temperature heat utilization. Stirling cycle is applied for higher temperature heat utilization.
- *Air-water heat exchanger.* An extra air-water heat exchanger is applied to increase the temperature of the main steam, which helps to improve the efficiency of Rankine cycle. On the other hand, it can overcome the disadvantage of low limit temperature of heat transfer oil in conventional solar trough systems, which helps to achieve higher main steam parameters than traditional solar trough systems.
- *Condensate for Stirling engine cooling.* Condensate of the Rankine cycle is used to cool the Stirling engine. Rejected heat of the Stirling cycle can be reused by Rankine cycle, which helps to improve the overall system efficiency.

In Figure 2-18b, the cascade system also has the features mentioned above. Besides, it uses different kinds of organic fluid as the working fluid, which adapts more general working temperature for solar energy systems. Figure 2-19 shows a calculation example of the cascade system.

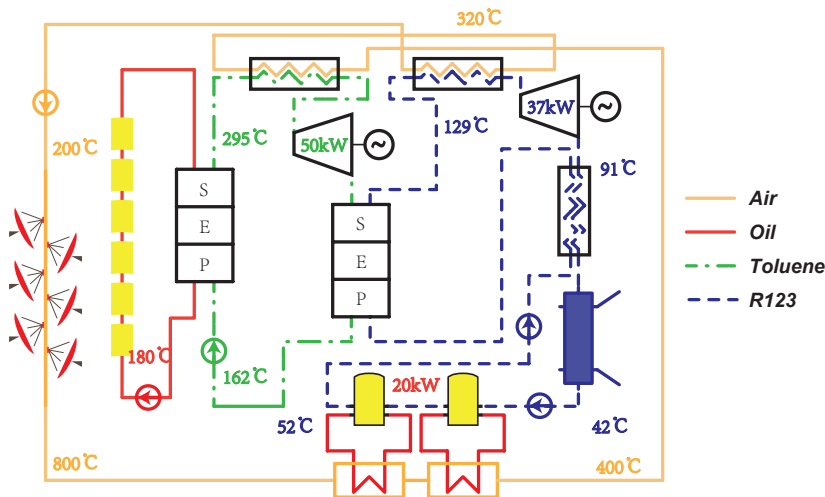


Figure 2-19 A calculation example of cascade system shown in Figure 2-18b

Both cascade systems will be modeled for investigation. However, considering the more extensive application of steam Rankine cycle, the system described in Figure 2-18a will be

used as the main research content in the following chapters.

## 2.4 Conclusion

This chapter systematically introduces a number of considerations in cascade solar thermal system design. These considerations include Rankine cycle fluid type, solar chimney, collector series connection, direct steam generation, heat exchanger between circuits and heat recovery between cycles.

These considerations are carefully checked for the cascade system study. Combining with the research direction, two typical system topologies suitable for the deployment of cascade demo system are put forward. These two typical system topologies have the following features:

- Multiple types of collectors are applied.
- Multiple kinds of thermodynamic cycles are applied.
- Air-water heat exchanger is applied to increase the Rankine cycle efficiency.
- Condensate for Stirling engine cooling to recover the heat rejected by the engine.

It is worthy noting that some of the considerations of the system topology design deserves more concern in the future. For example, a solar power tower combined with parabolic trough collectors and flat plates as shown in Figure 2-14 effectively utilizes the characteristics of the collectors. Besides, when the technology of direct steam generation is mature, it is worthy to apply it in cascade system for its less equipment required and no temperature loss feature.

## Chapter 3 Modeling

To investigate the performance of the proposed cascade systems, mechanism models of the systems are developed with EES (Engineering Equation Solver) and MATLAB (Matrix Laboratory). Bottom-up design method is used for the system modeling. Firstly, the mechanism models developed in EES are used to validate the theoretical relationships of the models. Secondly, the component models are developed in MATLAB using object-oriented method. It makes full use of inheritance and polymorphism to ensure both the independence and the relevance of the components. Three circuits, air circuit, water circuit and oil circuit, are developed with some specific state parameters in some key components. Energy-based models of these key components are created on the basis of their thermodynamic behavior, heat transfer and the second law.

The following part introduce models of some key components.

### 3.1 Component modeling

#### 3.1.1 Parabolic trough collector

Parabolic trough collector consists of a reflector and a receiver. The reflector (mirror) reflects direct normal radiation and concentrates it onto a receiver tube located at the focal line of the parabola. The receiver is typically a metal absorber tube with high absorption rate coating. An outer glass tube is used outside the absorber tube to reduce thermal losses and the space between the absorber tube and the glass tube is usually drawn into a vacuum to further reduce thermal losses.

Optical loss exists in the reflection process due to optical efficiency terms. The reflection terms can be listed as bellow<sup>[4]</sup>:

- Shadowing factor
- Tracking error
- Geometry error
- Clean mirror reflectance
- Dirt on mirrors

- Unaccounted errors

Another term, incident angle modifier  $K(\theta)$ , should be concerned when the solar irradiation is not normal to the collector aperture. It is a function of the solar incidence angle to the normal of the collector aperture ( $\theta$ ).

$K(\theta)$  is expressed by the following equation concluded from trough collector testing conducted at SNL.<sup>[5]</sup>

$$K(\theta) = \cos \theta + 0.000884\theta - 0.00005369\theta^2 \quad (3.1)$$

The optical losses are associated with five parameters (see Figure 3-1):

- (1) Reflectivity,  $\rho$ : only a fraction of the incident radiation is reflected towards the receiver. The fraction is determined by the reflector type and dirt condition. Reflectivity of commercial parabolic trough mirrors can be assumed to be 0.9 for washed mirrors.
- (2) Intercept factor,  $\gamma$ : a fraction of the direct solar radiation reflected by the mirrors does not reach the glass cover of the absorber tube due to either microscopic imperfections of the reflectors or macroscopic shape errors in the parabolic trough concentrators (e.g., imprecision during assembly). These errors cause reflection of some rays at wrong angles, and therefore they do not intercept the absorber tube. These losses are quantified by an optical parameter called the intercept factor,  $\gamma$ , that is typically 0.95 for a collector properly assembled.
- (3) Transmissivity of the glass tube,  $\tau$ : only a fraction of the direct solar radiation reaching the glass cover of the absorber pipe is able to pass through it. The ratio between the radiation passing through the glass tube and the total incident radiation on it, gives transmissivity  $\tau$ , which is typically 0.93.
- (4) Absorptivity of the absorber selective coating,  $\alpha_{abs}$ : this parameter quantifies the amount of energy absorbed by the steel absorber pipe, compared with the total radiation reaching the outer wall of the steel pipe. This parameter is typically 0.95 for receiver pipes with a cermet coating, whereas it is slightly lower for pipes coated with black nickel or chrome.
- (5) Soiling factor,  $F_e$ : the dirt on reflectors will reduce the reflectivity, it needs to concern the soiling factor. The soiling factor  $F_e$  takes into account the progressive soiling of mirrors and glass tubes after washing.

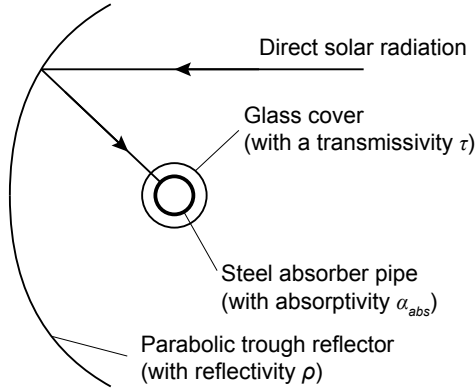


Figure 3-1 Some of the optical parameters of a parabolic trough

The energy passes through the glass tube to the receiver can be expressed by

$$P = I_r w_{tc} L_{tc} \rho \gamma \tau F_e K(\theta) \quad (3.2)$$

The solar energy absorbed by the absorber occurs very close to the outer surface, to simplify the absorption process, it is treated as a uniform heat flux  $q''$ .

$$q'' = \frac{P}{\pi d_o L_{tc}} = \frac{I_r w_{tc} \rho \gamma \tau F_e K(\theta)}{\pi d_o} \quad (3.3)$$

Assume overall heat transfer coefficient  $U(T_{abs})$  is uniform for whole length of the collector, and the heat transfer correlation in Appendix B can be applied. Figure 3-2 shows the schematic diagram of the thermal analysis of the absorber pipe.

$$\frac{T_o - T_{amb} - \frac{q''}{U(T_{abs})}}{T_i - T_{amb} - \frac{q''}{U(T_{abs})}} = \exp\left(-\frac{U(T_{abs}) \pi d_o L_{tc}}{\dot{m} c_p}\right) \quad (3.4)$$

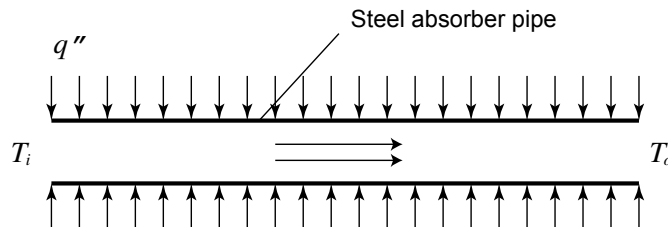


Figure 3-2 Schematic diagram of the absorber pipe

Since the Nusselt number  $Nu$  in the pipe is very large (about  $1 \times 10^4$ ), small temperature difference exists between absorber and oil. So the average fluid temperature  $(T_i + T_o)/2$  can be used as the average value of  $T_{abs}$ , and  $U(T_{abs})$  can be expressed by the a second-order polynomial function given by Romero and Zarza<sup>[104]</sup>. The length  $L_{tc}$  to get the required number of trough collectors in a row can be obtained from Equation (3.4).

The energy projected perpendicularly to the aperture of the trough collectors is

$$Q_{total} = I_r L_{tc} w_{tc} \quad (3.5)$$

The energy absorbed by the heat transfer fluid is

$$Q_{use} = \dot{m} c_p (T_o - T_i) \quad (3.6)$$

The thermal efficiency of the trough collectors

$$\eta_{tc} = \frac{Q_{use}}{Q_{total}} = \frac{I_r L_{tc} w_{tc}}{\dot{m} c_p (T_o - T_i)} \quad (3.7)$$

### 3.1.2 Parabolic dish collector

Parabolic dish collector consists of a reflector and a receiver. The reflector tracks the sun to reflect direct solar radiation and concentrates it onto a receiver located at the focal point of the reflector. Two axes tracking system needs to be applied for the reflector to continuously follow the daily path of the sun.

Two different methods are applied for the sun tracking systems:<sup>[105]</sup>

- Azimuth elevation tracking by an orientation sensor or by calculated coordinates of the sun performed by the local control.
- Polar tracking, where the concentrator rotates about an axis parallel to the earth's axis rotation.

In a traditional dish-Stirling system, a Stirling engine is located at the focal point. The Stirling engine has a receiver to absorb the thermal energy from the concentrated sunlights. The receiver consists of an aperture and an absorber. The aperture in a Stirling receiver is located at the focal point of the reflector to reduce the radiation and convection losses. The absorber absorbs the solar radiation and transfers the thermal energy to the working gas of the Stirling engine. An electrical generator, directly connected to the crankshaft of the engine, converts the mechanical energy into electricity.

In a proposed cascade system, a volumetric receiver is located at the focal point. A spiral tube is located in the receiver to absorb the concentrated solar energy. Air (or nitrogen, is used as the heat transfer fluid) flows through the tube to transfer the absorbed energy as the heat source of Stirling engine(s).

The reflector is a key element of the systems. The curved reflective surface can be manufactured by attached segments, by individual facets or by a stretched membranes shaped by a continuous plenum. In all cases, the curved surface should be coated or covered by aluminum or silver reflectors.

A dish reflector product of SES (Stirling Energy System) is used in this cascade system, and its key parameters can be found in Table 3.1. The structure of the receiver is shown in Figure 3-3.

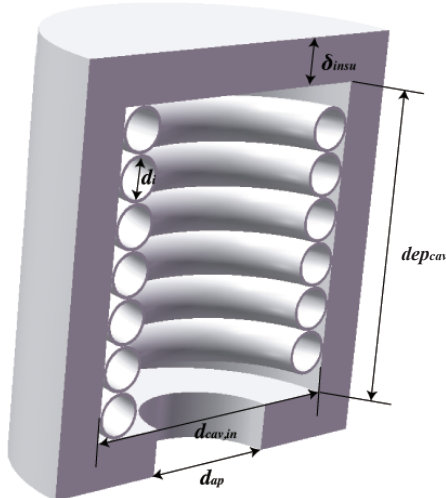


Figure 3-3 The structure of the dish receiver

The dish receiver model concerns the losses include: collector losses due to mirror reflectivity, receiver intercept losses, losses due to shading, and thermal losses. Thermal losses take the largest portion of all those losses, which are due to conduction, convection and radiation. Figure 3-4 shows the thermal network of dish receiver, which concerns the losses:

- Radiation losses reflected off of the receiver cavity surfaces and out of the receiver through the aperture. ( $q_{rad,ref}$ )
- Conductive losses through the receiver insulating layer. ( $q_{cond,tot}$ )

Table 3.1 Key parameters of the dish collector

| Parameter        | Value          | Parameter         | Value               | Parameter        | Value |
|------------------|----------------|-------------------|---------------------|------------------|-------|
| $d_{cav}$        | 0.46 m         | $\epsilon_{insu}$ | 0.6                 | $\theta_{dc}$    | 45°   |
| $\delta_{insu}$  | 0.075 m        | $\alpha_{cav}$    | 0.87                | $\gamma$         | 0.97  |
| $dep_{cav}$      | 0.23 m         | $\delta_a$        | 0.005 m             | $\eta_{shading}$ | 0.95  |
| $d_{ap}$         | 0.184 m        | $d_{i,1}$         | 0.07 m              | $\rho$           | 0.91  |
| $\lambda_{insu}$ | 0.06 W/(m · K) | $A_{dc}$          | 87.7 m <sup>2</sup> |                  |       |

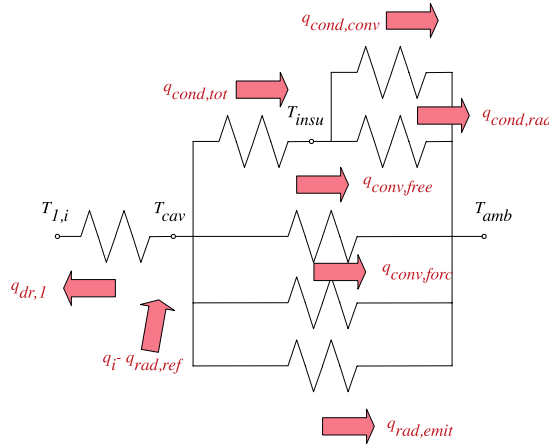


Figure 3-4 Thermal network of dish receiver

- Free convection from the cavity in the absence of wind. ( $q_{conv,free}$ )
- Forced convection in the presence of wind. ( $q_{conv,forc}$ )
- Emission losses due to thermal radiation emitted from the receiver aperture. ( $q_{rad,emit}$ )

To solve the thermal network in Figure 3-4, correlations and relationships of the heat fluxes should be clear.

### (1) Inlet energy from the reflector, $q_i$

To simplify the model, influences made by receiver blocking and imperfection track are ignored.

$$q_i = I_r A_{dc} \gamma \eta_{shading} \rho \quad (3.8)$$

In Equation (3.8),  $\gamma$  is the intercept factor,  $\eta_{shading}$  is the shading factor between different collectors,  $\rho$  is the reflectivity of the reflector.

(2) *Heat exchange between the HTF and the dish absorber,  $q_{dr,1}$*

The heat transfer process between the HTF and the dish absorber is simplified to a heat exchange process of a flow in a uniform temperature heat pipe. So  $q_{dr,1}$  can be written as

$$q_{dr,1} = h_{dr,1} A_{dr,1} \Delta T_{ln,dr,1} \quad (3.9)$$

where

$$h_{dr,1} = Nu_{tube} \lambda_{dr,1} / d_{i,1} \quad (3.10)$$

$$Nu_{tube} = c_r Nu'_{tube} \quad (3.11)$$

For helical spiral pipe, multiplier  $c_r$  based on curvature ratio can be expressed as<sup>[106]</sup>

$$c_r = 1 + 3.5 \frac{d_{i,1}}{d_{cav} - d_{i,1} - 2\delta_a} \quad (3.12)$$

$Nu'_{tube}$  is the Nusselt number of straight circular tube, which can be expressed by<sup>[107]</sup>

$$Nu'_{tube} = 0.027 Re_{tube}^{0.8} Pr_{tube}^{1/3} (\mu_{tube} / \mu_{tube,w})^{0.14} \quad (3.13)$$

and the logarithmic mean temperature difference  $\Delta T_{ln,dr,1}$  can be written as

$$\Delta T_{ln,dr,1} = \frac{(T_{cav} - T_{dc,i}) - (T_{cav} - T_{dc,o})}{\ln \frac{T_{cav} - T_{dc,i}}{T_{cav} - T_{dc,o}}} \quad (3.14)$$

(3) *Radiation losses reflected off the receiver,  $q_{rad,ref}$*

$$q_{rad,ref} = (1 - \alpha_{eff}) q_i \quad (3.15)$$

where  $\alpha_{eff}$  is the effective absorptivity of the receiver.

$$\alpha_{eff} = \frac{\alpha_{cav}}{\alpha_{cav} + (1 - \alpha_{cav}) \frac{A_{ap}}{A_{cav}}} \quad (3.16)$$

$\alpha_{cav}$  is the absorptivity of the cavity,  $A_{cav}$  is the cavity area,  $A_{ap}$  is the aperture area.

(4) *Conductive losses through the receiver insulating layer,  $q_{cond,tot}$*

$$q_{cond,tot} = 2\pi\lambda_{insu}dep_{cav} \frac{T_{cav} - T_{insu}}{\ln(1 + 2\delta_{insu}/d_{cav})} \quad (3.17)$$

where  $T_{cav}$  is the temperature of the cavity wall,  $T_{insu}$  is outside temperature of the insulation wall.

(5) *Convection losses from the receiver insulating layer,  $q_{cond,conv}$*

$$q_{cond,conv} = h_{insu}A_{insu}(T_{insu} - T_{amb}) = \frac{k_{insu}Nu_{insu}A_{insu}(T_{insu} - T_{amb})}{d_{cav} + 2\delta_{insu}} \quad (3.18)$$

where  $Nu_{insu}$  can be obtained from the correlation for flow over a circular cylinder.<sup>[108]</sup>

(6) *Radiation losses from the receiver insulating layer,  $q_{cond,rad}$*

$$q_{cond,rad} = \epsilon_{insu}A_{insu}\sigma(T_{insu}^4 - T_{amb}^4) \quad (3.19)$$

(7) *Free convection from the cavity in the absence of wind,  $q_{conv,free}$*

Ma<sup>[109]</sup> conducted tests to determine the free convection losses from the receiver for alternative setups, and the data were consistent with Stine and McDonald's free convection correlation. It is assumed that forced convection is independent of free convection in the receiver, so the total convection losses can be represented as the total of the free and forced convection losses as shown in Figure 3-4.

$$q_{conv,free} = h_{free}A_{cav}(T_{cav} - T_{amb}) \quad (3.20)$$

where  $h_{free} = k_{film}Nu_{free}/\overline{d_{cav}}$ ,  $\overline{d_{cav}}$  is the effective diameter of the cavity,  $\overline{d_{cav}} = d_{cav} - 2d_i - 4\delta_a$ .  $d_i = 0.066 \text{ m}$

(8) *Force convection from the cavity in the presence of wind,  $q_{conv,forc}$*

$$q_{conv,forc} = h_{forc}A_{cav}(T_{cav} - T_{amb}) \quad (3.21)$$

Wu et al.<sup>[110]</sup> present a comprehensive review and systematic summarization of convection heat loss from cavity receiver in parabolic dish solar thermal power system. And we choose the correlation presented by Leibfried and Ortjohann<sup>[111]</sup>. This correlation gives an extended model of Koenig and Marvin<sup>[112]</sup> and Stine and Diver<sup>[113]</sup> with better results.

For forced convection loss, side-on wind convection loss model given by Ma<sup>[109]</sup>, which is independent of the aperture orientation, is used

$$h_{forc} = 0.1967v_{wind}^{1.849} \quad (3.22)$$

(9) *Emission losses due to thermal radiation emitted from the receiver aperture,  $q_{rad,emit}$*

The emissivity is set equal to the effective absorptivity of the cavity (gray body),

$$\epsilon_{cav} = \alpha_{eff} \quad (3.23)$$

$$q_{rad,emit} = \epsilon_{cav} A_{ap} \sigma (T_{cav}^4 - T_{amb}^4) \quad (3.24)$$

From Figure 3-4, it can be found that

$$q_{eff} = q_i - q_{rad,ref} \quad (3.25)$$

$$q_{eff} = q_{dr,1} + q_{cond,tot} + q_{conv,free} + q_{conv,forc} + q_{rad,emit} \quad (3.26)$$

$$q_{cond,tot} = q_{cond,conv} + q_{cond,rad} \quad (3.27)$$

So the temperature nodes in the thermal network can be solved by these equations.

$q_{dr,1}$  can be obtained from Equation (3.9), and efficiency of the dish receiver

$$\eta_{dr} = \frac{q_{dr,1}}{q_i} \quad (3.28)$$

Efficiency of the dish collector

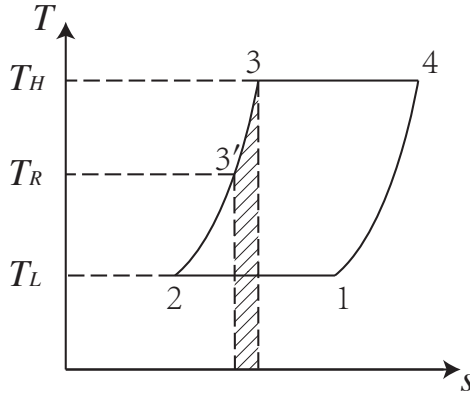
$$\eta_{dc} = \frac{q_{dr,1}}{I_r A_{dc}} \quad (3.29)$$

### 3.1.3 Stirling engine

#### 3.1.3.1 Theoretical Stirling cycle

In a Stirling cycle, there are two isothermal processes that exchange heat with heating and cooling fluids, two isochoric processes that exchange heat with regenerator. Figure 3-5 shows the  $T-s$  diagram of a typical Stirling cycle. The heat absorbed by regenerator in process 4-1 is reused in process 2-3, but only able to heat the working gas from 2 to 3' due to the imperfect regeneration.  $e$  is defined as the regenerator effectiveness<sup>[114,115]</sup>,  $e = \frac{T_R - T_L}{T_H - T_L}$ , where  $T_H$  is the temperature in the hot space,  $T_L$  is the temperature in the cold space,  $T_R$  is the effective working fluid temperature in the regenerator.

In order to obtain a simplified analytical model, several simplifications are made:


 Figure 3-5  $T$ - $s$  diagram of a Stirling cycle

- The working gas in Stirling engines obeys the ideal gas law.
- No heat loss to the environment for Stirling engines.
- Overall heat transfer coefficients of the fluids are constant.
- A symmetrical regenerator behavior is assumed so that a simple effectiveness can be obtained by  $T_R = \frac{T_H - T_L}{\ln(T_H/T_L)}$ .<sup>[114,115]</sup>

To consider internal irreversibilities in a Stirling cycle made by dead volumes, total dead volume  $V_D$  can be divided into heater dead volume  $V_{DH}$ , regenerator dead volume  $V_{DR}$  and cooler dead volume  $V_{DC}$ .<sup>[116]</sup> There exists a factor  $K$  to describe the dead volumes under different temperatures.  $K$  is relevant with temperatures in the process and regenerator effectiveness.

$$K = \frac{V_{DH}}{T_H} + \frac{V_{DR}}{T_R} + \frac{V_{DC}}{T_L} \quad (3.30)$$

For the isothermal compression process 1-2, the output work

$$W_{12} = \int_{V_E+V_C}^{V_E} p_{12} dV = -mRT_L \ln \frac{V_E + V_C + KT_L}{V_E + KT_L} \quad (3.31)$$

For the isothermal expansion process 3-4, the output work

$$W_{34} = \int_{V_E}^{V_E+V_C} p_{34} dV = mRT_H \ln \frac{V_E + V_C + KT_H}{V_E + KT_H} \quad (3.32)$$

Define  $\gamma_H = \frac{V_E + V_C + KT_H}{V_E + KT_H}$ , and  $\gamma_L = \frac{V_E + V_C + KT_L}{V_E + KT_L}$ . In a cycle, the theoretical output work

$$W_{th} = W_{12} + W_{34} = mR(T_H \ln \gamma_H - T_L \ln \gamma_L) \quad (3.33)$$

For the isochoric heating process 3'-3, the absorbed heat

$$Q_{3'3} = nc_v(T_H - T_R) = \frac{1-e}{k-1}mR(T_H - T_L) \quad (3.35)$$

For the isothermal expansion process 3-4, the absorbed heat

$$Q_{34} = W_{34} = mRT_H \ln \gamma_H \quad (3.36)$$

In a cycle, the theoretical absorbed heat

$$Q_{th} = Q_{3'3} + Q_{34} = \frac{1-e}{k-1}mR(T_H - T_L) + mRT_H \ln \gamma_H \quad (3.37)$$

### 3.1.3.2 Irreversibilities and losses

#### (1) Non-ideal heat transfer effect

Because of non-ideal heater and cooler, the working fluid temperature ( $T_H/T_L$ ) in these two heat exchangers is less/higher than the wall temperature ( $T_{hw}/T_{cw}$ ), respectively.  $T_H$  and  $T_L$  can be corrected by the wall temperatures as follows:

$$T_H = T_{hw} - \frac{Qs_{se}}{h_h A_{hw}} \quad (3.38)$$

$$T_L = T_{cw} + \frac{(Q-W)s_{se}}{h_c A_{cw}} \quad (3.39)$$

The heat transfer coefficient can be obtained using the following correlation<sup>[1]</sup>:

$$h_{h,c} = \frac{\mu c_p f_{Re}}{2D_{h,c} Pr_{h,c}} \quad (3.40)$$

where  $f_{Re}$  is a Reynolds friction factor defined as:

$$f_{Re} = 0.0791 Re_{h,c}^{0.75} \quad (3.41)$$

$Re_{h,c}$ ,  $Pr_{h,c}$  and  $D_{h,c}$  are Reynolds number, Prandtl number and hydraulic diameter of the heater/cooler exchanger.

(2) Effect of pressure drop

Pressure drops in the heat exchangers cause power losses of the Stirling engine. The pressure drops can be expressed by:<sup>[117]</sup>

$$\Delta p = -\frac{2f_{Re}\mu uV}{d^2 A} \quad (3.42)$$

where  $u$  is the working gas speed,  $V$  is volume,  $A$  is flow cross-section area.

The net power loss of the Stirling engine due to pressure drop of the heat exchangers can be evaluated by:

$$W_{pd} = \oint \sum_{i=E,C} (\Delta p_i \frac{dV_i}{d\theta}) d\theta \quad (3.43)$$

(3) Effect of finite speed of piston and mechanical friction

Due to the finite speed of piston, the pressure on the piston surface is different from the pressure of expansion and compression spaces. It has been demonstrated that the pressure on the piston surface in the expansion process is less than the mean pressure in the expansion space. Similarly, the pressure on the piston surface in the compression process is greater than the mean pressure in the compression space. This means the output work is less than the theoretical value. Besides, The output work also reduces due to mechanical friction. The output work loss due to finite speed of piston and mechanical friction can be obtained as follows:<sup>[1]</sup>

$$W_{fs} = \oint p(\pm \frac{au_p}{c} \pm \frac{\Delta p_f}{p}) dV \quad (3.44)$$

where the sign (+) is used in the compression space, and the sign (-) is used in the expansion space.  $p$  is the mean pressure in the compression/expansion space,  $u_p$  is velocity of the piston,  $c$  is the average speed of molecules and  $\Delta p_f$  is the pressure loss due to mechanical friction.  $\Delta p_f$ ,  $a$  and  $c$  can be expressed by:<sup>[118]</sup>

$$\Delta p_f = 0.97 + 0.009 s_{se} \quad (3.45)$$

$$a = \sqrt{3k} \quad (3.46)$$

$$c = \sqrt{3RT} \quad (3.47)$$

(4) Energy losses due to internal conduction

The temperature differs from the heater and cooler, heat losses from heater to cooler exists due to internal conduction through the walls of regenerator.<sup>[119]</sup> The internal conduction loss in a cycle can be expressed by follows:

$$Q_{id} = \frac{k_r A_r}{L_r s_{se}} (T_{hw} - T_{cw}) \quad (3.48)$$

where,  $k_r$ ,  $A_r$  and  $L_r$  denote the regenerator matrix conductivity, regenerator length, and regenerator conductive area respectively.

(5) Energy losses due to shuttle conduction

The displacer shuttles between the expansion and compression space. It absorbs heat during the hot end of its stroke and releases it during the cold end of its stroke. This heat loss can be estimated as<sup>[120]</sup>:

$$Q_{sc} = 0.4 \frac{Z^2 k_p D_p}{J L_d s_{se}} (T_H - T_L) \quad (3.49)$$

where,  $Z$ ,  $k_p$ ,  $D_p$ ,  $J$  and  $L_d$  denote the displacer stroke, piston thermal conductivity, displacer diameter, gap between the displacer and the cylinder, and length of the displacer respectively.

So, in a Stirling engine, the total absorbed heat in a cycle

$$Q = Q_{th} + Q_{id} + Q_{sc} \quad (3.50)$$

the output work

$$W = W_{th} - W_{pd} - W_{fs} \quad (3.51)$$

Power of the Stirling engine

$$P = W s_{se} \quad (3.52)$$

Efficiency of the Stirling engine

$$\eta = W/Q \quad (3.53)$$

### 3.1.3.3 Model validation

Evaluation of the developed thermal model is performed by considering the GPU-3 Stirling engine as a case study. Design specifications of the GPU-3 Stirling engine are indicated

Table 3.2 Design specifications of the GPU-3 Stirling engine<sup>[1,2]</sup>

| Parameter                              | Value                             |
|--|-----------------------------------|
| Engine type                            | $\beta$                           |
| Working gas                            | Helium                            |
| Mass of the working gas                | 1.136 g                           |
| <i>Heater</i>                          |                                   |
| Number of tubes                        | 40                                |
| Tube external diameter                 | $4.83 \times 10^{-3}$ m           |
| Tube internal diameter                 | $3.02 \times 10^{-3}$ m           |
| Tube length (cylinder side)            | 0.1164 m                          |
| Tube length (regenerator side)         | 0.1289 m                          |
| <i>Cooler</i>                          |                                   |
| Number of tubes                        | 312                               |
| Tube external diameter                 | $1.59 \times 10^{-3}$ m           |
| Tube internal diameter                 | $1.09 \times 10^{-3}$ m           |
| Average tube length                    | $4.61 \times 10^{-2}$ m           |
| <i>Regenerator</i>                     |                                   |
| Number of regenerator                  | 8                                 |
| Regenerator internal diameter          | $2.26 \times 10^{-2}$ m           |
| Regenerator length                     | $2.26 \times 10^{-2}$ m           |
| Diameter of regenerator tube           | $4 \times 10^{-5}$ m              |
| Material                               | Stainless steel                   |
| <i>Volume</i>                          |                                   |
| Swept Vol. (expansion/compression)     | 120.82/114.13 cm <sup>3</sup>     |
| Clearance Vol. (expansion/compression) | 30.52/28.68 cm <sup>3</sup>       |
| Dead Vol. (heater/cooler/regenerator)  | 70.28/13.18/50.55 cm <sup>3</sup> |

Table 3.3 Thermal efficiency of the models and experimental data (at  $T_{hw} = 922\text{ K}$  and  $T_{cw} = 288\text{ K}$ )

| Rotation speed (Hz) | Mean effective pressure (MPa) | The simple analysis (variable $\Pr^{[117]}$ ) |           |                   | The adiabatic analysis (simple II <sup>[119]</sup> ) |           |                   | The proposed Stirling engine model |           |                   | Experimental efficiency <sup>[1]</sup><br>Actual value (%) |
|---------------------|-------------------------------|---|-----------|-------------------|--|-----------|-------------------|------------------------------------|-----------|-------------------|--|
|                     |                               | Value (%)                                     | Error (%) | Average error (%) | Value (%)  | Error (%) | Average error (%) | Value (%)                          | Error (%) | Average error (%) |  |
| 16.67               | 38.72                         | 18.22   | 32.48     | 11.98             | 28.16  | 7.66      | 20.50             |                                    |           |                   |  |
| 25.00               | 36.16                         | 15.46   | 31.21     | 10.51             | 27.75  | 7.05      | 20.70             |                                    |           |                   |  |
| 33.33               | 33.79                         | 15.79   | 29.45     | 11.45             | 27.43  | 9.43      | 18.00             |                                    |           |                   |  |
| 41.67               | 2.76                          | 31.48   | 16.28     | 17.90             | 27.45  | 12.25     | 27.17             | 11.97                              | 12.10     | 15.20             |  |
| 50.00               |                               | 29.12   | 17.32     |                   | 25.21  | 13.41     | 26.94             | 15.14                              |           | 11.80             |  |
| 58.33               |                               | 29.74   | 24.34     |                   | 22.89  | 17.49     | 26.74             | 21.34                              |           | 5.40              |  |
| 25.00               | 35.65                         | 10.85   | 32.29     | 7.49              | 27.29  | 2.49      | 24.80             |                                    |           |                   |  |
| 33.33               | 33.52                         | 9.62  | 30.40     | 6.50              | 26.94  | 3.04      | 23.90             |                                    |           |                   |  |
| 41.67               | 4.14                          | 31.48   | 10.18     | 11.46             | 28.39  | 7.09      | 8.28              | 26.65                              | 5.35      | 6.65              | 21.30  |
| 50.00               |                               | 29.45   | 11.25     |                   | 26.33  | 8.13      | 26.39             | 8.19                               |           | 18.20             |  |
| 58.33               |                               | 27.40   | 15.40     |                   | 24.21  | 12.21     | 26.17             | 14.17                              |           | 12.00             |  |
| 41.67               | 31.20                         | 8.70  | 28.59     | 6.09              | 26.24  | 3.74      | 22.50             |                                    |           |                   |  |
| 50.00               | 5.52                          | 29.33   | 10.53     | 10.82             | 26.62  | 7.82      | 8.11              | 25.97                              | 7.17      | 7.48              | 18.80  |
| 58.33               |                               | 27.44   | 13.24     |                   | 24.62  | 10.42     | 25.73             | 11.53                              |           | 14.20             |  |
| 50.00               | 29.07                         | 10.37   | 26.61     | 7.91              | 25.62  | 6.92      | 18.70             |                                    |           |                   |  |
| 58.33               | 6.90                          | 27.29   | 13.09     | 11.73             | 24.67  | 10.47     | 9.19              | 25.37                              | 11.17     | 9.05              | 14.20  |

Table 3.4 Output power of the models and experimental data (at  $T_{hw} = 922\text{K}$  and  $T_{cw} = 288\text{K}$ )

| Rotation speed<br>(Hz) | Mean effective<br>pressure<br>(MPa) | The simple analysis<br>(variable Pr <sup>[117]</sup> ) |              |                         | The adiabatic analysis<br>(simple II <sup>[119]</sup> ) |              |                         | The proposed Stirling<br>engine model |              |                         | Experiment<br>(kW) <sup>[1]</sup><br>(kW) |
|------------------------|-------------------------------------|--|--------------|-------------------------|---|--------------|-------------------------|---------------------------------------|--------------|-------------------------|---|
|                        |                                     | Value<br>(kW)  | Error<br>(%) | Average<br>error<br>(%) | Value<br>(kW)   | Error<br>(%) | Average<br>error<br>(%) | Value<br>(kW)                         | Error<br>(%) | Average<br>error<br>(%) |   |
| 16.67                  | 1.796                               | 119.02   |              | 1.772                   | 116.10  |              | 0.861                   | 4.98                                  |              | 0.82                    |   |
| 25.00                  | 2.555                               | 128.13   |              | 2.500                   | 123.21  |              | 1.253                   | 11.88                                 |              | 1.12                    |   |
| 33.33                  | 3.215                               | 165.70   |              | 3.117                   | 157.60  |              | 1.632                   | 34.88                                 |              | 1.21                    |   |
| 41.67                  | 3.769                               | 211.49   |              | 3.615                   | 198.76  |              | 2.001                   | 65.37                                 |              | 1.21                    |   |
| 50.00                  | 4.195                               | 303.37   |              | 3.973                   | 282.08  |              | 2.362                   | 127.12                                |              | 1.04                    |   |
| 58.33                  | 4.505                               | 704.46   |              | 4.203                   | 650.54  |              | 2.715                   | 384.82                                |              | 0.56                    |   |
| 25.00                  | 3.844                               | 114.75   |              | 3.761                   | 110.11  |              | 1.818                   | 1.56                                  |              | 1.79                    |   |
| 33.33                  | 4.856                               | 120.73   |              | 4.708                   | 114.00  |              | 2.362                   | 7.36                                  |              | 2.20                    |   |
| 41.67                  | 4.14                                | 5.734  | 136.94       | 259.70                  | 5.501   | 127.31       | 158.41                  | 2.890                                 | 19.42        | 39.83                   | 2.42                                      |
| 50.00                  | 6.462                               | 174.98   |              | 6.126                   | 160.68  |              | 3.405                   | 44.89                                 |              | 2.35                    |   |
| 58.33                  | 7.030                               | 306.36   |              | 6.573                   | 279.94  |              | 3.908                   | 125.90                                |              | 1.73                    |   |
| 41.67                  | 7.645                               | 133.08   |              | 7.334                   | 123.60  |              | 3.742                   | 14.09                                 |              | 3.28                    |   |
| 50.00                  | 5.52                                | 8.655  | 163.87       | 180.02                  | 8.206   | 150.18       | 164.91                  | 4.401                                 | 34.18        | 43.68                   | 3.28                                      |
| 58.33                  | 9.470                               | 243.12   |              | 8.858                   | 220.94  |              | 5.045                   | 82.79                                 |              | 2.76                    |   |
| 50.00                  | 6.90                                | 10.788   | 174.50       | 287.04                  | 10.223  | 160.13       | 263.63                  | 5.362                                 | 36.44        | 97.75                   | 3.93                                      |
| 58.33                  | 11.840                              | 399.58   |              | 11.071                  | 367.13  |              | 6.140                   | 159.07                                |              | 2.37                    |   |

in Table 3.2. The thermal efficiency and power of the proposed Stirling engine model are compared with previous thermal models and experimental data as shown in Table 3.3 and Table 3.4.

It can be found that the proposed model has much better agreement with the experimental results than previous thermal models at various rotation speeds and mean effective pressures. It is required to mention that in all thermal models both power  $W$  and input heat  $Q$  are determined by the thermal process of heat transfer between the wall and working gas. In the proposed model,  $W$  and  $Q$  are obtained from Equation (3.38) and (3.39). Therefore all the three parameters  $W$ ,  $Q$  and  $\eta$  are determined by the thermal model and input parameters to the model. These input parameters includes heater, cooler, mean effective pressure, type of working gas and geometrical specification of the engine.

Table 3.3 and 3.4 indicate that when mean effective pressure of the engine increases from 2.76 MPa to 6.90 MPa, best performance (efficiency and power) prediction of the proposed model exists. When rotation speed increases from 16.67 Hz to 58.33 Hz, error in prediction of performance of the proposed model increases. The proposed model may have the best performance prediction at a low rotation speed, with mean effective pressure between 4.14 MPa and 5.52 MPa.

However, there is still some discrepancy between the simulation results of proposed model and the experimental data. In the future researches, more accurate models of Stirling engine may be developed by considering other irreversibilities such as heat loss to the environment, gas spring hysteresis, and etc. It is worth pointing that there are more accurate Stirling engine models. For example, polytropic simulation models of Stirling engine show higher accuracy than our proposed model<sup>[1,121]</sup>. However, the model needs more costly calculations and the polytropic indexes are engine-specific.

### 3.1.3.4 Heat transfer between the engine and the fluids

For a Stirling engine thermal process, the wall temperatures of the heater and cooler are considered to be uniform and constant. The heat transferred between the wall and the fluids after a contact area of  $dA$  is

$$(T_w - T)UdA = \dot{m}c_p dT \quad (3.54)$$

$$\frac{dT}{T - T_w} = - \frac{U dA}{\dot{m} c_p} \quad (3.55)$$

With  $T(0) = T_i$ ,  $T(A) = T_o$ ,

$$\frac{T_o - T_w}{T_i - T_w} = \exp\left(-\frac{U A}{\dot{m} c_p}\right) \quad (3.56)$$

For a Stirling engine,  $T_{hw}$  or  $T_{cw}$  can be used to substitute  $T_w$  to get the relationships between  $T_{i,h}$ ,  $T_{o,h}$  and  $T_{hw}$ , or  $T_{i,c}$ ,  $T_{o,c}$  and  $T_{cw}$  respectively.

$$\frac{T_{o,h} - T_{hw}}{T_{i,h} - T_{hw}} = \exp\left(-\frac{U_h A_h}{\dot{m}_h c_{p,h}}\right) \quad (3.57)$$

$$\frac{T_{o,c} - T_{cw}}{T_{i,c} - T_{cw}} = \exp\left(-\frac{U_c A_c}{\dot{m}_c c_{p,c}}\right) \quad (3.58)$$

Heat transferred from heating fluid to Stirling engine in a cycle

$$\dot{m}_h c_{p,h} (T_{i,h} - T_{o,h}) / s_{se} = Q \quad (3.59)$$

Heat transferred from Stirling engine to cooling fluid in a cycle

$$\dot{m}_c c_{p,c} (T_{o,c} - T_{i,c}) / s_{se} = Q - W \quad (3.60)$$

### 3.1.4 Rankine power generation system

Based on different working fluids, there are two different kinds of Rankine power generation systems, steam Rankine power generation system and organic Rankine power generation.

#### 3.1.4.1 Steam Rankine cycle

For steam Rankine cycle, a deaerator is used to remove the oxygen and other non-condensable gases in the feedwater of steam generating system. Dissolved oxygen in feedwater will cause serious corrosion damage in steam generating system by forming oxides (rust) of the metal pipes. Dissolved carbon dioxide combines with water to form carbonic acid will cause further corrosion. The accumulation of the non-condensable gases will increase

the heat transfer resistance, which is harmful for the heat exchangers. The extraction of the steam turbine provides heat for the deaerator.

Figure 3-6a shows the  $T-s$  diagram of the water circuit in the cascade system in Figure 3-11. Process 2a-2c-2b shows the heat process in the steam turbine (see Figure 3-6b). State point 2b and  $i, 2b$  have the same pressure, state point 2c and  $i, 2c$  have the same pressure. To simplify the inner process 2a-2c-2b of the turbine, same isentropic efficiency of steam turbine with different loads and in different stages is assumed, which means

$$\eta_{i,tb} = (h_{2a} - h_{2b}) / (h_{2a} - h_{i,2b}) = (h_{2a} - h_{2c}) / (h_{2a} - h_{i,2c}) \quad (3.61)$$

where  $h_{i,2b}$  is determined by  $s_{2a}$  and  $p_c$ ;  $h_{i,2c}$  is determined by  $s_{2a}$  and  $p_e$ .

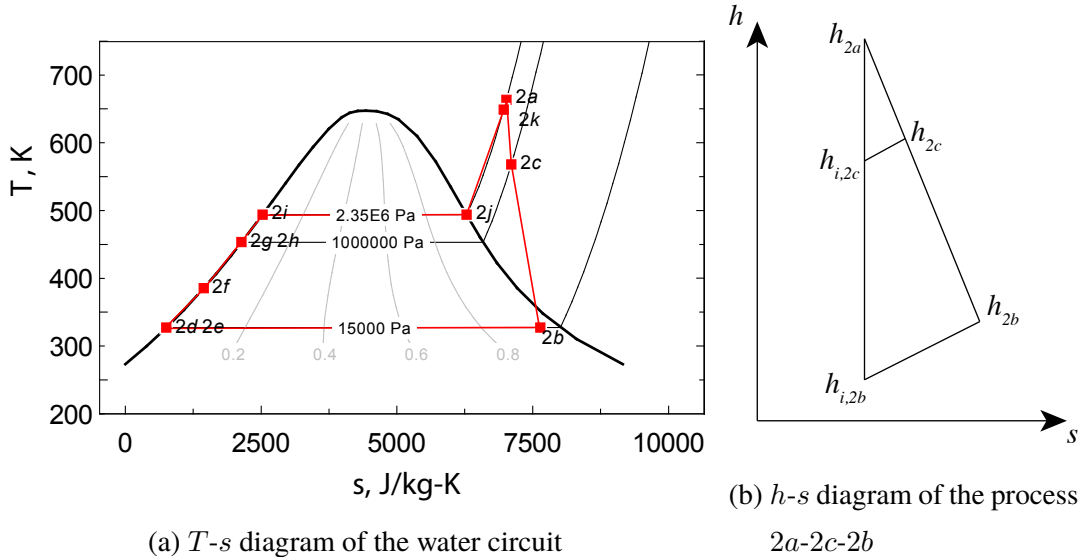


Figure 3-6  $T-s$  diagram of the water circuit and  $h-s$  diagram of the process 2a-2b

The output power of the steam turbine

$$P_{tb} = (1 - y) \dot{m}_2 (h_{2a} - h_{2b}) + y \dot{m}_2 (h_{2a} - h_{2c}) \quad (3.62)$$

Process 2b-2d shows the heat process in the condenser. The outlet water in the condenser is saturated water. The outlet temperature  $T_{2d}$  and outlet enthalpy  $h_{2d}$  are determined by the exhaust pressure of the turbine  $p_c$ . The released heat of the condenser

$$Q_{cd} = (1 - y) \dot{m}_2 (h_{2b} - h_{2d}) \quad (3.63)$$

State points  $2c$ ,  $2f$  and  $2g$  have the same pressure ( $p_e$ , 1 MPa). The water at the outlet of the deaerator is saturated fluid, its enthalpy is determined.

$$yh_{2c} + (1 - y)h_{2f} = h_{2g} \quad (3.64)$$

The total power of the pumps

$$P_{pu} = (1 - y)\dot{m}_2(h_{2e} - h_{2d}) + \dot{m}_2(h_{2h} - h_{2g}) \quad (3.65)$$

where  $h_{2e}$  can be obtained from  $\eta_{pu} = (h_{i,2e} - h_{2d})/(h_{2e} - h_{2d})$ ,  $h_{2h}$  can be obtained from  $\eta_{pu} = (h_{i,2h} - h_{2g})/(h_{2h} - h_{2g})$ .  $h_{i,2e}$  is determined by  $s_{2d}$  and  $p_e$ ,  $h_{i,2h}$  is determined by  $s_{2g}$  and  $p_s$ .

The outlet water of the deaerator is saturated water ( $x = 0$ ), so the outlet temperature  $T_{2g}$  and outlet enthalpy  $h_{2g}$  of the heated fluid is determined by pressure  $p_{2g}$ . For the deaerator, the outlet pressure equals to any of the inlet pressure.

$$p_{2g} = p_{2c} \quad (3.66)$$

Heat injected in the water circuit

$$Q_2 = (1 - y)\dot{m}_2(h_{2f} - h_{2e}) + \dot{m}_2(h_{2a} - h_{2h}) \quad (3.67)$$

The efficiency of Rankine cycle can be expressed as

$$\eta_{rk} = (P_{tb} - P_{pu}/\eta_{ge})/Q_2 \quad (3.68)$$

### 3.1.4.2 Organic Rankine cycle

Compared with steam Rankine cycle, ORC has the following features:

- (1) Organic fluid has lower boiling point, and higher evaporation pressure. It is suitable for the recovery of low temperature waste heat. Besides, it has small density and specific heat capacity, the required size of turbine, pipes and heat transfer areas are small, which is beneficial for cost saving.
- (2) The exhaust fluid of the turbine is dry. So without overheating, the saturated gas can be used as the main gas for the turbine. The corrosion situation caused by the impact of the droplets to the high-speed rotating blades will not happen with ORC.

- (3) Organic fluid has lower sound speed than vapor, the turbine can achieve favorable aerodynamic performance with lower wheel speed.
- (4) Organic fluid has higher condensing pressure than water. It can condense under the pressure higher than the atmosphere. The system pressure can be maintained above the atmosphere pressure to prevent air leak into the system. This means a deaerator is no more necessary.
- (5) Organic fluid has low freezing point, no anti-freezing treatment is required even in the cold area.

The shapes of curves in the  $T-s$  diagram of different fluids are different. According to the saturated vapor curve  $dT/ds$  in the  $T-s$  diagram, the working fluid can be divided into three types:  $dT/ds > 0$  means dry fluid (moisture does not form when high-pressure saturated vapor expanded reversibly from a high pressure), most of the organic fluid are dry fluids;  $dT/ds < 0$  means wet fluid (moisture forms when high-pressure saturated vapor expanded reversibly from a high pressure), such as water;  $dT/ds \rightarrow \pm\infty$  means isentropic fluid, such as R134a. For the high temperature high pressure dry fluid and isentropic fluid, since there is no droplets after work in the expansion turbine, no superheater is required. On the other hand, since the purpose of the ORC focuses on the recovery of low grade heat power, a superheated approach like the traditional Rankine cycle is not appropriate.

Figure 3-7 shows the  $T-s$  diagram of steam Rankine cycle and ORC cycle. Figure 3-8 shows the schematic diagram of the ORC system. For a dry fluid, the cycle can be improved by the use of a regenerator: since the fluid has not reached the two-phase state at the end of the expansion, its temperature at this point is higher than the condensing temperature. This higher temperature fluid can be used to preheat the liquid before it enters the evaporator. A counter-current heat exchanger is thus installed between the expander outlet and the evaporator inlet. The power required from the heat source is therefore reduced and the efficiency is increased.

#### The isentropic efficiency of the turbine

$$\eta_{i,tb} = (h_{4a} - h_{4b}) / (h_{4a} - h_{i,4b}) \quad (3.69)$$

where  $h_{i,4b}$  is determined by  $s_{4a}$  and  $p_c$ .

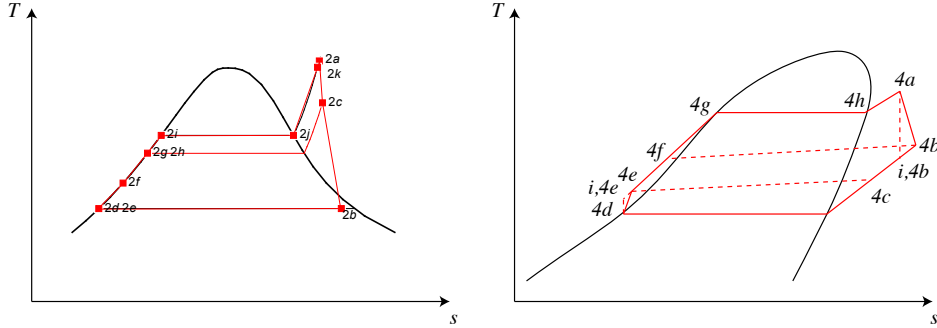


Figure 3-7  $T$ - $s$  diagram of water and a typical organic fluid in Rankine cycles

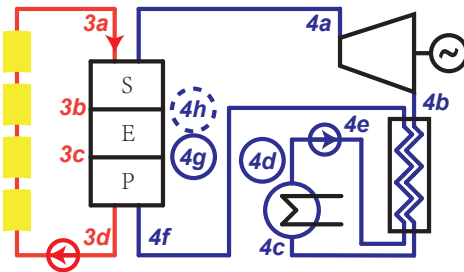


Figure 3-8 The schematic diagram of an ORC system with regenerator

The output power of the turbine

$$P_{tb} = \dot{m}_4(h_{4a} - h_{4b}) \quad (3.70)$$

Process 4c-4d shows the heat process in the condenser. The outlet fluid of the condenser is saturated liquid. The outlet temperature  $T_{4d}$  and outlet enthalpy  $h_{4d}$  are determined by the exhaust pressure of the turbine  $p_c$ .

For the regenerator,

$$h_{4b} - h_{4c} = h_{4f} - h_{4e} \quad (3.71)$$

The released heat of the condenser

$$Q_{cd} = \dot{m}_4(h_{4c} - h_{4d}) \quad (3.72)$$

The power of the pump

$$P_{pu} = \dot{m}_4(h_{4e} - h_{4d}) \quad (3.73)$$

where  $h_{4e}$  can be obtained from  $\eta_{pu} = (h_{i,4e} - h_{4d})/(h_{4e} - h_{4d})$ .  $h_{i,4e}$  is determined by  $s_{4d}$  and  $p_s$ .

Heat injected in the circuit

$$Q_4 = \dot{m}_4(h_{4a} - h_{4f}) \quad (3.74)$$

The efficiency of Rankine cycle can be expressed as

$$\eta_{rk} = \frac{P_{tb} - P_{pu}/\eta_{ge}}{\dot{m}_4(h_{4a} - h_{4f})} \quad (3.75)$$

### 3.1.4.3 Generator

The generator is relatively independent of the cascade system and its efficiency is assumed to be a constant value, 0.975.

## 3.2 Stirling engine array modeling

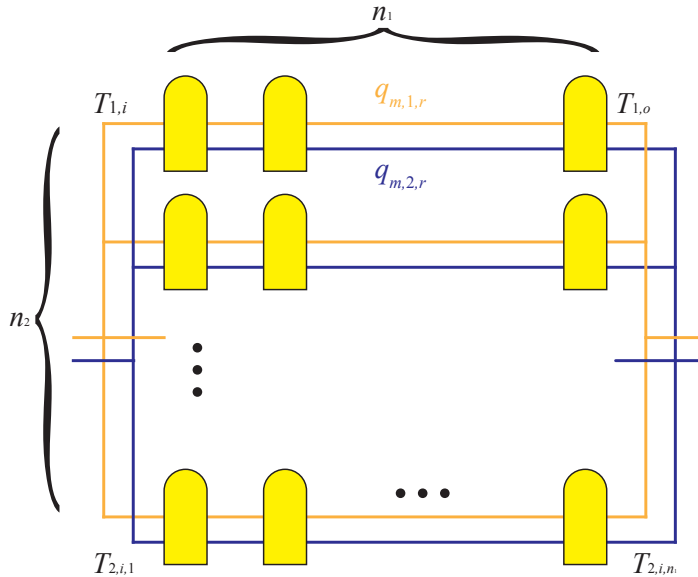


Figure 3-9 Layout of Stirling engines

Stirling engine array is used in the cascade system, Figure 3-9 shows the layout of a Stirling engine array. Each Stirling engine in the Stirling engine array has the identical parameters:  $U_{se,1} = 30 \text{ W}/(\text{m}^2 \cdot \text{K})$ ,  $U_{se,2} = 150 \text{ W}/(\text{m}^2 \cdot \text{K})$ ,  $A_{se,1} = 6 \text{ m}^2$ ,  $A_{se,2} = 6 \text{ m}^2$ ,  $k_{se} = 1.4$ ,  $\gamma_{se} = 3.375$ ,  $n_g = 7.84 \times 10^{-2} \text{ mol}$ ,  $s_{se} = 10 \text{ s}^{-1}$ .

Depending on the direction of heating and cooling flows, there are two possible flow types: parallel flow and counterflow. Figure 3-10 and Figure 3-10b show the heat transfer diagrams of the two flow types.  $n_1$  is chosen to be 10 and can be optimized later.

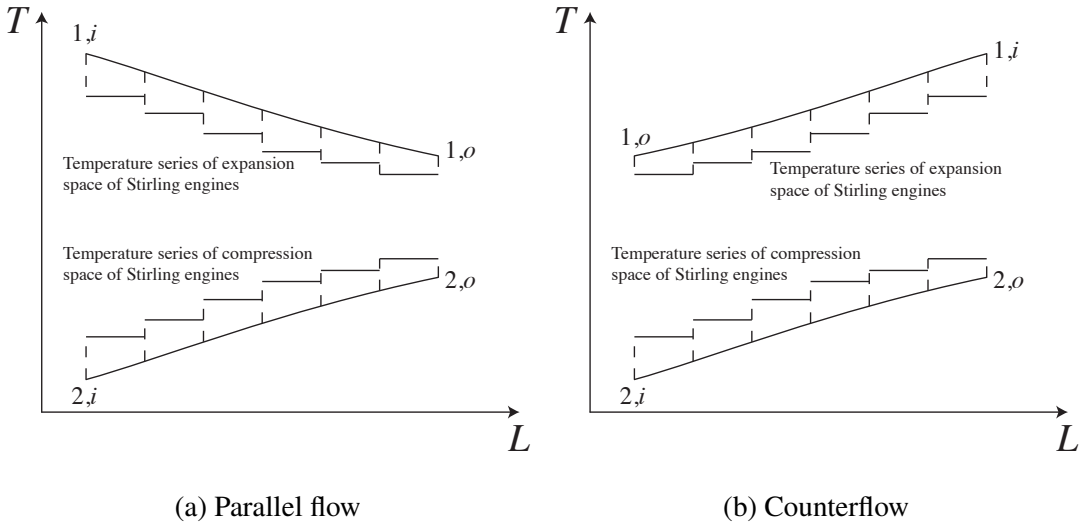


Figure 3-10 Heat transfer diagrams of parallel flow and counterflow

In Figure 3-9,  $T_{1,i,1} = T_{1,i}$ ,  $\dot{m}_{1,r} = \dot{m}_1/n_2$ . For  $x$  from 1 to  $n_1 - 1$ , where  $x$  is the column number of Stirling engines,  $T_{1,i,x+1} = T_{1,o,x}$ ,  $T_{2,i,x+1} = T_{2,o,x}$ .

Assume that the positive flow direction is to the right, for parallel flow,  $T_{2,i,1} = T_{2,i}$ ,  $\dot{m}_{2,r} = \dot{m}_2/n_2$ ; for counterflow,  $T_{2,o,n_1} = T_{2,i}$ ,  $\dot{m}_{2,r} = -\dot{m}_2/n_2$ .

Assume linear temperature profile across the regenerator, the mean effective temperature  $T_{R,x} = \frac{T_{H,x} - T_{L,x}}{\ln(T_{H,x}/T_{L,x})}$ <sup>[122,123]</sup> and the symmetrical regenerator behaviour assumption  $e_x = \frac{T_{R,x} - T_{L,x}}{T_{H,x} - T_{L,x}}$ <sup>[114,115]</sup>

For a Stirling engine in column  $x$ ,  $x$  from 1 to  $n_1$ , according to Equation (3.38) and Equation (3.39),

$$T_{hw,x} = T_{1,i,x} - \frac{T_{1,i,x} - T_{1,o,x}}{1 - \exp(-\frac{U_{se,1}A_{se,1}}{\dot{m}_{1,r}c_{p,1,x}})} \quad (3.76)$$

$$T_{cw,x} = T_{2,i,x} - \frac{T_{2,i,x} - T_{2,o,x}}{1 - \exp(-\frac{U_{se,2}A_{se,2}}{\dot{m}_{2,r}c_{p,2,x}})} \quad (3.77)$$

The power of each Stirling engine in column  $x$  can be written as

$$P_{se,x} = W_{th,x} - W_{pd,x} - W_{fs,x} \quad (3.78)$$

The efficiency of each Stirling engine in column  $x$  can be written as

$$\eta_{se,x} = \frac{W_{th,x} - W_{pd,x} - W_{fs,x}}{Q_{th,x} + Q_{id,x} + Q_{sc,x}} \quad (3.79)$$

For energy balance,

$$\dot{m}_{1,r}(h_{1,i,x} - h_{1,o,x})(1 - \eta_{se,x}) = \dot{m}_{2,r}(h_{2,o,x} - h_{2,i,x}) \quad (3.80)$$

Using equations in Section 3.1.3 and the energy balance equations, key parameters of the Stirling engine array can be obtained.

The efficiency of the Stirling engine array

$$\eta_{sea} = 1 - \frac{\dot{m}_2(h_{2,o,n_1} - h_{2,i,1})}{\dot{m}_1(h_{1,i,1} - h_{1,o,n_1})} \quad (3.81)$$

The output power of each Stirling engine in column  $x$

$$P_{se,x} = \dot{m}_{1,r}(h_{1,i,x} - h_{1,o,x})\eta_{se,x} \quad (3.82)$$

The total output power of the Stirling engine array

$$P_{sea} = \eta_{sea}\dot{m}_1(h_{1,i,1} - h_{1,o,n_1}) \quad (3.83)$$

### 3.3 Steam generating system modeling

The steam generating system can be divided into preheater, evaporator and superheater, they are collectively referred to as PES. They are all heat exchangers. It is assumed that, in these heat exchangers, the pressure of the fluid does not change significantly. It can be assumed that the water pressure in the steam generating system equals to the pressure of the inlet pressure of the turbine. Besides, these heat exchangers do not exchange heat with the environment. To clearly understand the modeling process of these heat exchangers, an example of steam generating system as shown in Figure 3-11 is used for explanation. Figure 3-12 shows the  $T-Q$  diagram of the heat transfer process. State points of different fluids are marked on the sketch. The number indicates the type of the fluid, the letter indicates the

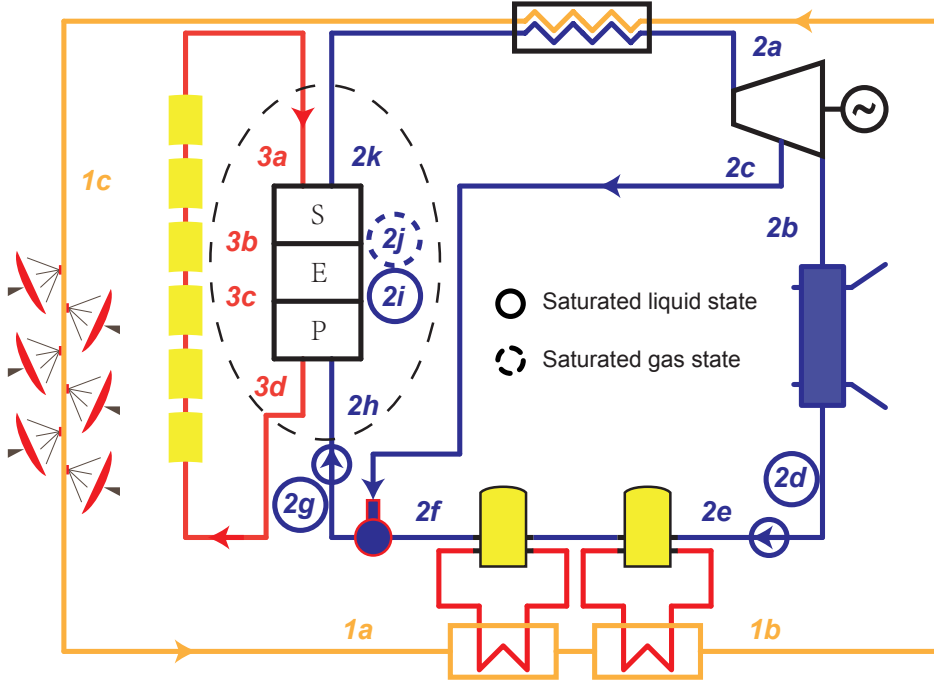


Figure 3-11 An example of steam generating system in a cascade system

state point of the fluid. A state point with solid circle indicates saturated liquid state ( $x = 0$ ), and with dotted circle indicates saturated gas state ( $x = 1$ ).

The modeling process of PES is the process of solving the unknown states of the state points. Notice that, the pressure of the fluids keeps constant in the heat transfer process. For an unsaturated state, known the temperature or enthalpy, the state is determined. This means, the temperature can be obtained from the enthalpy, and vice versa. For a saturated state, known the dryness ( $x$ ) of the fluid, the state is determined.

For a typical PES modeling process as shown in Figure 3-11,  $\dot{m}_2$ , state  $2h$  and state  $2k$  are determined by the parameters of the turbine. State  $3a$  is determined by the design parameters. State  $2i$  and state  $2j$  are determined by their dryness values.

### (1) Preheater

The outlet of the heated fluid is saturated liquid ( $x = 0$ ), so the outlet temperature  $T_{2i}$  and outlet enthalpy  $h_{2i}$  of the heated fluid are determined by the main pressure of the

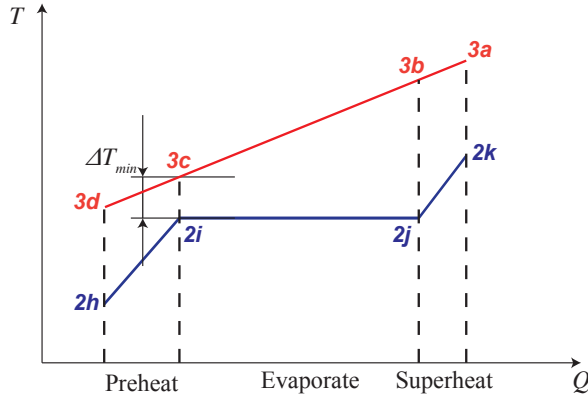


Figure 3-12 The steam generating process

turbine,  $p_s$ .

$$\dot{m}_3(h_{3c} - h_{3d}) = \dot{m}_2(h_{2i} - h_{2h}) \quad (3.84)$$

### (2) Evaporator

The outlet of the heated fluid is saturated gas ( $x = 1$ ), so the outlet temperature  $T_{2j}$  and outlet enthalpy  $h_{2j}$  of the heated fluid are determined by the main pressure of the turbine,  $p_s$ .

$$\dot{m}_3(h_{3b} - h_{3c}) = \dot{m}_2(h_{2j} - h_{2i}) \quad (3.85)$$

It has to be mentioned that, state  $3c$  is determined by  $T_{3c}$ , which equals to  $T_{2i} + \Delta T_{min}$ . ( $T_{3c} = T_{2i} + \Delta T_{min}$ )

### (3) Superheater

For the energy balance,

$$\dot{m}_3(h_{3a} - h_{3b}) = \dot{m}_2(h_{2k} - h_{2j}) \quad (3.86)$$

By solving the equations (3.84) to (3.86),  $\dot{m}_3$ , state  $3b$  and  $3d$  can be obtained.

## 3.4 System modeling

Different components are connected to form a system by their interfaces (inlets and outlets). These interfaces are interacted with each other by "streams". For example, the steam turbine in Figure 3-11 is connected with the deaerator by a steam stream. This steam stream has its own properties such as fluid type, mass flow rate, temperature, pressure and

so on. "Streams" are defined as objects in the modeling language – MATLAB. Appendix C shows the source code of the definition of the class – **Stream**.

Some properties, **T**, **q\_m** and **p**, of **Stream** are also objects. They belong to the classes **Temperature**, **Massflow** and **Pressure** separately.

Given the inherent properties of a **Stream**, its dependent properties, mass specific enthalpy (**h**), mass specific entropy (**s**) and pressure (**p**), can be obtained.

If the stream is a single phase stream, its dryness does not exist. Its dependent properties ( $h$ ,  $s$ ,  $c_p$ ) can be obtained from its temperature ( $T$ ) and pressure ( $p$ ) by calling the open source MATALB wrapper CoolProp. If the stream is a two-phase stream,  $0 \leq x \leq 1$ . Its dependent properties ( $h$ ,  $s$ ,  $c_p$ ) can be obtained from its pressure ( $p$ ) and dryness ( $x$ ). The reason of choosing pressure ( $p$ ) instead of temperature ( $T$ ) as the input value is that it is easier to be determined.

A **stream** can be used to record a state point since it contains all the information for a state point. Streams are defined in a system for component connection and system calculation. Different components are connected by streams to form a system. The Streams are passed as parameters to the components, completing the calculation of the methods in the components.

Components are connected each other by streams. Their inlets and outlets are used as interfaces for connection. Two interfaces are connected together by being assigned the same stream.

Systems are initialized by given parameters (design parameters). These parameters are assigned to corresponding properties of the streams and thus affect the state of the related components.

For system calculation, it has to be mentioned that, some parameters of a component are related with other components. In such situations, guess values are used for the calculation methods in the components. The guess values are set to be the properties of some streams. Each of these streams is assigned to two components (evaporator and superheater). These streams are assigned to corresponding components to accomplish the calculation methods in the components. These calculation methods will return solutions for the stream parameters. Then the parameters will be compared with the guess values for verification. If the differences between guess values and the calculated parameters are within permissible error, the guess values are accepted; otherwise, the guess values will be iteratively readjusted according to the Runge-Kutta method until accepted.

For example, the mass flow rate of oil of the evaporator ( $\dot{m}_3$ ) is related with the superheater in a system as described in Figure 2-18a. A guess value of  $\dot{m}_3$ ,  $\dot{m}_{3,g}$ , is required to determine it.  $\dot{m}_{3,g}$  is assigned to the evaporator oil stream. This stream is assigned to both evaporator and superheater. In **evaporator**, the method **get\_T\_3b** will change the temperature of the stream ( $T_{3b}$ ) from the default value. In **superheater**, the method **get\_q\_m\_3** will return a solution of  $\dot{m}_3$ ,  $\dot{m}_{3,s}$ , for verification. If  $|\dot{m}_{3,g} - \dot{m}_{3,s}|$  is less than permissible error ( $10^{-4}$ ), then  $\dot{m}_{3,g}$  is accepted as the value of  $\dot{m}_3$ ; otherwise,  $\dot{m}_{3,g}$  will be iteratively readjusted according to the Runge-Kutta method until  $|\dot{m}_{3,g} - \dot{m}_{3,s}| < 10^{-4}$ .

### 3.5 Conclusion

This chapter presents the modeling method of the cascade system and introduces the modeling of some key components and subsystems in detail. The component models are developed in MATLAB using object-oriented method. Bottom-up design method is applied for system development. Models of the components of a system are developed first according to their mechanism characteristics, and the system model is established by these component models. A MATLAB class **Stream** created for component connection is used as an example to introduce the system modeling process. The components' inlets and outlets are used as interfaces for connection. Two interfaces are connected together by being assigned the same stream. The calculation process related with different components is also briefly introduced in this chapter.

Due to the encapsulation, composition and polymorphism of the object-oriented language, the system model has some advantages such as easy to establish, convenient to replace a component and clearly check the performance of specific components.

The key component models in the cascade system can be validated experimentally or be compared with the classic models. The validation of Stirling engine model shows that the proposed model has much better agreement with the experimental results than previous classic thermal models at various rotation speeds and mean effective pressures.

## Chapter 4 Optimization of Stirling engine array

### 4.1 Connection types of SEA

For a single Stirling engine, the heat transfer processes between fluids and engine are independent and irrelevant with the directions of the flows, which means the efficiency and power are not affected by the direction of fluids. However, for an SEA, the connection type will affect the temperature profiles through the array and the specific work production, both of which will determine the efficiency and power of the SEA. It is practically significant to investigate the influence of connection type of an SEA on its performance. Using parallel flow, on the one hand, will reduce the flow rate of the fluid, which will reduce the power of each engine; however, on the other hand, will take the advantage of higher inlet heating fluid temperature (or lower inlet cooling fluid temperature), which may increase the power of each engine. Using serial flow, on the one hand, will increase the flow rate of the fluid, which will increase the power of each engine; however, on the other hand, the inlet heating fluid temperature reduces with the flow direction (or the inlet cooling fluid temperature increases with the flow direction), which leads to lower engine power along the flow direction. Using the same order will lead to largest fluid temperature difference (temperature difference of the heating and cooling fluids) at the first engines and smallest fluid temperature difference at the last engines. Using the reverse order will lead to more averaged fluid temperature differences of each engine. For a heat exchanger, the reverse order (counterflow), which leads to a smaller fluid temperature difference, has a better heat transfer effect for its lower exergy loss. However, for a Stirling engine, the smaller fluid temperature difference leads to lower performance due to the lower temperature difference of the working gas in the hot space and cold space. To find out the influence of connection types on the performance of SEA, it is essential to classify the connection types.

Five basic connection types of SEA are summarized according to the direction-irrelevant feature of Stirling engine, as shown in Figure 4-1. Type 1 is parallel flow, Type 2 is serial flows in the same order, Type 3 is serial flows in the reverse order, Type 4 is heating fluid in serial flow and cooling fluid in parallel flow and Type 5 is heating fluid in parallel flow and cooling fluid in serial flow. All other connection types are the combination of these five

basic connection types. For instance, an SEA in Figure 4-2 is the combination of Type 2 and Type 4.

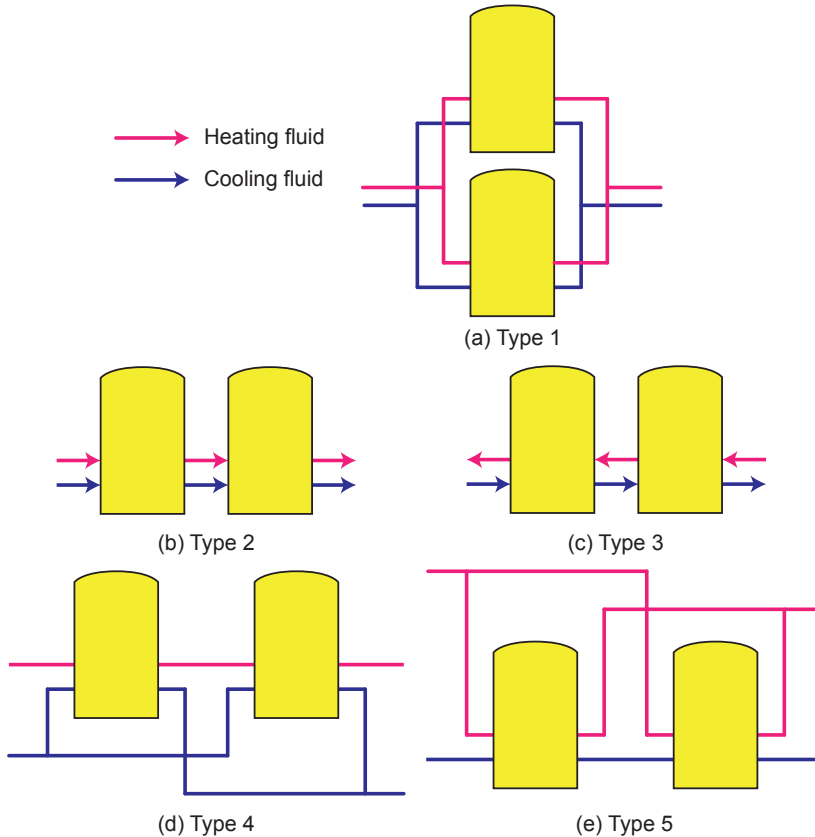


Figure 4-1 Five basic connection types of SEA

## 4.2 Modeling of the SEAs

As mentioned in Section 4.1, there are five basic connection types for an SEA. All other connection types are the combination of these five basic connection types. This thesis investigates the five basic connection types.

To determine the performance of an SEA, models of all the Stirling engines need to be built depending on their thermodynamic characteristic. Stirling engines are chosen to have

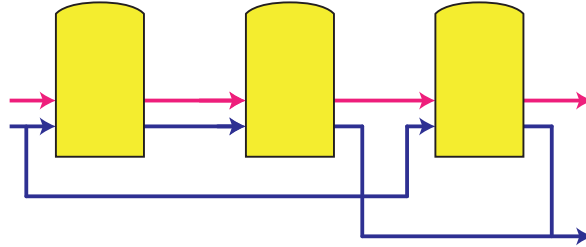


Figure 4-2 An instance of connection type of an SEA

the same parameters including the same speed  $s_{se}$ . This is a reasonable assumption when using SEA for power generation, where the output power frequency should be constant. The speed of Stirling engine can be calibrated by speed controller system<sup>[124]</sup>. To eliminate interference of other factors, heating and cooling fluids are chosen to have same parameters for different connection types of SEAs. To clearly find out the performance differences of different SEAs, large temperature differences of the heating/cooling fluids after heat exchange with the engines are preferred. Air is chosen as the cooling fluid instead of commonly used water to avoid small temperature rise and evaporation in the cooling process. Design parameters of Stirling engines are the same as shown in Table 3.2. Other parameters of Stirling engines and heating/cooling fluids in SEAs are shown in Table 4.1. Rotation speed of the engines and mean effective pressure are chosen to be 25 Hz and 5 MPa respectively to get the best Stirling engine model for performance prediction, as pointed in Section 3.1.3.3.

In an SEA, there are 2 flows as shown in Figure 4-1. In a serial flow, each engine's mass flow rate is  $\dot{m}$ , and from the flow's direction, for  $2 \leq x \leq n_{se}$ ,

$$T_{i,x} = T_{o,x-1} \quad (4.1)$$

In a parallel flow, each engine's mass flow is  $\dot{m}/n_{se}$ , for  $2 \leq x \leq n_{se}$ ,

$$T_{i,x} = T_{i,h} \quad (4.2)$$

According to the equations (Equation (3.57)-(4.2)), there are  $6n_{se} - 2$  equations for  $6n_{se}$  parameters for  $n_{se}$  engines. Other parameters of an SEA can be calculated by the given inlet temperature of the heating and cooling fluids. The efficiency and power of each engine can be obtained from Equation (3.53) and (3.52). The total efficiency and power of SEA can be obtained from powers of engines and outlet properties of the fluids.

Table 4.1 Parameters of SEA models

| Parameter     | Value   | Parameter   | Value              |
|---------------|---------|-------------|--------------------|
| Heating fluid | Air     | $\dot{m}_h$ | 0.4 kg/s           |
| Cooling fluid | Air     | $T_{i,h}$   | 1000 K             |
| $n_{se}$      | 6       | $p_{i,h}$   | $5 \times 10^5$ Pa |
| $s_{se}$      | 25 Hz   | $\dot{m}_c$ | 0.4 kg/s           |
| $p_{se}$      | 5 MPa   | $T_{i,c}$   | 300 K              |
| $U_h A_h$     | 180 W/K | $p_{i,c}$   | $5 \times 10^5$ Pa |
| $U_c A_c$     | 180 W/K |             |                    |

MATLAB is used as the programming tool to build the models of SEAs, and CoolProp is used to provide fluid properties for MATLAB program. Five basic SEA models composed of the aforementioned Stirling engines and fluids are built. To compare SEA connection types under various conditions, several parameters are investigated to find out their effects on SEA performance.

Figure 4-3 shows the solution algorithm of the SEA model. Flowchart (a) shows the algorithm to solve a Stirling engine known inlet parameters of the fluids. Flowchart (b) shows the algorithm to solve a Stirling engine known inlet parameters of heating fluid and outlet parameters of cooling fluid. Flowchart (c) shows the algorithm to solve the SEA model iteratively depending on different connection types. The levenberg-marquardt algorithm is applied to numerically solve the non-linear equations in the flowcharts.

### 4.3 Result analysis

SEA models with specified parameters in Table 4.1 are built and calculated. Results of the performances of the SEAs are shown in Table 4.2, it can be found that under specified parameters Type 3 has the highest efficiency and output power, while Type 1 has the lowest efficiency and output power.

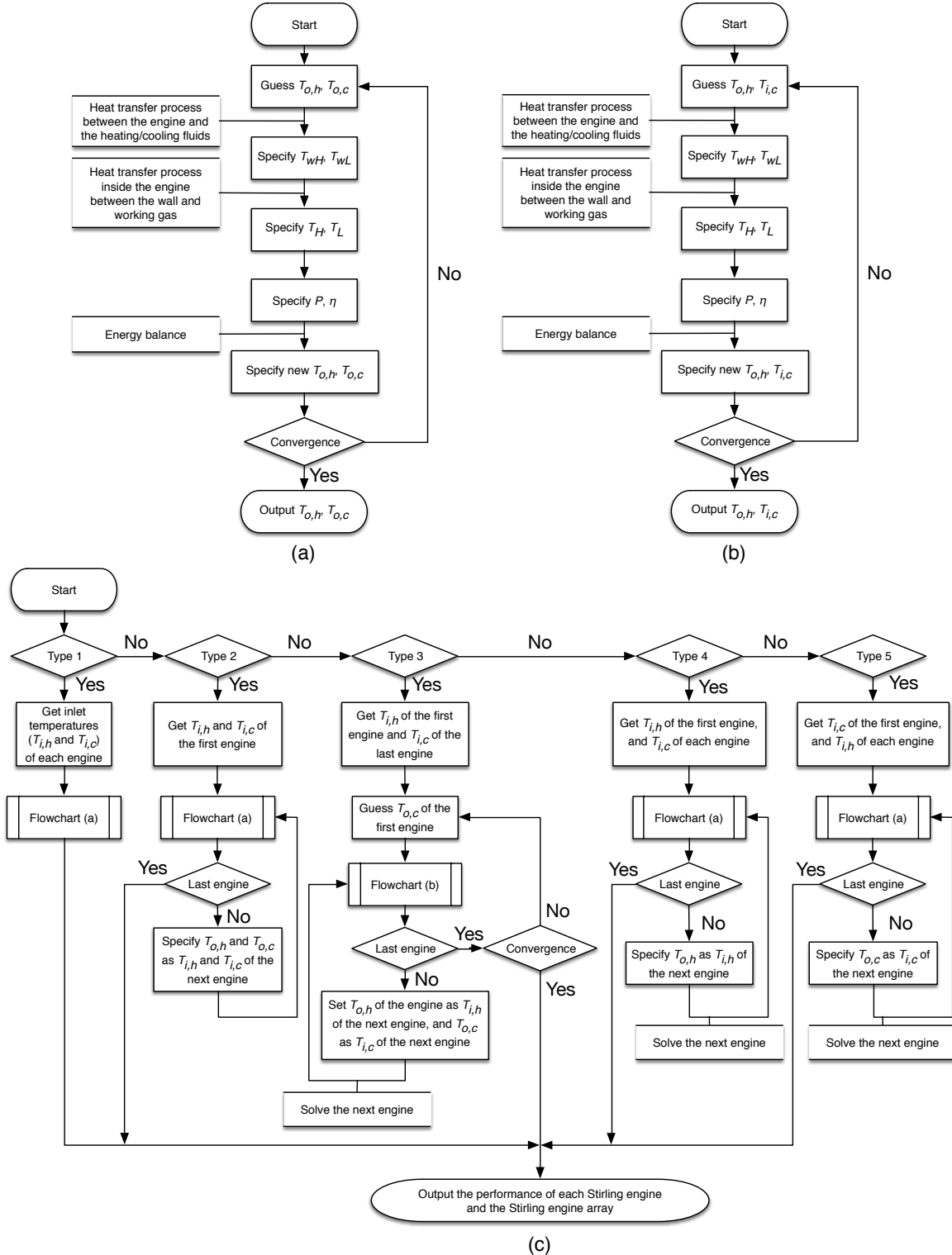


Figure 4-3 Flowcharts of the SEA model for performance analysis of the SEAs

Table 4.2 Results of SEA models under specified parameters

| Parameter | Value  | Parameter | Value  |
|-----------|--------|-----------|--------|
| $\eta_1$  | 0.2215 | $P_1$     | 8022 W |
| $\eta_2$  | 0.2273 | $P_2$     | 8483 W |
| $\eta_3$  | 0.2277 | $P_3$     | 8512 W |
| $\eta_4$  | 0.2227 | $P_4$     | 8116 W |
| $\eta_5$  | 0.2263 | $P_5$     | 8399 W |

### 4.3.1 Effects of $T_{i,h}$

According to Carnot cycle efficiency formula, the temperature of heating fluid determines the efficiency of Stirling engine array. For a Stirling engine, lower temperature heating fluid leads to a lower efficiency. The efficiency and output power may drop to 0 due to its insufficient heating fluid temperature to drive the engine.

Curves of performance of SEAs and  $T_{i,h}$  are shown in Figure 4-4. As it is shown, with the increase of  $T_{i,h}$ , both  $\eta$  and  $P$  increase for all SEAs. For some types of SEA, when  $T_{i,h}$  is lower than a critical temperature, some of the engines in the SEA will not work. In such situations, reduce the number of operating engines is a way to increase the total output power of the SEA. This strategy is used in the situation in Figure 4-4 when  $T_{i,h}$  is low. Turning points on the  $\eta-T_{i,h}$ ,  $P-T_{i,h}$  curves shows the use of this strategy. The data points in the figure record the performance of the SEA with maximum output power under given conditions. For example, in SEA of Type 1, when  $T_{i,h}$  is 820 K, if no engines is removed from the SEA, all the engines will stop due to the low inlet fluid temperature. Remove one engine out of the system will reduce the operating number of the engines from 6 to 5, and it will increase the inlet flow rate for each engine. This will make the remaining 5 engines work again and achieve the maximum output power under the condition of  $T_{i,h} = 820$  K. 820 K is a critical temperature for Type 1, and a turning point at 820 K can be found on the  $\eta-T_{i,h}$ ,  $P-T_{i,h}$  curves of Type 1 in Figure 4-4.

From the curves in Figure 4-4, it can be concluded that Type 2 and Type 3 have the best performance, and Type 2 has the best adaptability for lower  $T_{i,h}$ . All engines in Type 2 work

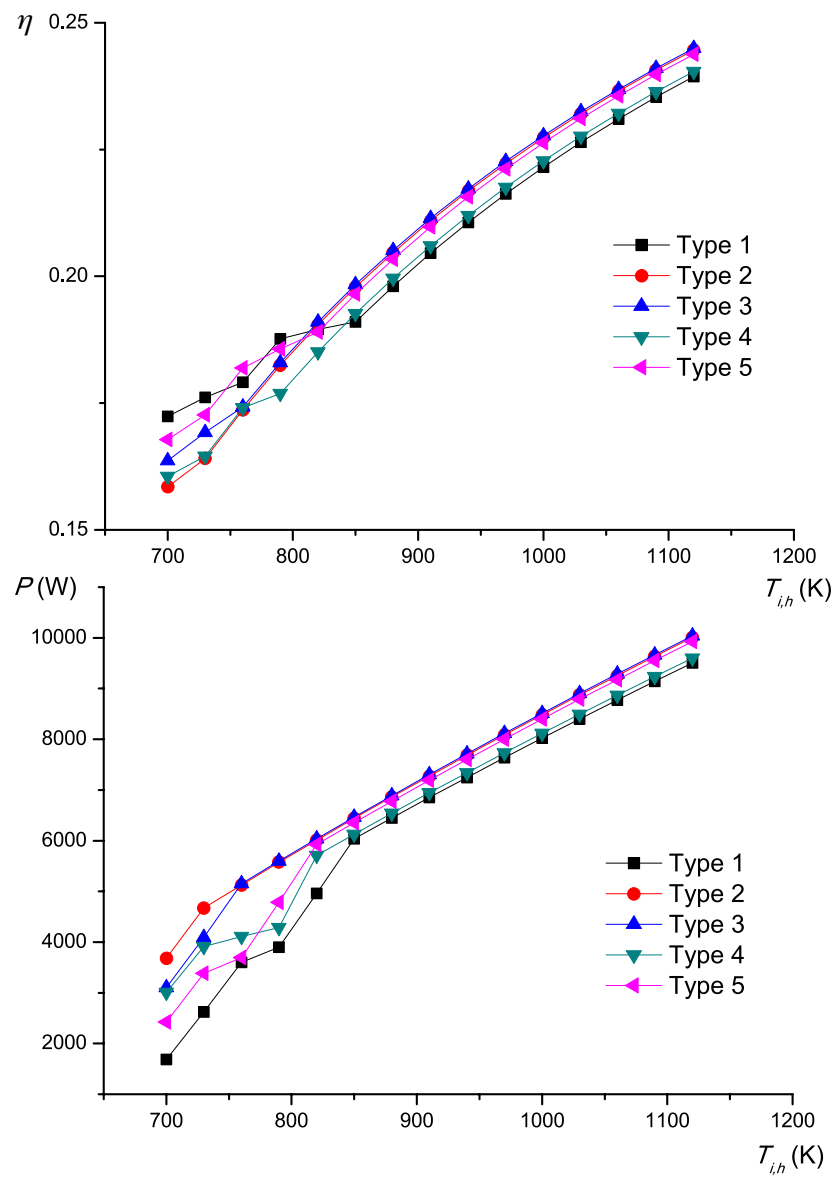


Figure 4-4 Influence of  $T_{i,h}$  on efficiency and power of SEA

from 730 K.

#### 4.3.2 Effects of $\dot{m}c_p$

According to Equation (3.59), (3.60),  $\dot{m}c_p$  (both  $\dot{m}_h c_{p,h}$  and  $\dot{m}_c c_{p,c}$ ) will affect the heat transfer process, which is one of the vital factor for the performance of SEA.

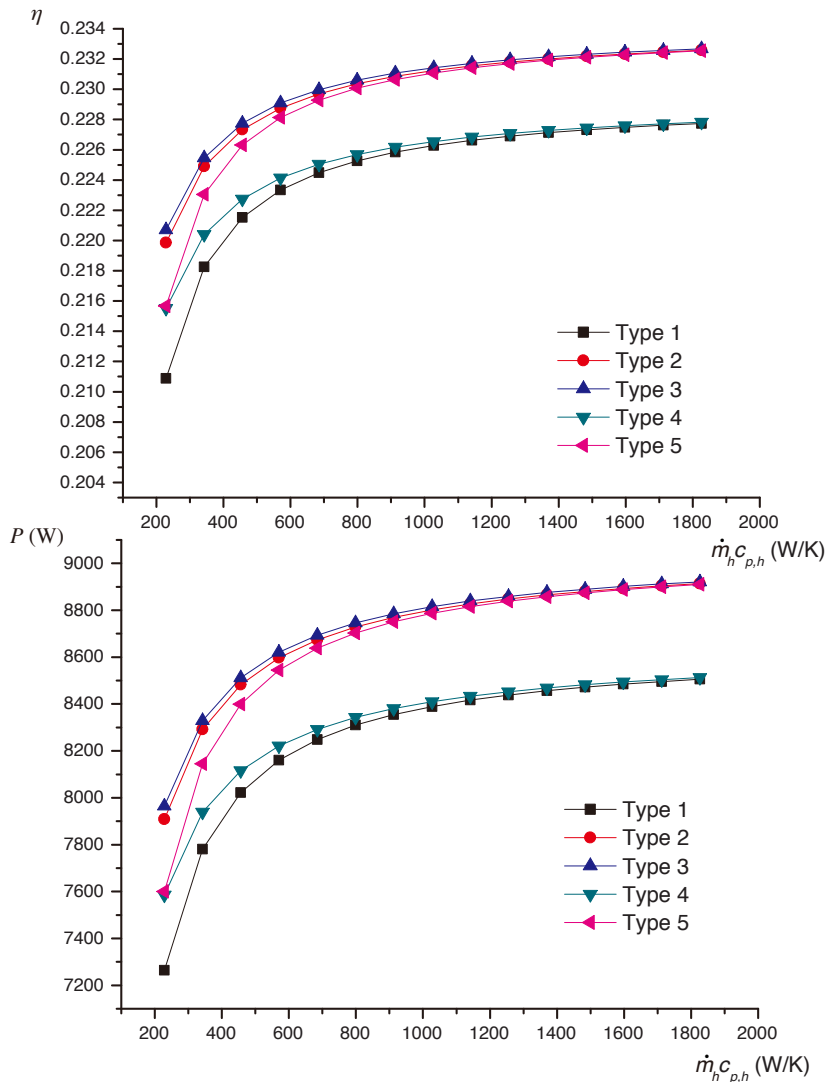


Figure 4-5 Influence of  $\dot{m}_h c_{p,h}$  on efficiency and power of SEA

Curves of performance of SEAs of different  $\dot{m}_h c_{p,h}$  are shown in Figure 4-5. For a large

$\dot{m}_h c_{p,h} (> 800 \text{ W/K})$ , Type 2 , Type 3 and Type 5 have similar performance, which can be interpreted as the cooling fluid has the same properties for the two types of SEAs, and for a large  $\dot{m}_h c_{p,h}$ , the heating fluid has similar effect after diverged. Similar performance of Type 1 and Type 4 can be also interpreted for the same reason.

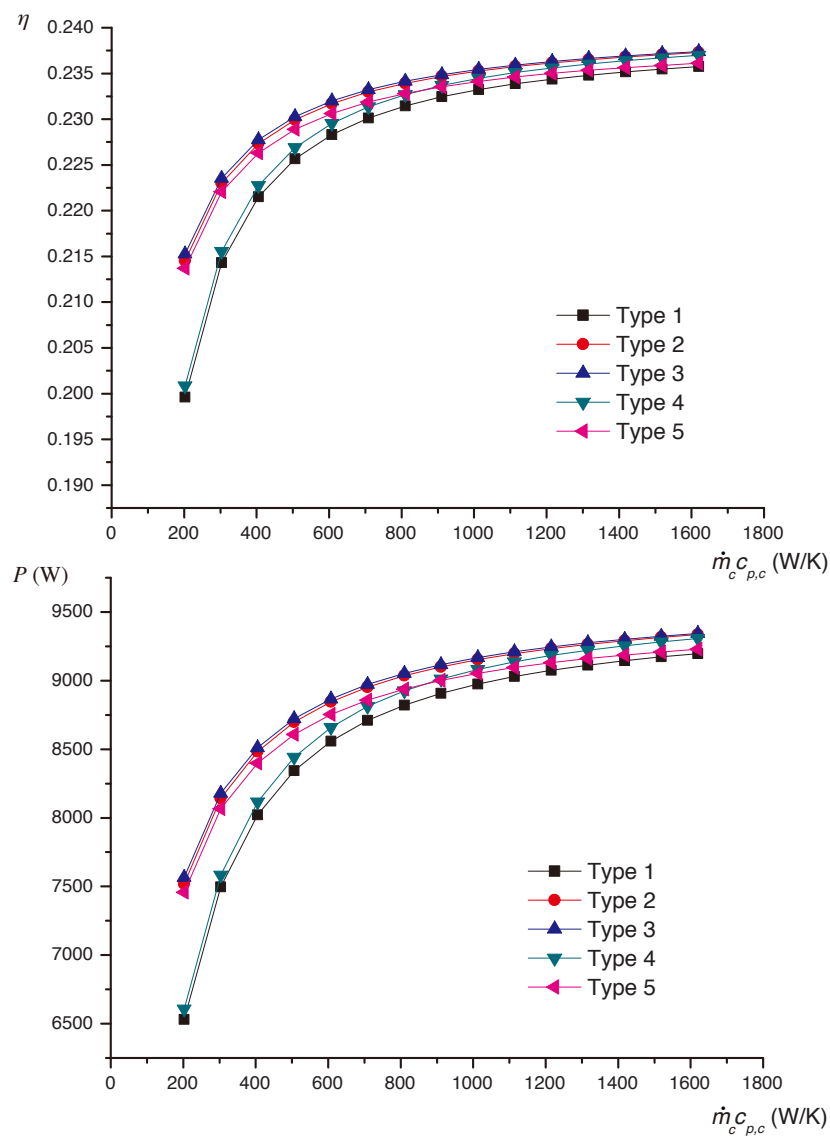


Figure 4-6 Influence of  $\dot{m}_c c_{p,c}$  on efficiency and power of SEA

Curves of performance of SEAs of different  $\dot{m}_c c_{p,c}$  are shown in Figure 4-6. For a

connection type of SEA, the performance improves with the increase of  $\dot{m}_c c_{p,c}$ . For a large  $\dot{m}_c c_{p,c}$  ( $> 800 \text{ W/K}$ ), Type 2 and Type 3 have similar performance, which means the flow order doesn't affect the performance of SEA with a large  $\dot{m}_c c_{p,c}$ . There exists an intersection point (at  $830 \text{ W/K}$ ) of curves of Type 4 and Type 5. For a larger  $\dot{m}_c c_{p,c}$ , Type 4 has a better performance, and vice versa. This can be interpreted that larger  $\dot{m}_c c_{p,c}$  weaken the drawback of larger temperature rise of parallel flow, while for the heating fluid, temperature drop of serial flow is smaller than parallel flow.

#### 4.3.3 Effects of $n_{se}$

By varying the number of engines in SEA, the performance levels changed accordingly.  $n_{se}$  may affect both the flow rates and temperatures of fluids of each engine. Figure 4-7 shows curves of performance of SEAs with different  $n_{se}$ . As it is shown, with an increase of  $n_{se}$  leads to a reduction of  $\eta$  for all SEAs due to smaller heating and cooling average temperature difference for more engines. For some types of SEA, when  $n_{se}$  is larger than a critical value, some of the engines in the SEA will not work and the curves will dive. E.g. for SEA of Type 1, when  $n_{se}$  is larger than 9, all the engines stop working, turning points at 9 can be found on the  $\eta$ - $n_{se}$ ,  $P$ - $n_{se}$  curves in Figure 4-7.

For a certain connection type, increase  $n_{se}$  will reduce the efficiency of SEA. For some connection types, increase  $n_{se}$  will reduce the output power  $P$  due to inoperative engines and smaller output power engines. It is important to choose the number of engines for some connection types of SEA.

For Type 1, when  $n_{se} \geq 10$ , all engines stop working for given heating and cooling fluids due to small  $\dot{m}c_p$ . For Type 2 and Type 3, every engine in the SEAs works.  $\eta$  reduces with increasing  $n_{se}$  due to smaller temperature difference of the fluids, and  $P$  increases due to more operating engines. For Type 4, by checking results, it can be found that when  $n_{se} = 13$ , the last engine doesn't work; when  $n_{se} = 14$ , only the first 10 engines will work; when  $n_{se} = 15$ , the working engine number drops to 9. For Type 5, by checking results, it can be found that when  $n_{se} = 12$ , the last 2 engines stop working; when  $n_{se} = 13$ , only the first 8 engines will work; when  $n_{se} = 14$ , the working engine number drops to 6; when  $n_{se} = 15$ , the working engine number drops to 4. The aforementioned strategy is applied to achieve maximum total output power. For Type 4, when  $n_{se} \geq 13$ , the number of the operating engines is changed

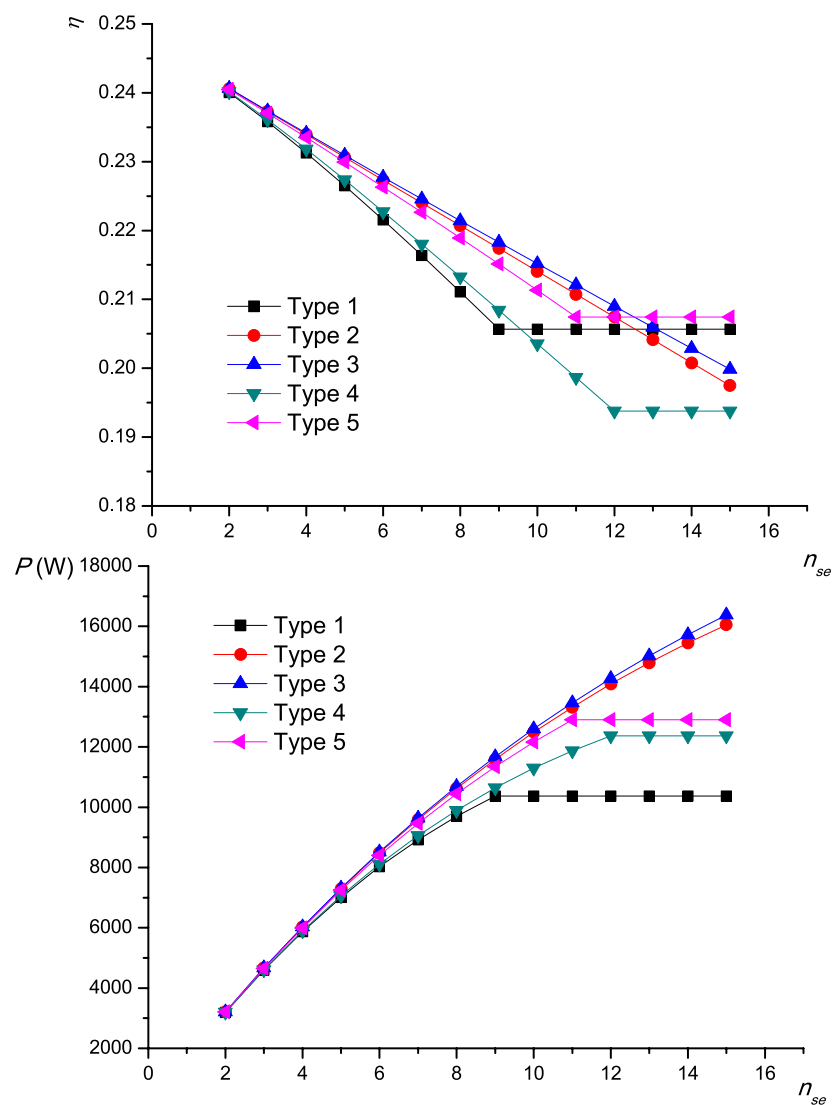


Figure 4-7 Influence of  $n_{se}$  on efficiency and power of SEA

to be 12 to achieve maximum output power. For Type 5, when  $n_{se} \geq 12$ , the number of the operating engines is changed to be 11 to achieve maximum output power. Horizontal lines in Figure 4-7 shows the application results of the strategy.

## 4.4 Conclusion

Connection type of the engines changes the flow rates and temperatures of the fluids, as a result the performance of the SEA will be different depending on the connection schemes. In order to compare performance of SEAs with different arrangements, five basic connection types of SEA are classified according to flow type and flow order.

Models of different connections of SEAs are developed to investigate the performance under different parameters and the impacts of  $T_{i,h}$ ,  $\dot{m}_h c_{p,h}$ ,  $\dot{m}_c c_{p,c}$  and  $n_{se}$  with different connection types. It is found that

- (1) Reduce  $T_{i,h}$  or  $\dot{m}c_p$  will weaken the performance of SEA of all connection types. This is obvious since lower  $T_{i,h}$  or  $\dot{m}c_p$  leads to lower temperature distribution of the hot chamber of the Stirling engines. Lower temperature difference of the hot chamber and cold chamber leads to lower efficiency.
- (2) When inlet temperature of hot fluid ( $T_{i,h}$ ) is lower than a critical value, some engines in the SEAs will stop working. Reduce the number of operating engines may help for the total output power.
- (3) Different connection types of SEAs show different adaptability for low  $T_{i,h}$ . Type 2 shows the best adaptability for low  $T_{i,h}$ . when  $T_{i,h} \geq 730$  K, all the 6 engines are running.
- (4) SEA of serial flows (Type 3) has the best performance and adaptability under different parameters. Given heating and cooling fluids, using serial flow is the best choice for the connection type of an SEA.

## Chapter 5 Optimization of steam generating system

### 5.1 Steam generating subsystem

In a solar parabolic trough power plant in which intermediate heat-transfer fluid (take oil for instance) is used, heat addition to the working fluid (take water for instance) takes place in three counterflow heat exchangers (steam generator subsystem, SGSS) as shown in Figure 5-1. The SGSS consists of preheater, evaporator and superheater. The flow rates of both oil and water remain the same in the three heat exchangers. The water has phase change in the three heat exchangers, from liquid to vapor in the evaporator, however, oil remains liquid. The heat capacity of water in each heat exchanger differs significantly. The heat capacity of oil has no significant difference since no phase change. The heat transfer process is illustrated on Figure 5-2. Large temperature differences exist at the inlets and outlets of the heat exchangers, which leads to large entropy production during the entire heat exchange process.

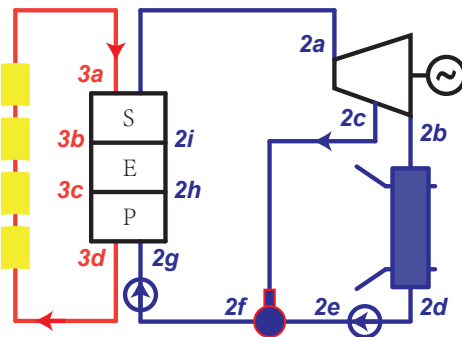


Figure 5-1 A typical solar parabolic trough system

The HTF at  $3a$  represents the solar field outlet temperature and at  $3d$ , the field inlet temperature. The difference between the two can be reduced by increasing the flow rate of HTF through the field.

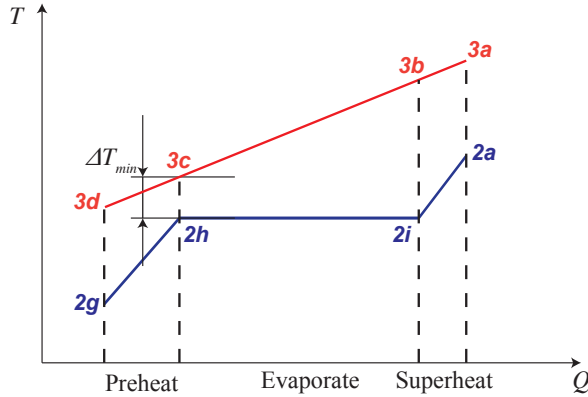


Figure 5-2 The steam generating process in counterflow heat exchangers

Since the heat exchangers must always stay a positive temperature difference for heat transfer, the temperature of oil must always be higher than the temperature of water. On the other hand, the temperature of oil should not be much higher than that of the water. Higher oil temperature leads to more heat losses in the solar field hence lower efficiency, more entropy production generated in the heat exchange process. Besides, higher oil temperature brings greater operational risks for the solar system. Setting the appropriate temperature difference between the oil and water is particularly important. The oil temperature must always higher (but not too much higher) than that of the water.

To find out the inlet and outlet temperatures of oil at the solar field, the lowest temperature difference of oil and water is defined as the pinch temperature  $\Delta T_{min}$ . The temperatures of state points  $2h$  and  $2i$  are determined by the main pressure of the steam turbine in Figure 5-1, and  $T_{3b}$  is larger than  $T_{3c}$ . So state points  $3c$  and  $2h$ , called the pinch points, are set to satisfy the pinch temperature,  $T_{3c} - T_{2h} = \Delta T_{min}$ . The pinch temperature  $\Delta T_{min}$  is usually set to be 10~20 K. It has to be mentioned that the temperature differences  $T_{3d} - T_{2g}$  and  $T_{3a} - T_{2j}$  worth attention to be not larger than  $\Delta T_{min}$ .

However, even with the chosen pinch temperature  $\Delta T_{min}$ , the temperature difference during the heat exchange process in SGSS is still large due to the phase change of water. Large temperature differences always exist at the inlet/outlet of the exchangers. As shown in Figure 5-3, it is a tradeoff to choose a mass flow rate of oil ( $\dot{m}_3$ ).  $\dot{m}_3$  affects the slope of curve  $3a-3b-3c-3d$ . A smaller  $\dot{m}_3$  leads to a steeper curve, hence a larger  $T_{3a} - T_{2j}$ . A larger  $\dot{m}_3$  leads to a more gentle curve, hence a larger  $T_{3d} - T_{2g}$ . The heat transfer processes in

SGSS always produce large entropy and exergy losses. In this regard, a new steam generating system to reduce exergy loss is put forward.

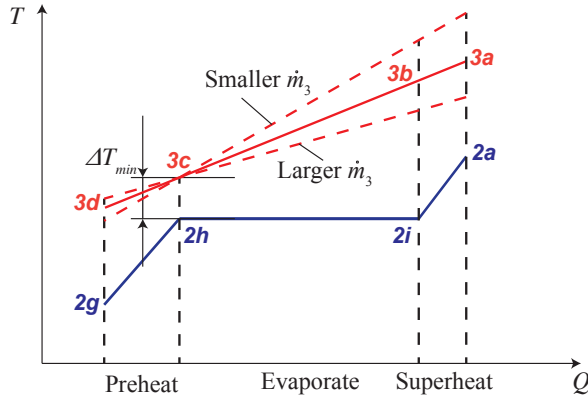


Figure 5-3 The tradeoff to choose  $\dot{m}_3$

## 5.2 Multistage exergy loss reduction system

The reason of large temperature differences of the two curves in Figure 5-2 is that, the slope of oil curve changes slightly in different heat exchangers (preheater, evaporator and superheater), while the water curve changes dramatically due to large heat capacity  $c_p$  differences.

$$\Delta Q = c_p \dot{m} \Delta T \quad (5.1)$$

The slope of the curves are determined by  $c_p \dot{m}$ ,  $\dot{m}$  can be altered to adjust the slope of the curves despite  $c_p$  is unalterable. All the water needs to be heated from supercooled water to superheated steam, which means  $\dot{m}_2$  remains the same in the three heat exchangers. The last way is to change  $\dot{m}_3$  in the heat exchangers.

As shown in Figure 5-4, the oil curve can be changed to the dashed curve. The temperature difference between the water curve and oil curve reduces significantly. Water is heated in three stages and the exergy loss reduces. The corresponding steam generating system is so called Multistage Exergy Loss Reduction System (MELRS). Figure 5-5 shows the schematic

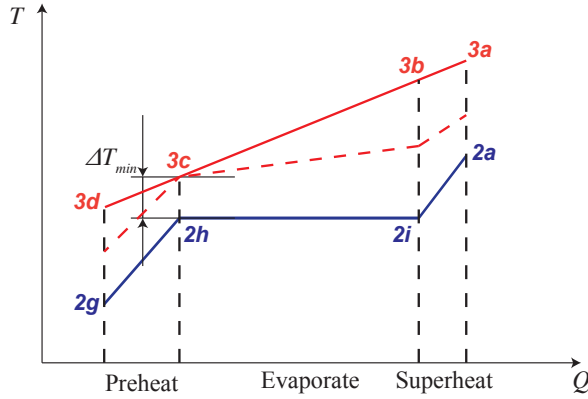


Figure 5-4 Change  $\dot{m}_3$  in the heat exchangers to reduce the temperature difference

diagram of the MELRS for comparison with typical solar parabolic trough system in Figure 5-1. The solar field in Figure 5-1 has been divided into three independent sectors. Each sector becomes the heat source of a range for the steam heating process: the first corresponds to overheating, the second to evaporation, and the third to preheating. It has to be mentioned that the collectors in the schematic diagram are only used for explanation. The arrangement of these collectors can be in series, in parallel or combination of both.

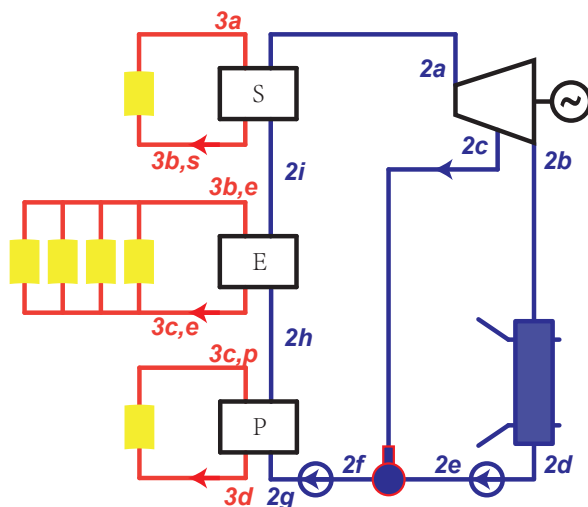


Figure 5-5 The schematic diagram of the MELRS

To optimize the MELRS, considering the limitation of pinch temperature, temperatures

of the oil at the inlet/outlet of the heat exchangers can be set according to following rules:

$$T_{3d} - T_{2g} = \Delta T_{min}$$

$$T_{3c,p} = T_{3c,e} = T_{3c}$$

$$T_{3c} - T_{2h} = \Delta T_{min}$$

$$T_{3b,e} = T_{3b,s} = T_{3b}$$

$$T_{3a} - T_{2a} = \Delta T_{min}$$

A large flow rate of oil in the evaporator  $\dot{m}_{3,e}$  can be applied to reduce the temperature  $T_{3b}$  hence the temperature differences of the oil and water. However, a large  $\dot{m}_{3,e}$  requires more pump power consumption for the oil circuits. Besides,  $\dot{m}_{3,e}$  is limited for the limitation of oil velocity in the pipes.

The enthalpy of each state point can be determined by its temperature and pressure.

The optimum oil average temperature in the solar field corresponds to the preheater is

$$T_{3,p} = (T_{2g} + T_{2h})/2 + \Delta T_{min} \quad (5.2)$$

The optimum oil flow rate in the solar field corresponds to the preheater is

$$\dot{m}_{3,p} = \dot{m}_2(h_{2h} - h_{2g})/(h_{3c} - h_{3d}) \quad (5.3)$$

The optimum oil average temperature in the solar field corresponds to the evaporator is

$$T_{3,e} = (T_{3b} + T_{3c})/2 \quad (5.4)$$

The optimum oil flow rate in the solar field corresponds to the evaporator is

$$\dot{m}_{3,e} = \dot{m}_2(h_{2i} - h_{2h})/(h_{3b} - h_{3c}) \quad (5.5)$$

The optimum oil average temperature in the solar field corresponds to the superheater is

$$T_{3,s} = (T_{3b} + T_{2a} + \Delta T_{min})/2 \quad (5.6)$$

The optimum oil flow rate in the solar field corresponds to the superheater is

$$\dot{m}_{3,s} = \dot{m}_2(h_{2a} - h_{2i})/(h_{3a} - h_{3b}) \quad (5.7)$$

### 5.3 Comparison

To find out the effect of MELRS, models of traditional SGSS and proposed MELRS are developed based on the models of the components created in Chapter 3. To clearly find out the influence of oil temperature on the performance of the trough collectors, Equation (3.7) in Section 3.1.1 is used.

The exergy loss caused by a heat exchange process per unit time

$$\dot{I} = T_{amb} \left( \sum \dot{m}_o s_o - \sum \dot{m}_i s_i \right) \quad (5.8)$$

Table 5.1 Main parameters used for SGSS and MELRS

| Parameter        | Value                | Parameter | Value                 |
|------------------|----------------------|-----------|-----------------------|
| $I_r$            | 700 W/m <sup>2</sup> | $T_s$     | 613.15 K              |
| $P_{ge}$         | $6 \times 10^6$ W    | $p_s$     | $2.35 \times 10^6$ Pa |
| $\eta_{i,tb}$    | 0.711                | $p_c$     | $1.5 \times 10^4$ Pa  |
| $\eta_{ge}$      | 0.975                | $p_{de}$  | $1 \times 10^6$ Pa    |
| $\Delta T_{min}$ | 15 K                 |           |                       |

The turbine and deaerator are the same for the two systems (SGSS and MELRS), so that the corresponding state points of water are the same. The main parameters are listed in Table 5.1.

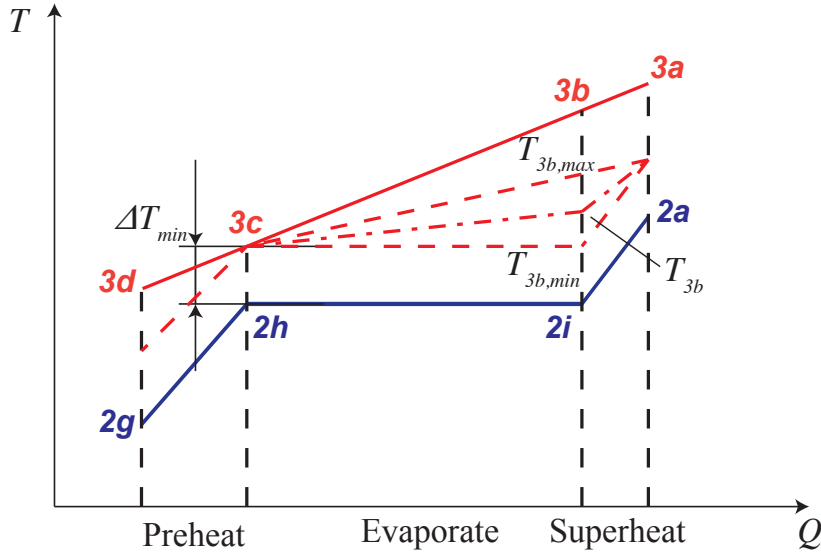
As discussed in Section 5.2,  $T_{3b}$  is an undetermined value. Figure 5-6 shows the minimum and maximum value of it.  $T_{3b,min}$  means the limit situation of unlimited flow rate of oil in the evaporator,  $T_{3b,min} = T_{3c}$ .  $T_{max}$  has the traditional effect of temperature differences in the evaporator and superheater,  $\dot{m}_{3,e} = \dot{m}_{3,s}$ . In our research,  $T_{3b}$  is set to be the average value of the two limitations,  $T_{3b} = (T_{3b,min} + T_{3b,max})/2$ .

$$\frac{T_{3b,max} - T_{3c}}{T_{3a} - T_{3c}} = \frac{T'_{3b} - T_{3c}}{T'_{3a} - T_{3c}} \quad (5.9)$$

where  $T'_{3a}$  and  $T'_{3b}$  are the inlet oil temperature of superheater and evaporator in SGSS respectively.

Table 5.2 Simulation results of SGSS and MELRS

| SGSS              | MELRS                |                      |                      |
|-------------------|----------------------|----------------------|----------------------|
|                   | $T_{3b,max}$         | $T_{3b}$             | $T_{3b,min}$         |
| $T_{2a}$          | 613.15 K             |                      |                      |
| $T_{2i}$          | 493.83 K             |                      |                      |
| $T_{2h}$          | 493.83 K             |                      |                      |
| $T_{2g}$          | 453.28 K             |                      |                      |
| $T_{3c}$          | 508.83 K             |                      |                      |
| $T_{3a}$          | 653.15 K             | 628.15 K             | 628.15 K             |
| $T_{3b}$          | 634.11 K             | 612.41 K             | 560.62 K             |
| $T_{3d}$          | 495.43 K             | 468.28 K             | 468.28 K             |
| $\dot{m}_{3p}$    | 47.8 kg/s            | 16.1 kg/s            | 16.1 kg/s            |
| $\dot{m}_{3e}$    | 47.8 kg/s            | 58.6 kg/s            | 120.8 kg/s           |
| $\dot{m}_{3s}$    | 47.8 kg/s            | 59.4 kg/s            | 14.3 kg/s            |
| $\dot{I}_p$       | $4.80 \times 10^4$ W | $2.58 \times 10^4$ W | $2.58 \times 10^4$ W |
| $\dot{I}_e$       | $1.10 \times 10^6$ W | $9.68 \times 10^5$ W | $6.24 \times 10^5$ W |
| $\dot{I}_s$       | $1.81 \times 10^5$ W | $1.42 \times 10^5$ W | $9.19 \times 10^4$ W |
| $\dot{I}_{total}$ | $1.33 \times 10^6$ W | $1.14 \times 10^6$ W | $7.44 \times 10^5$ W |
| $\eta_p$          | 0.699                | 0.703                | 0.703                |
| $\eta_e$          | 0.673                | 0.678                | 0.689                |
| $\eta_s$          | 0.633                | 0.648                | 0.662                |
| $\eta_{overall}$  | 0.670                | 0.676                | 0.686                |
|                   |                      |                      | 0.695                |


 Figure 5-6  $T_3b$  in the  $T$ - $Q$  diagram of the heat transfer processes

Simulation results of the two system models are listed in Table 5.2. It can be found that MELRS can effectively reduce the exergy loss of the steam generating process. The exergy loss can be reduced from 14.3% up to 76.7% for the three MELRS. The overall thermal efficiency of the solar fields can be improved from 0.9% up to 3.6%.

It is worthy pointing that, for the situation  $T_{3b} = T_{3b,min}$ , when  $\dot{m}_{3e} = \infty$ , the correlation (5.8) is not applicable. The new correlation listed below is applied for the isothermal heat transfer process

$$\dot{I} = T_{amb} \left( \frac{Q}{T_{2h}} - \frac{Q}{T_{3c}} \right) = \frac{QT_{amb}(T_{3c} - T_{2h})}{T_{2h}T_{3c}} \quad (5.10)$$

where,  $Q$  is the heat transferred in the evaporator.

$T_{2a}$ ,  $T_{2i}$ ,  $T_{2h}$ ,  $T_{2g}$  and  $T_{3c}$  are the same for SGSS and different MELRSs for the same water side processes. The different mass flow rates of the oil lead to different oil temperatures in the heat exchangers, and hence different exergy loss. It can be found that the exergy losses in preheaters of MELRSs (all are  $2.58 \times 10^4$  W) are smaller than that of SGSS ( $4.80 \times 10^4$  W). The exergy losses in evaporators of different MELRSs vary greatly, from  $9.68 \times 10^5$  W to  $2.41 \times 10^5$  W for oil flow rate from 58.6 kg/s to infinity. Exergy loss in the evaporator takes the largest portion of the steam generating process, which takes about 82.8%, 85.2%, 83.8% and 78.0% for SGSS and MELRSs separately. Increasing flow rate of the heating fluid in

the steam generating process can effectively reduce the exergy loss. The exergy losses in superheaters of MELRSs ( $1.42 \times 10^5$  W,  $9.19 \times 10^4$  W and  $4.24 \times 10^4$  W) are much smaller than that of SGSS ( $1.81 \times 10^5$  W) due to the large temperature differences in the traditional superheaters.

It can be found that the MELRS can effectively reduce exergy loss hence improve the system efficiency compared to traditional SGSS. The thermal efficiency for the corresponding solar field for the preheater ( $\eta_p$ ), evaporator ( $\eta_e$ ) and superheater ( $\eta_s$ ) of MELRSs are larger than that of SGSS (virtual solar fields). The overall thermal efficiency ( $\eta_{overall}$ ) of the solar field can be improved effectively.

## 5.4 Conclusion

In this chapter, a novel multistage exergy loss reduction system is proposed to reduce the large exergy loss in traditional solar parabolic trough power plants. Traditional solar field is divided into three solar fields to provide heat to the preheater, evaporator, and superheater, respectively. Different flow rates in the three solar fields provides the ability to reduce temperature difference of the heat exchange processes.

Smaller temperature difference leads to lower oil temperature and therefore higher solar field thermal efficiency. Besides, the different temperature ranges of different solar fields provide the convenience of the application of different types of collectors.

The analytical model of the steam generating system is developed. A flow control strategy of HTF depending on the analytical system model is derived. Energy and exergy efficiency of the MELRS is analyzed and compared with the SGSS of traditional solar parabolic trough power plant. Result shows that the MELRS can effectively decrease the exergy loss in the heating process, and the performance of the plant can be improved. The exergy loss can be reduced from 14.3% up to 76.7% for the three typical MELRSs. The overall thermal efficiency of the solar fields can be improved from 0.9% up to 3.6%.

## Chapter 6 Cascade system performance evaluation

### 6.1 System description

In Section 2.3, two typical cascade system topologies (see Figure 2-18) are selected for further investigation. It has to be pointed out that, in Chapter 5, multistage exergy loss reduction system (MELRS) is proposed and analyzed. It is obvious that MELRS has better energy and exergy performance than SGSS. However, the MELRS is not applied in this chapter for investigation. There are several reasons. First, in order to clearly find out the advantages of cascade collection and cascade utilization of the cascade systems, it is not applied in the cascade system in this chapter. Second, compared with traditional SGSS, MELRS only changes the solar field, which has no influence on the cascade utilization of the cascade system. It can be easily applied in the cascade system analyzed in this chapter in the future without influence of existing calculations. Third, the MELRS proposed in Chapter 5 needs further research in the future. Different types of solar collector technologies can be applied in different solar fields. For example, linear Fresnel reflectors or flat collectors can be applied for the preheating solar field to reduce costs; molten salt can be used as heat transfer fluid in the superheating solar field to increase the main steam temperature of the Rankine cycle.

Two typical cascade system topologies are selected in Chapter 2. Both systems take advantage of the different types of heat collectors and different thermal cycles to achieve cascade collection of energy and cascade utilization. However, this chapter focuses on the first model because it is more widely used and more suitable for large-scale applications. Figure 6-1 shows the scheme sketch of the cascade system. In this system, dish collectors are used to provide heat for Stirling engines and air-to-water heat exchanger. Trough collectors are used to provide heat for steam generating processes (preheating, evaporating and superheating) in the Rankine cycle. Hot air is produced by the dish collectors. High temperature (1073 K) air is used to provide heat to Stirling cycle to get higher conversion efficiency, then the air is used to provide heat for air-to-water heat exchanger to use the lower temperature energy in Rankine cycle effectively. Besides, feed water of Rankine cycle is used to cool the Stirling engines to recycle the heat wasted conventionally. The Stirling engines are connected in series for better performance.

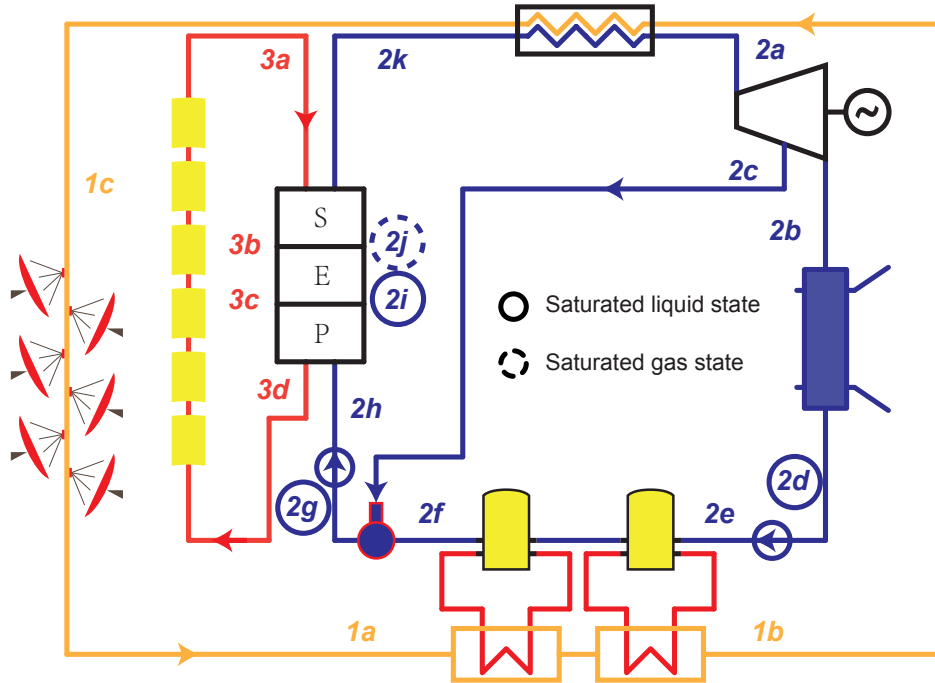


Figure 6-1 Sketch of the cascade system

Figure 6-2a shows the  $T-s$  diagram of the water circuit in the cascade system. In this Rankine cycle, the heat provided in process  $2e-2f$  comes from the Stirling engines, which increases the power of Rankine cycle. Figure 6-2b shows the heat transfer diagram of this process.

To build the cascade system model, several simplifying assumptions are made:

- Steady state at nominal load of the system is analysed.
- Pressure drop due to flow is negligible.
- The leak of working fluid in the pipes is neglected.
- Same isentropic efficiency of steam turbine with different loads and in different stages.
- Heat loss that occurs from the tube to the atmosphere is not considered.
- There is no heat loss to the environment for Stirling engines.
- Simple models are used of some processes and equipment.
- A symmetrical regenerator behavior is assumed so that a single effectiveness can be

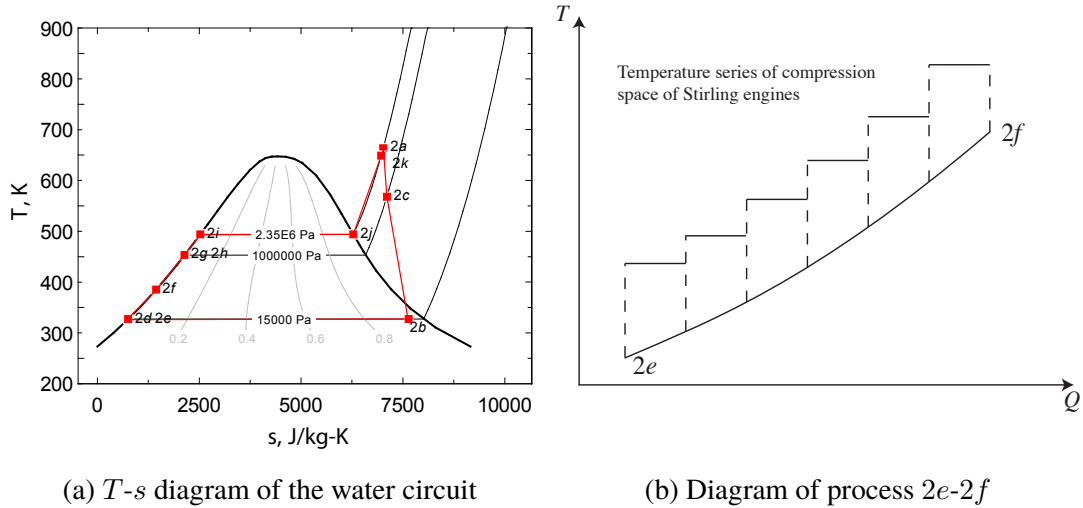


Figure 6-2 Diagrams of water circuit and 2e-2f process

defined as  $e = (T_R - T_L)/(T_H - T_L)$ .<sup>[114,115]</sup>

- A linear temperature profile across the regenerator exists, the mean effective temperature  $T_R = (T_H - T_L)/\ln(T_H/T_L)$ .<sup>[122,123]</sup>

## 6.2 System parameters

In order to study the efficiency of the system and its influencing factors, a model of the cascade system is required. Chapter 3 introduces the system modeling process in detail. After the system modeling process, another important task is to determine the system parameters.

The system mainly consists of the following components:

### 6.2.1 Environment

Typical environmental parameter values of Wuhan are used for the cascade system design.

$$I_r = 700 \text{ W/m}^2, T_{amb} = 293 \text{ K}, p_{amb} = 1 \times 10^5 \text{ Pa}, v_{amb} = 1 \text{ m/s.}$$

### 6.2.2 Steam Turbine

A steam turbine product, N-6 2.35, of Qingdao Jieneng Power Station Engineering Co., Ltd is used for calculation. Its nominal parameters are:  $P = 6 \text{ MW}$ ,  $p_s = 2.35 \text{ MPa}$ ,  $T_s = 390^\circ\text{C}$ ,  $\dot{m} = 32.09 \text{ t/h}$ ,  $p_c = 0.015 \text{ MPa}$ ,  $s_{tb} = 3000 \text{ rpm}$ .

Known the main steam parameters, its enthalpy and entropy can be obtained by using CoolProp,  $h_s = 3.2203 \times 10^6 \text{ J/kg}$ ,  $s_s = 7.0149 \times 10^3 \text{ J/(kg} \cdot \text{K)}$ .

$$\text{Exhaust enthalpy of the turbine } h_c = h_s - \frac{P}{\dot{m}} = 2.5472 \times 10^6 \text{ J/kg.}$$

Known exhaust pressure and  $s_{i,c} = s_s$ , isentropic exhaust enthalpy of the turbine can be obtained by using CoolProp,  $h_{i,c} = 2.2737 \times 10^6 \text{ J/kg}$ .

$$\text{So the isentropic efficiency of the turbine can be obtained from } \eta_{i,tb} = \frac{h_s - h_c}{h_s - h_{i,c}} = 0.71.$$

Taking into account of the application in solar trough system, the designed parameters of the steam turbine are shown in Table 6.2.

### 6.2.3 Trough collector

LUZ solar collector LS-3 is used as the trough collector for its known test data. Its main characters are listed in Table 6.1.<sup>[101]</sup>

Table 6.1 Main parameters of LS-3

| Parameter   | Value               | Parameter     | Value             | Parameter | Value            |
|-------------|---------------------|---------------|-------------------|-----------|------------------|
| $A_{pc}$    | $570.2 \text{ m}^2$ | $w_{dc}$      | $5.76 \text{ m}$  | $L_{dc}$  | $99 \text{ m}$   |
| $f$         | $1.71 \text{ m}$    | $d_i$         | $0.066 \text{ m}$ | $d_o$     | $0.07 \text{ m}$ |
| $d_{abs,i}$ | $0.113 \text{ m}$   | $d_{abs,o}$   | $0.115 \text{ m}$ | Rim angle | $80^\circ$       |
| $\epsilon$  | 0.15                | $\eta_{peak}$ | 0.77              | $\rho$    | 0.94             |
| $\tau$      | 0.95                | $\alpha$      | 0.96              | $Fe$      | 0.97             |

### 6.2.4 Dish collector

A dish reflector product of SES (Stirling Energy System) is used as the reflector, the receiver is self-designed. The key parameters of the dish collector are listed in Table 3.1.

### 6.2.5 Stirling engines

The Stirling engines used in the cascade system are the same with the one analyzed in Section 3.1.3. It is a GPU-3 type Stirling engine, Table 3.2 shows its parameters.

### 6.2.6 Preheater

Water is heated to saturated water in the preheater by the oil. For outlet stream of water,  $x = 0$ . Besides, considering the minimum temperature difference required between oil and water,  $T_{3c} - T_{2i} = \Delta T_{3,2,min}$ .  $\Delta T_{3,2,min}$  is set to be 15 K.

### 6.2.7 Evaporator

Water is heated from saturated liquid water to saturated steam in the evaporator. For outlet stream of water,  $x = 1$ .

### 6.2.8 Superheater

The inlet temperature of oil is limited by the oil properties. In the cascade system, Therminol VP-1 Synthetic oil is used as the heat transfer fluid. Its properties can be obtained from both EES and CoolProp. The inlet temperature of the oil of superheater is set as  $T_{3a} = 623$  K.

### 6.2.9 Deaerator

The deaerator has two inlet streams and one outlet stream. They have the same pressure,  $p_{se} = 1 \times 10^6$  Pa. The outlet stream of the deaerator is saturated water.

### 6.2.10 Air-water heat exchanger

The inlet temperature is set as  $T_{1b} = 673$  K.

### 6.2.11 Main design parameters summary

The main design parameters of the cascade system can be concluded in Table 6.2.

## 6.3 System evaluation method

There are two aspects to be evaluated for the cascade system. The first one is the performance. The cascade system uses different types of collectors and different thermodynamic cycles. They are closely linked together. It is unable to define part of the system's efficiency or to indicate the output power of one specific kinds of collector. A common approach is to

Table 6.2 Basic design parameters of the cascade system

| Parameter  | Value                | Parameter            | Value              | Parameter | Value                 |
|------------|----------------------|----------------------|--------------------|-----------|-----------------------|
| $I_r$      | 700 W/m <sup>2</sup> | $T_{dc,o}$           | 1073 K             | $n_{se}$  | 100                   |
| $T_{amb}$  | 293 K                | $p_{dc}$             | $5 \times 10^5$ Pa | $T_s$     | 613 K                 |
| $p_{amb}$  | $1 \times 10^5$ Pa   | $\Delta T_{3,2,min}$ | 15 K               | $p_s$     | $2.35 \times 10^6$ Pa |
| $v_{amb}$  | 1 m/s                | $T_{tc,o}$           | 623 K              | $p_c$     | $1.5 \times 10^4$ Pa  |
| $P_{ge}$   | $6 \times 10^6$ W    | $p_{tc}$             | $2 \times 10^6$ Pa | $T_{s,d}$ | 663 K                 |
| $T_{dc,i}$ | 623 K                | $T_{1b}$             | 673 K              | $p_{de}$  | $1 \times 10^6$ Pa    |

define the overall efficiency of the system. The overall solar-to-electric efficiency equals to the total output power divided by the total input solar energy.

The other one is to compare with existing solar thermal power technologies. This requires more consideration.

(1) Compare with parabolic trough.

When compared with parabolic trough system, a higher efficiency of the cascade system may be explained as the usage of solar dish collector. It is difficult to tell if the higher efficiency is due to the usage of cascade system or the usage of dish collector.

(2) Compare with parabolic dish.

When compared with parabolic dish system, a lower cost of the cascade system may be explained as the usage of solar trough collector. It is difficult to tell if the lower cost is due to the usage of cascade system or the usage of trough collector.

(3) Compare with stand-alone systems.

It is important to choose good stand-alone systems. An intuitive idea is to use both parabolic trough and parabolic dish for comparison. To compare two systems, contrast conditions needs to be set.

If the same output power was selected as the contrast condition, different amount of trough collectors and dish collectors will be used in the cascade system and stand-alone systems. It is complicated for cost comparison due to different prices of trough collectors and dish collectors.

A better way is to select the same collectors as the contrast condition. Since the output is electricity, it is much more convenient for both efficiency comparison and cost comparison.

## 6.4 Stand-alone system selection

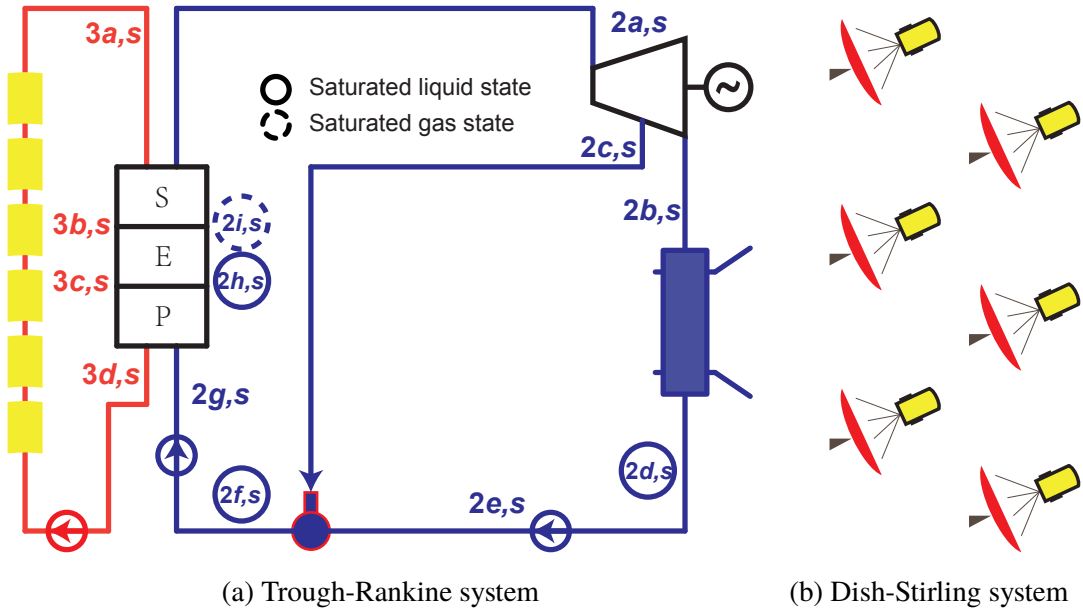


Figure 6-3 Sketch of the stand-alone systems

Figure 6-3 shows the sketch of the stand-alone systems. These two stand-alone systems are developed for comparison. They use the same dish collectors and trough collectors with the same thermal efficiencies of the cascade system.

### 6.4.1 Stand-alone trough-Rankine system

Steam turbine has the same main parameters and isentropic efficiency with that of the cascade system. Working pressure of deaerator is the same of the cascade system. So parameters of state  $2b, s$  and  $2c, s$  in Figure 6-3 of the steam turbine can be expressed by

$$\eta_{i,tb} = (h_{2a,s} - h_{2b,s}) / (h_{2a,s} - h_{i,2b,s}) = (h_{2a,s} - h_{2c,s}) / (h_{2a,s} - h_{i,2c,s}) \quad (6.1)$$

The output power of steam turbine

$$P_{tb,s} = (1 - y_s) \dot{m}_{2,s} (h_{2a,s} - h_{2b,s}) + y_s \dot{m}_{2,s} (h_{2a,s} - h_{2c,s}) \quad (6.2)$$

The output power of generator

$$P_{ge,s} = P_{tb,s} \eta_{ge} \quad (6.3)$$

The total power of pumps

$$P_{pu,s} = (1 - y_s) \dot{m}_{2,s} (h_{2e,s} - h_{2d,s}) + \dot{m}_{2,s} (h_{2g,s} - h_{2f,s}) \quad (6.4)$$

Heat injected in the water circuit

$$Q_{2,s} = \dot{m}_{2,s} (h_{2a,s} - h_{2g,s}) \quad (6.5)$$

The generator efficiency is the same of that in the cascade system, and the efficiency of Rankine cycle can be expressed as

$$\eta_{rk,s} = (P_{tb,s} - P_{pu,s} / \eta_{ge}) / Q_{2,s} \quad (6.6)$$

#### 6.4.2 Stand-alone dish-Stirling system

In the stand-alone dish-Stirling system, Stirling engines with the same number of dish collectors are directly put on the focuses of the dish collectors. Water is used for cooling the Stirling engines.  $T_{H,s}$  is chosen to be equal to outlet temperature of air in dish receiver.  $T_{L,s}$  is chosen to be 310 K, the default expansion temperature in Fraser's dissertation<sup>[125]</sup> for the calculation of 4-95 NKII engine.  $k$  and  $\gamma$  are chosen the same value as that of the Stirling engines in the cascade system.

$$\eta_{sea,s} = \frac{T_{H,s} - T_{L,s}}{T_{H,s} + \frac{1 - e_s}{k - 1} \cdot \frac{T_{H,s} - T_{L,s}}{\ln \gamma}} \quad (6.7)$$

where,  $T_{R,s} = \frac{T_{H,s} - T_{L,s}}{\ln(T_{H,s}/T_{L,s})}$  and  $e_s = \frac{T_{R,s} - T_{L,s}}{T_{H,s} - T_{L,s}}$ .

The total power of Stirling engines

$$P_{sea,s} = n_{dc} A_{dc} I_r \eta_{dc} \eta_{sea,s} \quad (6.8)$$

## 6.5 Comparison with stand-alone system

The results presented in Table 6.3 are issued using design parameters with counterflow of two fluids in Stirling engine array as the default flow type. It is shown that the cascade system with design parameters can achieve higher efficiency compared to corresponding stand-alone systems. Although the efficiency of the Stirling engine array is lower, the efficiency of the Rankine cycle is higher. The overall output power of the cascade system is  $3.83 \times 10^4$  W higher.

Table 6.3 Some important results using design parameters

| Parameter     | Value  | Parameter      | Value             | Parameter   | Value                 |
|---------------|--------|----------------|-------------------|-------------|-----------------------|
| $\eta_{cs}$   | 0.1974 | $\eta_{sea,s}$ | 0.3786            | $P_{ge,s}$  | $5.826 \times 10^6$ W |
| $\eta_s$      | 0.1962 | $\eta_{rk}$    | 0.2660            | $P_{sea}$   | $3.552 \times 10^5$ W |
| $\eta_{diff}$ | 0.0062 | $\eta_{rk,s}$  | 0.2678            | $P_{sea,s}$ | $4.909 \times 10^5$ W |
| $\eta_{sea}$  | 0.3407 | $P_{ge}$       | $6 \times 10^6$ W | $P_{diff}$  | $3.830 \times 10^4$ W |

### 6.5.1 Effects of $I_r$

It is found that  $I_r$  can affect the efficiency difference of cascade system and stand-alone systems  $\eta_{diff}$ . Figure 6-4 shows curve fits of efficiency differences  $\eta_{diff}$  versus  $I_r$  with a series of different Stirling engine array power ratios. As it can be seen, for a high  $I_r$  ( $I_r > 550$  W/m<sup>2</sup>),  $\eta_{diff} > 0$ , the cascade system can achieve a higher efficiency than corresponding stand-alone systems. For a low  $I_r$  ( $I_r < 550$  W/m<sup>2</sup>),  $\eta_{diff}$  may be negative. At this situation, the cascade system achieves a lower efficiency than corresponding stand-alone systems. This may be explained that instead of cooling water in the stand-alone dish-Stirling system, condensed water of Rankine cycle is used to cool the Stirling engines, which jeopardizes the heat dissipation and leads to a lower power of the Stirling engines. For a low  $I_r$ , the increased power of steam turbine due to absorbed heat by the condensed water is lower than the power loss of the Stirling engines. It can also be found that higher  $I_r$  can achieve higher  $\eta_{diff}$ , which can be interpreted as the heat absorbed by the condensed water increases

with  $I_r$ . So a higher  $I_r$  location is always more suitable for cascade system. This means  $I_r$  is a key factor to determine whether cascade system should be applied in a certain location.

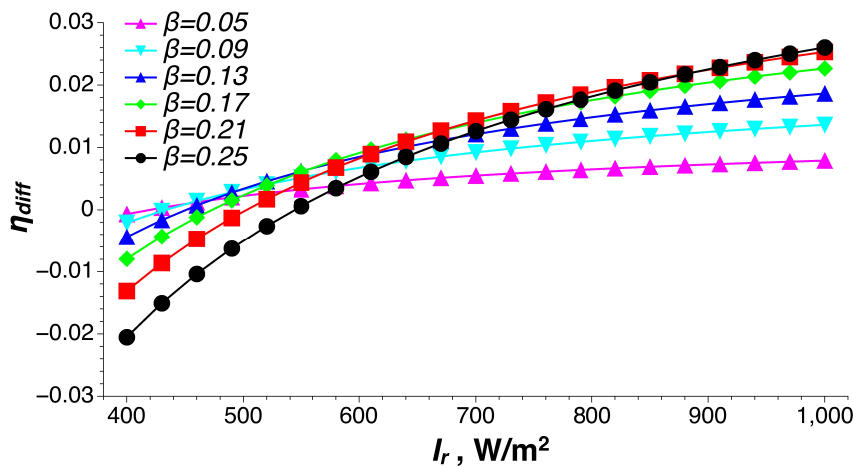


Figure 6-4 Curve fits of efficiency difference  $\eta_{diff}$  versus  $I_r$

### 6.5.2 Effects of $\beta$

As it can be seen in Table 6.3, the  $\eta_{diff}$  is very small with the design parameters given above. A reason  $\eta_{diff}$  to be so small is that  $\beta$ , the ratio of power of Stirling engines to the total power, is very small, the heat released by the Stirling engine array is a small portion of the heat absorbed in the Rankine cycle. So increase  $\beta$  may achieve higher  $\eta_{diff}$ . The relationship between  $\eta_{diff}$  and  $\beta$  under a series of  $I_r$  is shown in Figure 6-5. It can be found that, for a high  $I_r$ , increase  $\beta$  may achieve a higher  $\eta_{diff}$ , but there is a limit. For  $I_r = 900\text{W/m}^2$ , the maximum  $\eta_{diff} = 0.0228$  appears at  $\beta = 0.23$ . For a low  $I_r$ ,  $\eta_{diff}$  is negative, increase  $\beta$  will reduce  $\eta_{diff}$ . This can be explained as the same reason in Section 6.5.1.

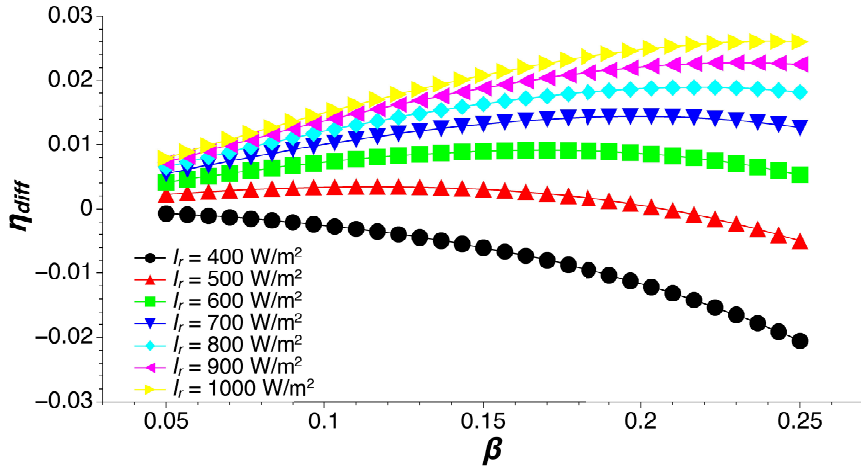


Figure 6-5 Curve fits of efficiency difference  $\eta_{diff}$  versus  $\beta$

### 6.5.3 Effects of flow type

Flow type between heating and cooling streams can affect the efficiency of Stirling engine array. Parallel flow, compared to counterflow, leads to higher Stirling engine efficiency in the first columns of the array for lower cooling temperature, while lower Stirling engine efficiency in the last columns for higher cooling temperature.

Table 6.4 shows the different results of the two flow types. The fit curves of temperature series of the heating and cooling fluids and the efficiency of Stirling engines in different columns are shown in Figure 6-6 and 6-7.

Table 6.4 Results of Stirling engine array with two different flow types

| x  | Parallel flow |           |           |              | Counterflow |           |           |              |
|----|---------------|-----------|-----------|--------------|-------------|-----------|-----------|--------------|
|    | $T_{1,i}$     | $T_{2,i}$ | $P_{sea}$ | $\eta_{sea}$ | $T_{1,i}$   | $T_{2,i}$ | $P_{sea}$ | $\eta_{sea}$ |
|    | K             | K         | W         | -            | K           | K         | W         | -            |
| 1  | 1073.15       | 327.17    | 5000      | 0.3648       | 1073.15     | 348.09    | 4867      | 0.3601       |
| 2  | 1022.38       | 329.80    | 4630      | 0.3599       | 1023.25     | 345.48    | 4541      | 0.3562       |
| 3  | 974.35        | 332.29    | 4280      | 0.3544       | 975.82      | 343.00    | 4230      | 0.3520       |
| 4  | 928.90        | 334.65    | 3949      | 0.3485       | 930.75      | 340.65    | 3934      | 0.3474       |
| 5  | 885.91        | 336.88    | 3635      | 0.3419       | 887.94      | 338.42    | 3654      | 0.3424       |
| 6  | 845.26        | 339.00    | 3338      | 0.3347       | 847.28      | 336.29    | 3387      | 0.3370       |
| 7  | 806.82        | 341.00    | 3057      | 0.3269       | 808.69      | 334.28    | 3134      | 0.3312       |
| 8  | 770.49        | 342.91    | 2792      | 0.3184       | 772.06      | 332.37    | 2894      | 0.3248       |
| 9  | 736.16        | 344.71    | 2541      | 0.3090       | 737.31      | 330.55    | 2666      | 0.3180       |
| 10 | 703.75        | 346.43    | 2304      | 0.2989       | 704.37      | 328.82    | 2450      | 0.3106       |

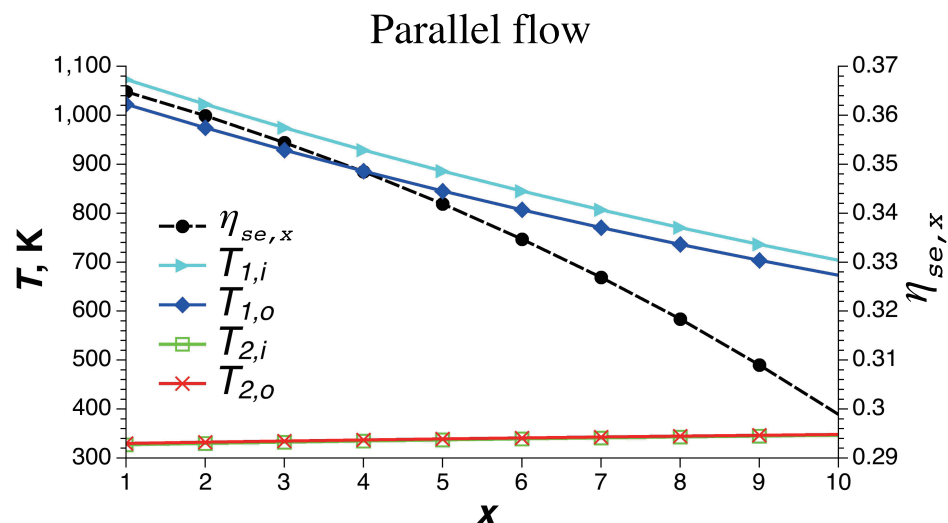


Figure 6-6 Parallel flow: Temperature series of two fluids and efficiency of Stirling engines in column x

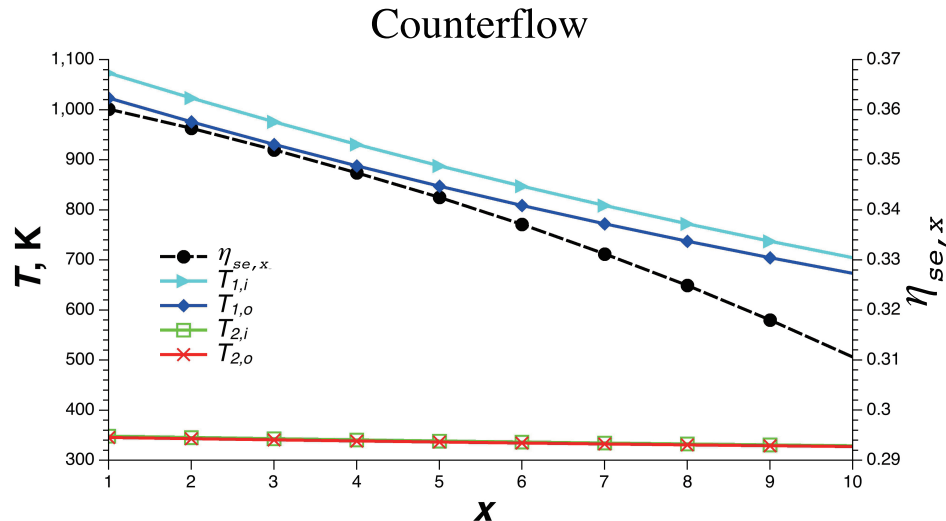
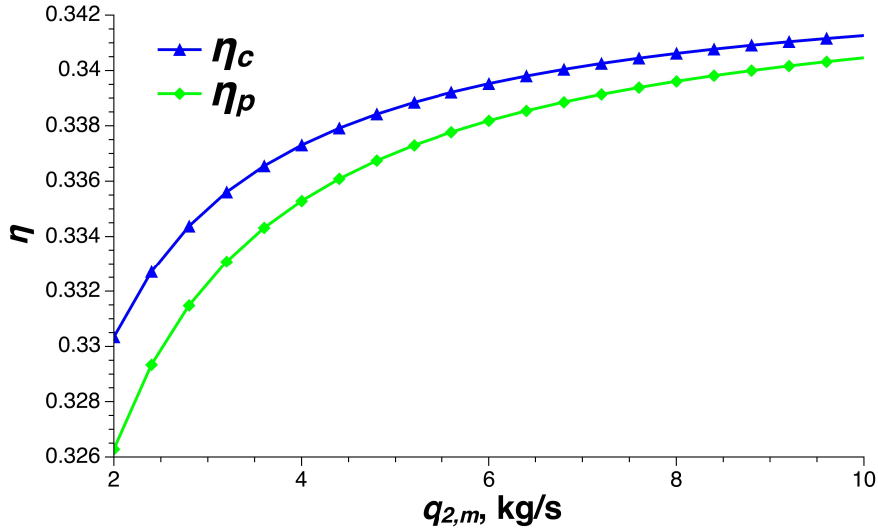


Figure 6-7 Counterflow: Temperature series of two fluids and efficiency of Stirling engines in column  $x$

It can be concluded that the temperature increment of cooling fluid is much smaller than the temperature decrement of heating fluid due to their large difference of  $c_p \dot{m}$ , which leads to a small difference of overall efficiency of Stirling engine array between the two flow types.

To find out a clear difference of the two flow types, a simple model of Stirling engine array is developed with air as the heating fluid and water as the cooling fluid.  $T_{1,i}, T_{1,o}, T_{2,i}, q_{1,m}$  are fixed and chosen the same values as in the cascade system. Change the value of  $q_{2,m}$ , and the corresponding Stirling engine array efficiency of the two flow types ( $\eta_p$  and  $\eta_c$ ) can be obtained. Figure 6-8 shows the efficiency of Stirling engine array with different  $q_{2,m}$  in two flow types. It can be found that counterflow has a higher efficiency than parallel flow, and with lower  $q_{2,m}$  comes with higher efficiency difference.

For a system with large difference of  $c_p \dot{m}$  of two fluids, that means one fluid can only achieve a small temperature rise (drop) compared to the other fluid, will lead to a small difference of two flow types. For a system with similar difference of  $c_p \dot{m}$ , use the counterflow can achieve a higher efficiency.

Figure 6-8 Efficiency of Stirling engine array with different  $q_{2,m}$ 

## 6.6 Conclusion

In this chapter, an effective typical cascade system proposed in Chapter 2 is chosen for evaluation. This cascade system uses two different types of collectors and two different power generation methods. Steam Rankine cycle is applied for this system for its widely applied applications. Reasonable parameters are selected and the system model is developed. Two stand-alone systems are chosen as the comparison systems for system evaluation. They use the same dish collectors and trough collectors of the cascade system. Simulations of the cascade system are carried out and results are compared with corresponding stand-alone systems.

Results show that  $I_r$  is the key factor to determine whether cascade system should be applied in a certain location. Compared to corresponding stand-alone systems, the cascade system can achieve a higher efficiency with high solar irradiance ( $I_r > 550 \text{ W/m}^2$ ). The directions to increase the efficiency difference between cascade system and corresponding stand-alone systems are also considered. To design a cascade system including Stirling engine array, flow type of fluids for heating and cooling Stirling engine array is also required to be considered.

## Chapter 7 Experiment research on solar thermal power platform

In Chapter 3, MATLAB is used as the simulation tool to develop the models of the key components of solar thermal systems. Based on these component models, the cascade system model is developed. The mechanism of trough collector is studied. Under the condition of assumption of uniform overall heat transfer coefficient, the correlations between temperature rise, mass flow of the HTF, solar direct normal irradiance, ambient temperature and other factors were derived. The theoretical formula of the efficiency of trough collector is obtained. The heat losses of dish collector were analyzed in detail. A thermal network model of the dish receiver is established. Using classical heat transfer correlations, each temperature node of the heat network is solved and the thermal efficiency of the dish collector is obtained.

To understand the solar thermal power generation system more deeply and to validate the applicable range and error of the proposed component models, a platform includes trough concentrating collector, dish concentrating collector and ORC system was built in Wuhan. The construction of this solar thermal platform provides a good foundation for future cascade solar power generation system.

### 7.1 Platform introduction

Figure 7-1 shows the schematic structure of the solar thermal power platform. Three circuits, the air circuit, oil circuit and organic fluid circuit, are created by different fluids. In the air circuit, air in the environment is first compressed in the compressor, and warmed by a heater, then heated in dish receiver, then flows into the air-oil heat exchanger to provide heat for Rankine cycle and finally through the water cooling system back to the environment. In the oil circuit, the oil is first heated in the trough collector and then flows into the air-oil heat exchanger to obtain the heat provided by the air. The heated oil flows into the evaporator of the ORC system to provide heat for the ORC system, then through the pump back to the trough collector. In the organic fluid circuit, the organic fluid first absorbs the heat provided by the oil in the evaporator, then flows into the ORC turbine for expansion. After expansion,

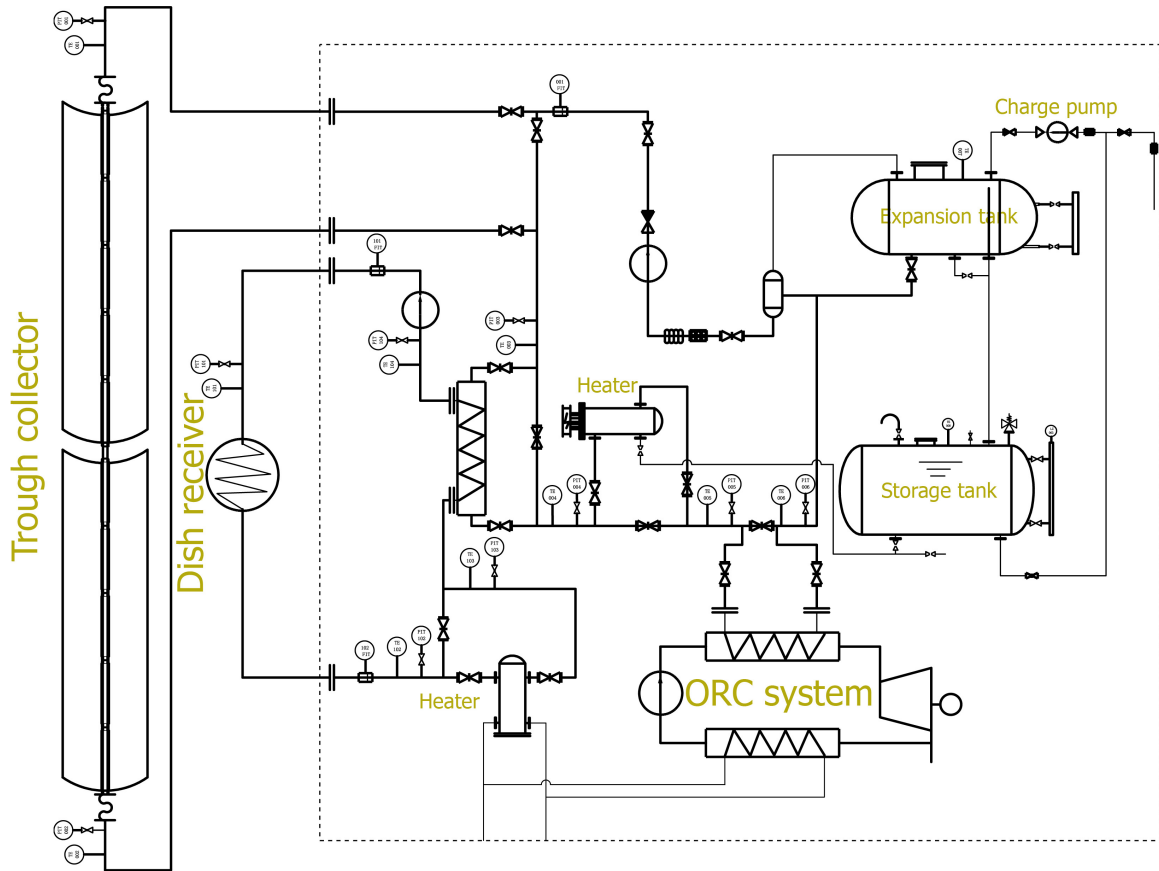


Figure 7-1 Schematic structure of the platform

the organic fluid flows into the regenerator to recover part of the overheating heat, then into the condenser, and back to the regenerator to reuse the rejected heat, then through the pump back to the evaporator.

The following describes key components of the platform.

### 7.1.1 Trough collector

The trough collector is east-west oriented due to land constrains. It is made of parabolic reflector, receiver and bracket. Figure 7-2 shows the photo of the trough collector. The reflector is 20 m long, and 2.55 m wide. The receiver is an SEIDO-I type product of Sunda-Solar Company. It consists of a glass tube and a metal black pipe, vacuum is maintained between the two to reduce heat loss. The external diameter of the glass tube is 0.11 m, and the internal diameter is 0.106 m. The external diameter of the metal tube is 0.038 m, and

the internal diameter is 0.035 m. The bracket is applied to support the reflector and receiver. Its structure is safe enough to resist common windy, stormy and snowy weather conditions. The mechanical structures for rotation, positioning and connection are simple and reliable, easy for mounting, dismounting and transportation, and convenient for operation and maintenance. Single-axis tracking system is applied for the trough collector system. The program algorithm is used for real-time automatic tracking with small tracking error. Manual mode is also an optional choice. The buttons in the control cabinet make it convenient to adjust the collector to a desired direction. In addition, it provides automatic protection and manual operation protection in case of emergency.

SINOPEC L-QD350 synthetic thermal oil is applied as the HTF of the trough collector system. Its typical physical parameters are provided from the seller.

### 7.1.2 Dish collector

Figure 7-3 shows the photo of the dish collector. The reflector is made of multiple curved mirrors. When the aperture is facing to the sun, each of the mirrors reflects the sunlight to the focal point. A self-designed receiver is mounted at the focal point of the dish reflector, as shown at top of the photo in Figure 7-3. The key parameters of the dish collector are listed in Table 7.1.

Table 7.1 Key parameters of the designed dish collector

| Parameter        | Value          | Parameter         | Value              | Parameter        | Value      |
|------------------|----------------|-------------------|--------------------|------------------|------------|
| $d_{cav}$        | 0.45 m         | $\epsilon_{insu}$ | 0.6                | $\theta_{dc}$    | $20^\circ$ |
| $\delta_{insu}$  | 0.11 m         | $\alpha_{cav}$    | 0.87               | $\gamma$         | 0.97       |
| $dep_{cav}$      | 0.45 m         | $\delta_a$        | 0.002 m            | $\eta_{shading}$ | 1          |
| $d_{ap}$         | 0.25 m         | $d_{i,1}$         | 0.07 m             | $\rho$           | 0.91       |
| $\lambda_{insu}$ | 0.06 W/(m · K) | $A_{dc}$          | $23.3 \text{ m}^2$ |                  |            |

The YYGN-GR-1A automatic two-axis tracking control system is used for the dish collector system. Both algorithm tracking method and sensor tracking method are applied for the tracking system. Usually, at the beginning of the focusing process, manual mode is ap-

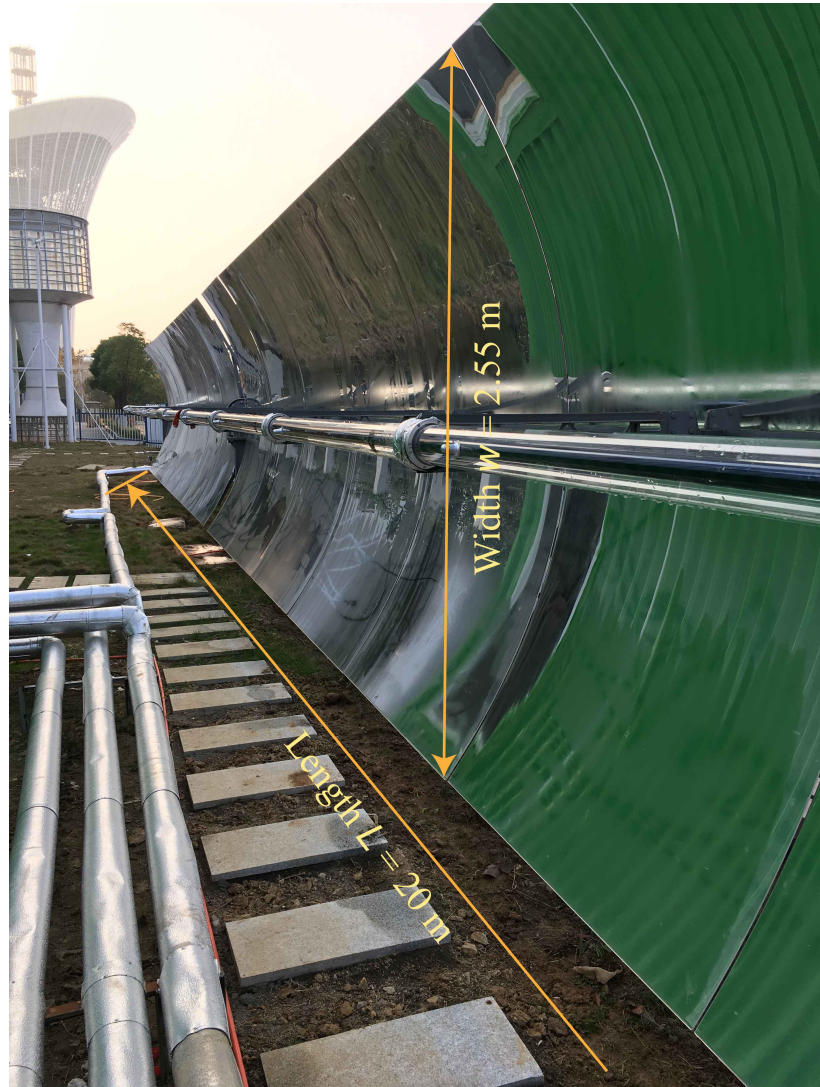


Figure 7-2 Trough collector of the platform

plied to roughly rotate the collector towards the sun. Then switch to the automatic mode to precisely face to the sun. And the algorithm tracking method will take over and keep tracking the sun. This provides a more reliable tracking system with tracking error of less than  $0.2^\circ$  without cumulative error. The control cabinet of the dish collector provides mechanical, electrical and other optional controls. It also monitors the wind speed and provides the function of set maximum wind speed for safety. When the wind is too strong, it will rotate the collector to a safe angle (facing the zenith).



Figure 7-3 Dish collector of the platform

### 7.1.3 ORC system

Hot oil (heated by the trough collector and/or the heater) is supplied to the ORC system. In the hot loop, input temperature of the supplied oil is 180°C, and output temperature is 160°C. Flow rate of 0.44 kg/s is required to reach the nominal output gross power 1.5 kW. In the cold loop, input temperature of tap water is 30°C, and output temperature is 37°C. The water flow rate is about 0.83 kg/s.

Figure 7-4 shows photos of the ORC system. It is made of evaporator, high speed ORC turbine, generator, regenerator, condenser, organic working medium pump, electrical control

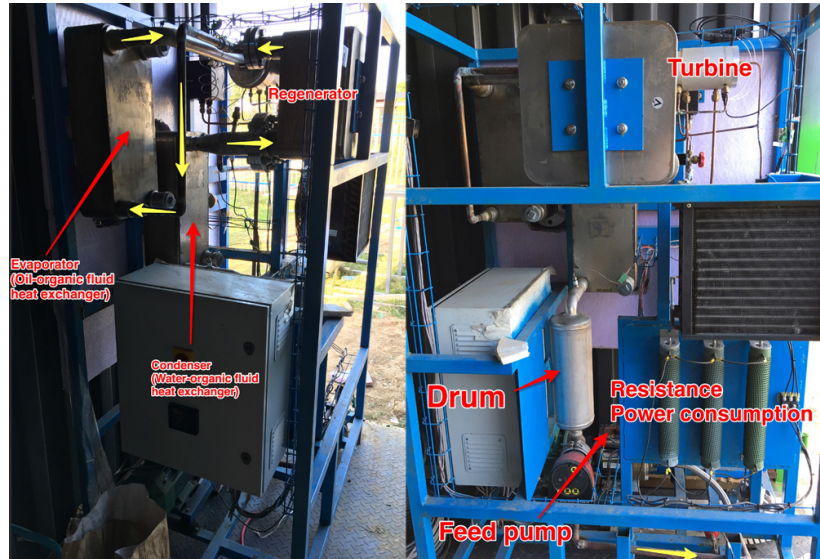


Figure 7-4 ORC system of the platform

cabinet and the connection pipes.

The control cabinet provide a touch screen to control the ORC system. Both automatic mode and manual mode are provided. In automatic mode, all the start up work and shut down work will be completed by procedure automatically. In manual mode, you can manually set the parameters such as the speed of the organic fluid pump to provide precise control of the system.



Figure 7-5 Control screen of the ORC system

### 7.1.4 Piping system

Piping system provides the basis for fluid flow and heat exchange. Plus, it provides thermal insulation for hot fluids. Meters, pumps, valves, tanks and heaters are arranged in the piping system to maintain the normal and orderly operation.

Two heaters are used in the platform to increase the temperatures of the fluids (air and oil) to reach the experiment requirements when the solar irradiance is not enough. Both heaters have temperature sensors to maintain the temperatures of the outlet fluids by changing the power.

## 7.2 Experiments

In order to test the performance of the platform and validate the proposed models, relevant experiments were carried out.

### 7.2.1 Trough collector experiment

#### 7.2.1.1 Experiment purpose

The purpose of the experiment is to study the effects of solar irradiance, flow rate, inlet temperature of the working fluid on the thermal performance of the collector, and to validate the trough collector model established in Section 3.1.1.

#### 7.2.1.2 Experiment steps

The operation steps are as follows,

- (1) Complete the preparation work. Ensure that the devices and components are all properly connected and can work normally.
- (2) Initialize the solar radiometer. Adjust the direction of the solar radiometer to get the normal irradiation value, make sure the light spot passing through the tube falls in the designed position.
- (3) Open the valves in the oil circuit, then turn on the oil pump.
- (4) Turn on the motor of the trough collector tracking system. Synchronize the time of the tracking system, and turn on the automatic mode to make the trough system tracking the sun automatically.

- (5) Adjust the parameters to meet the designed conditions. When the data is stable, record and save the data collected by the data acquisition system.
- (6) Finish the experiment when all the design conditions have been tested.
- (7) Rotate the trough collector to face towards the horizontal position on the control panel.  
Turn off the motor when the trough collector is ready in place.
- (8) Turn off the oil pump.

### 7.2.1.3 Experiment cases

Considering the uncontrollability and continuity of the direct normal irradiance (DNI) in a clear day, when DNI is a control variable, solar irradiance values can not be controlled as design values and should be measured values. When DNI is required to be a constant, total experiment time should be limited to reduce the impact of DNI variation.

Table 7.2 Designed cases of the solar trough system

| Case | DNI ( $\text{W/m}^2$ ) | Flow rate ( $\text{kg/s}$ ) | Inlet temperature (K) |
|------|------------------------|-----------------------------|-----------------------|
| 1-10 | Live values            | 0.2                         | 433.2                 |
| 11   | Live value             | 0.1                         | 433.2                 |
| 12   | Live value             | 0.2                         | 433.2                 |
| 13   | Live value             | 0.3                         | 433.2                 |
| 14   | Live value             | 0.4                         | 433.2                 |
| 15   | Live value             | 0.5                         | 433.2                 |
| 16   | Live value             | 0.2                         | 413.2                 |
| 17   | Live value             | 0.2                         | 423.2                 |
| 18   | Live value             | 0.2                         | 433.2                 |
| 19   | Live value             | 0.2                         | 443.2                 |
| 20   | Live value             | 0.2                         | 453.2                 |

In table 7.2, Case 1 to Case 10 are completed at different times of a day or in different days. Case 11 to Case 15 are required to be completed within half an hour. It is worth noting

that, only 5 cases (Case 16 to Case 20) are designed with small temperature increment for the inlet temperature investigation due to the slow heating process of the oil heater. And the 5 cases are required to be completed within an hour.

#### 7.2.1.4 Data processing method

The specific heat of the oil is given as: when  $T = 373.15^\circ\text{C}$ ,  $c_p = 2.44 \times 10^3 \text{ J}/(\text{kg} \cdot \text{K})$ ; when  $T = 473.15^\circ\text{C}$ ,  $c_p = 2.88 \times 10^3 \text{ J}/(\text{kg} \cdot \text{K})$ . Linear interpolation method is applied,  $c_p = aT + b$ , where  $a = 4.4 \text{ J}/(\text{kg} \cdot \text{K}^2)$ ,  $b = 798.14 \text{ J}/(\text{kg} \cdot \text{K})$ .

$$\text{The absorbed heat of the oil } Q_{abs} = \int_{T=T_i}^{T=T_o} c_p \dot{m} dT = \frac{1}{2} a(T_o^2 - T_i^2) \dot{m} + b(T_o - T_i) \dot{m}.$$

The thermal efficiency of the trough collector

$$\eta_{tc} = \frac{Q_{abs}}{I_r w_{tc} L_{tc}} \quad (7.1)$$

To validate the simulation model, Equation (3.4) is required to be checked. In the simulation model,

$$\tilde{T}_o = T_{amb} + \frac{q''}{U(T_{abs})} + \exp\left(-\frac{U(T_{abs})\pi d_o L}{\dot{m}\tilde{c}_p}\right)(T_i - T_{amb} - \frac{q''}{U(T_{abs})}) \quad (7.2)$$

where  $T_{abs}$  is replaced by  $(T_i + T_o)/2$  ( $T_i$  and  $T_o$  are the measured values of inlet temperature and outlet temperature),  $\tilde{c}_p$  is the average specific heat obtained from  $(T_i + T_o)/2$ ,  $U(T_{abs})$  is obtained from<sup>[104]</sup>

$$U(T_{abs}) = 0.687257 + 0.001941(T_{abs} - T_{amb}) + 0.000026(T_{abs} - T_{amb})^2 \quad (7.3)$$

$$q'' = \frac{I_r w_{tc} \rho \gamma \tau F_e K(\theta)}{\pi d_o} \quad (7.4)$$

$$K(\theta) = \cos \theta + 0.000884\theta - 0.00005369\theta^2 \quad (7.5)$$

So  $\widetilde{\eta}_{tc}$  from the simulation results can be obtained for comparison with the one in Equation (7.1) obtained from experiment.

$$\widetilde{\eta}_{tc} = \frac{\dot{m}\tilde{c}_p(\tilde{T}_o - T_i)}{I_r w_{tc} L_{tc}} \quad (7.6)$$

## 7.2.2 Dish collector experiment

### 7.2.2.1 Experiment purpose

The purpose of the experiment is to study the effects of solar irradiance, flow rate, inlet temperature of the working fluid on the thermal performance of the collector, and to validate the dish receiver model established in Section 3.1.2.

### 7.2.2.2 Experiment steps

The operation steps are as follows,

- (1) Complete the preparation work. Ensure that the devices and components are all properly connected and can work normally.
- (2) Initialize the solar radiometer. Adjust the direction of the solar radiometer to get the normal irradiation value, make sure the light spot passing through the tube falls in the designed position.
- (3) Turn on the water cooling system.
- (4) Open the valves of the inlet and outlet of the air circuit, then turn on the air compressor.
- (5) Use manual mode to rotate the collector toward the sun. Then switch to the automotive mode.
- (6) Adjust the parameters to meet the designed conditions. When the data is stable, record and save the data collected by the data acquisition system.
- (7) Finish the experiment when all the designed conditions have been tested.
- (8) Rotate the collector to the up most position (facing the zenith). Turn off the compressor, turn off the outlet and inlet valves, turn off the water cooling system.

### 7.2.2.3 Experiment cases

In Table 7.3, Case 1 to Case 10 are completed at different times of a day or in different days. Case 11 to Case 15 are required to be completed within half an hour. Case 16 to Case 20 are required to be completed within an hour.

### 7.2.2.4 Data processing method

Known the pressure ( $p = 4 \times 10^5$  Pa) and the measured temperature, the inlet enthalpy ( $h_i$ ) and outlet enthalpy ( $h_o$ ) of the air can be obtained.

Table 7.3 Designed cases of the solar dish system

| Case | DNI ( $\text{W}/\text{m}^2$ ) | Flow rate ( $\text{kg}/\text{s}$ ) | Inlet temperature (K) |
|------|-------------------------------|------------------------------------|-----------------------|
| 1-10 | Live values                   | 0.03                               | 423.2                 |
| 11   | Live value                    | 0.01                               | 423.2                 |
| 12   | Live value                    | 0.02                               | 423.2                 |
| 13   | Live value                    | 0.03                               | 423.2                 |
| 14   | Live value                    | 0.04                               | 423.2                 |
| 15   | Live value                    | 0.05                               | 423.2                 |
| 16   | Live value                    | 0.03                               | 383.2                 |
| 17   | Live value                    | 0.03                               | 403.2                 |
| 18   | Live value                    | 0.03                               | 423.2                 |
| 19   | Live value                    | 0.03                               | 443.2                 |
| 20   | Live value                    | 0.03                               | 463.2                 |

The absorbed heat of the air  $Q_{abs} = \dot{m}(h_o - h_i)$ .

The thermal efficiency of the dish collector  $\eta_{dc} = \frac{Q_{abs}}{I_r A_{dc}}$ .

To validate the simulation model in Section 3.1.2, the thermal network of dish receiver (see Figure 3-4) are solved from the equations in Section 3.1.2.

The simulation efficiency of the dish collector  $\widetilde{\eta}_{dc} = \frac{Q_{dr,1}}{I_r A_{dc}}$ .

## 7.3 Result analysis

### 7.3.1 Trough collector experiment result analysis

Influences of solar irradiance, flow rate and inlet temperature of the working fluid on the collector thermal performance are concerned.

Table 7.4 Experiment results of Case 1 to Case 10 of the trough collector

| Case | DNI (W/m <sup>2</sup> ) | $\dot{m}$ (kg/s) | $T_i$ (K) | $T_o$ (K) | $T_{amb}$ (K) |
|------|-------------------------|------------------|-----------|-----------|---------------|
| 1    | 353                     | 0.2              | 433.2     | 452.9     | 277.8         |
| 2    | 408                     | 0.2              | 433.2     | 456.2     | 278.0         |
| 3    | 464                     | 0.2              | 433.2     | 459.4     | 278.2         |
| 4    | 476                     | 0.2              | 433.2     | 460.2     | 278.4         |
| 5    | 497                     | 0.2              | 433.2     | 461.3     | 278.4         |
| 6    | 508                     | 0.2              | 433.2     | 462.0     | 278.6         |
| 7    | 553                     | 0.2              | 433.2     | 464.6     | 278.6         |
| 8    | 610                     | 0.2              | 433.2     | 467.9     | 278.8         |
| 9    | 637                     | 0.2              | 433.2     | 469.3     | 278.8         |
| 10   | 652                     | 0.2              | 433.2     | 470.2     | 278.9         |

### 7.3.1.1 Influence of $I_r$

Tested results of Case 1 to Case 10 are listed in Table 7.4. It is noteworthy that due to the uncontrollability and variability of solar radiation intensity, the measured values of solar irradiance are not evenly distributed. Figure 7-6 shows the influence of solar irradiance on the thermal efficiency of the trough collector. Simulation results are also included. The simulation parameters are set to be the same as the experiment.

It can be found that both the experimental data and simulation results show the same trend of thermal efficiency and solar irradiance. The thermal efficiency increases with DNI. There exists small deviations between the experimental data and simulation results, between 0% to 1%.

### 7.3.1.2 Influence of $\dot{m}$

Tested results of Case 11 to Case 15 are listed in Table 7.5. Figure 7-7 shows the influence of inlet flow rate on the thermal efficiency of the trough collector. The data points on the figure are collected within a short time, so the irradiance can be regarded as unchanged.

It can be found that higher flow rate leads to higher efficiency. This is obvious for

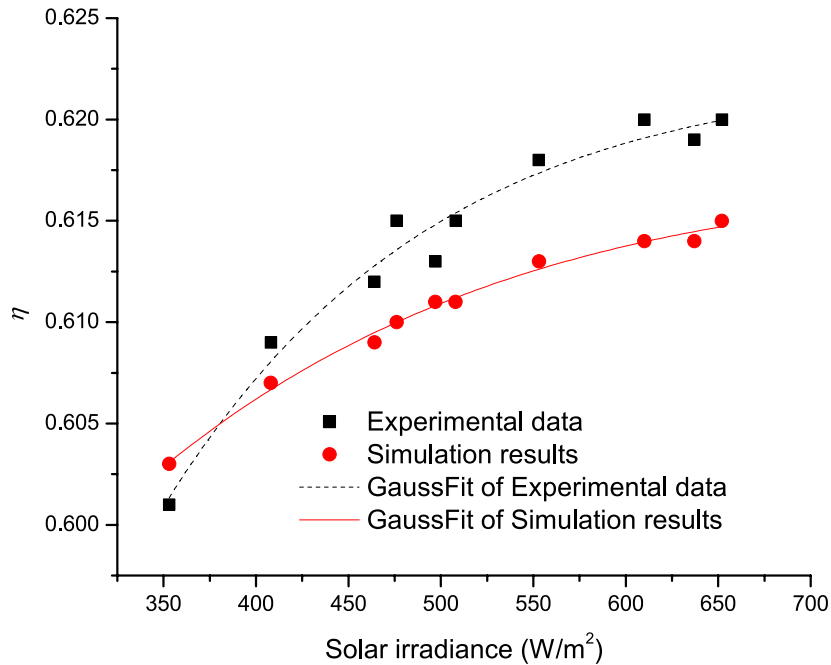


Figure 7-6 Influence of solar irradiance on the thermal efficiency

Table 7.5 Experiment results of Case 11 to Case 15 of the trough collector

| Case | DNI (W/m <sup>2</sup> ) | $\dot{m}$ (kg/s) | $T_i$ (K) | $T_o$ (K) | $T_{amb}$ (K) |
|------|-------------------------|------------------|-----------|-----------|---------------|
| 11   | 612                     | 0.1              | 433.2     | 501.0     | 286.3         |
| 12   | 615                     | 0.2              | 433.2     | 468.2     | 286.4         |
| 13   | 615                     | 0.3              | 433.2     | 456.7     | 286.6         |
| 14   | 614                     | 0.4              | 433.2     | 451.2     | 286.7         |
| 15   | 612                     | 0.5              | 433.2     | 447.6     | 286.7         |

higher flow rate takes more heat away from the receiver, leads to lower receiver temperature distribution and hence less thermal losses. The experimental data and simulation result are in good agreement. Small deviations also exist between the experimental data and simulation results, between 0.4% to 0.9%. The simulation efficiency is lower than corresponding experimental efficiency. This may be interpreted that, the correlation of thermal loss coefficient  $U$  and  $T_{abs}$  (see Equation 7.3) is for LS-3 type collector, which is not ideal for the

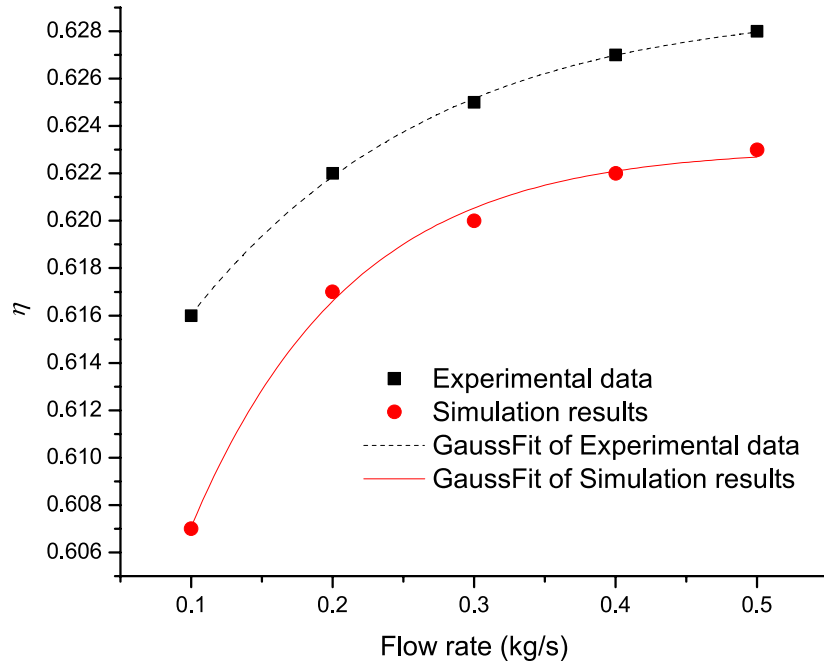


Figure 7-7 Influence of inlet flow rate on the thermal efficiency

trough collector product used in the platform. Future tests will provide more data for a more accurate correlation for the SEIDO6-I product.

### 7.3.1.3 Influence of $T_i$

Table 7.6 Experiment results of Case 16 to Case 20 of the trough collector

| Case | DNI (W/m <sup>2</sup> ) | $\dot{m}$ (kg/s) | $T_i$ (K) | $T_o$ (K) | $T_{amb}$ (K) |
|------|-------------------------|------------------|-----------|-----------|---------------|
| 16   | 616                     | 0.2              | 413.2     | 449.7     | 289.5         |
| 17   | 614                     | 0.2              | 423.2     | 458.8     | 288.3         |
| 18   | 610                     | 0.2              | 433.2     | 467.9     | 288.7         |
| 19   | 618                     | 0.2              | 443.2     | 477.7     | 288.9         |
| 20   | 615                     | 0.2              | 453.2     | 486.8     | 286.3         |

Tested results of Case 16 to Case 20 are listed in Table 7.9. Figure 7-8 shows the influ-

ence of inlet flow rate on the thermal efficiency of the trough collector.

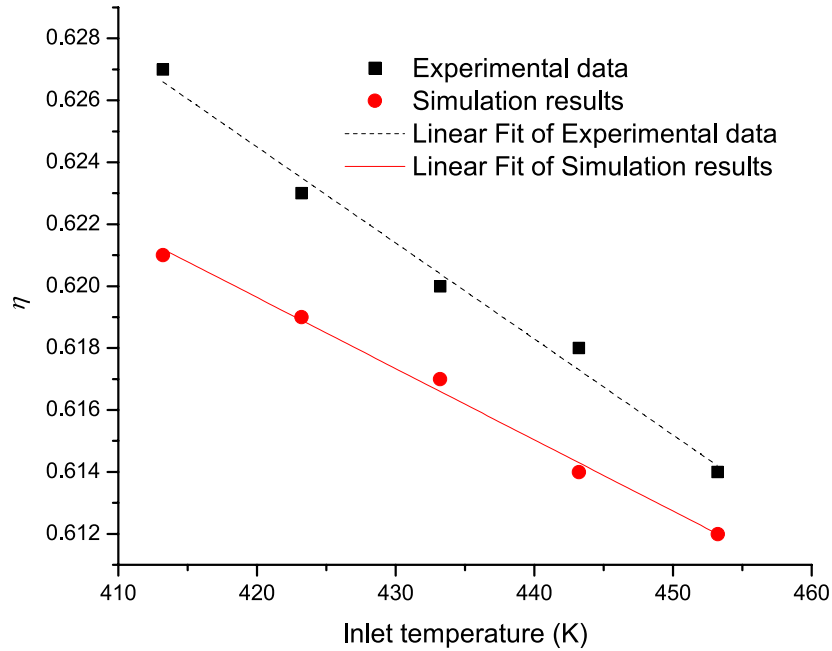


Figure 7-8 Influence of inlet temperature on the thermal efficiency

Both the experimental data and simulation results show that, higher inlet temperature leads to lower efficiency. This is obvious for higher inlet temperature leads to higher receiver temperature distribution and hence more thermal losses. Small deviations also exist between the experimental data and simulation results, between 0.7% to 1.5%. The simulation efficiency is lower than corresponding experimental efficiency. This can be interpreted as the same reason of inaccurate thermal loss coefficient  $U$ .

### 7.3.2 Dish collector experiment result analysis

Influences of solar irradiance, flow rate and inlet temperature of the working fluid on the collector thermal performance are concerned.

#### 7.3.2.1 Influence of $I_r$

Tested results of Case 1 to Case 10 are listed in Table 7.7. It is noteworthy that the measured values of solar irradiance are not evenly distributed due to the uncontrollability and variability of solar radiation intensity. Figure 7-9 shows the influence of solar irradiance

Table 7.7 Experiment results of Case 1 to Case 10 of the dish collector

| Case | DNI (W/m <sup>2</sup> ) | $\dot{m}$ (kg/s) | $T_i$ (K) | $T_o$ (K) | $T_{amb}$ (K) |
|------|-------------------------|------------------|-----------|-----------|---------------|
| 1    | 303                     | 0.03             | 423.2     | 552.1     | 282.1         |
| 2    | 358                     | 0.03             | 423.2     | 576.4     | 282.5         |
| 3    | 414                     | 0.03             | 423.2     | 602.3     | 283.2         |
| 4    | 426                     | 0.03             | 423.2     | 607.5     | 283.4         |
| 5    | 512                     | 0.03             | 423.2     | 646.0     | 285.0         |
| 6    | 596                     | 0.03             | 423.2     | 682.7     | 287.4         |
| 7    | 620                     | 0.03             | 423.2     | 692.4     | 289.2         |
| 8    | 641                     | 0.03             | 423.2     | 701.5     | 289.5         |
| 9    | 658                     | 0.03             | 423.2     | 708.7     | 289.4         |
| 10   | 683                     | 0.03             | 423.2     | 719.4     | 289.5         |

on the thermal efficiency of the dish collector. Simulation results are also included. The simulation parameters are set to be the same as the experiment.

It can be found that the thermal efficiency increases with solar irradiance when DNI is less than 600 W/m<sup>2</sup>. When DNI is larger than 600 W/m<sup>2</sup>, higher irradiance leads to higher wall temperature and hence more radiation loss, which jeopardizes the thermal efficiency when solar irradiance increases. The discrepancy of the experimental data and simulation data may be interpreted for the insulation condition. The out wall temperature of the insulation layer is higher than expected, which proves that the isolation condition is not good enough.

To clearly show the influence of higher DNI, a simulation of the dish collector model was carried out. The inlet air temperature is set to be 423.2 K, and the flow rate is set to be 0.03 kg/s. The environment temperature was set to be 283.2 K and the wind speed is set to be 0.4 m/s. The simulation results are shown in Figure 7-10. It can be found that there exists an optimum DNI for a specific receiver to achieve the highest thermal efficiency. For the receiver used in the platform, the optimum DNI is about 600 W/m<sup>2</sup>.

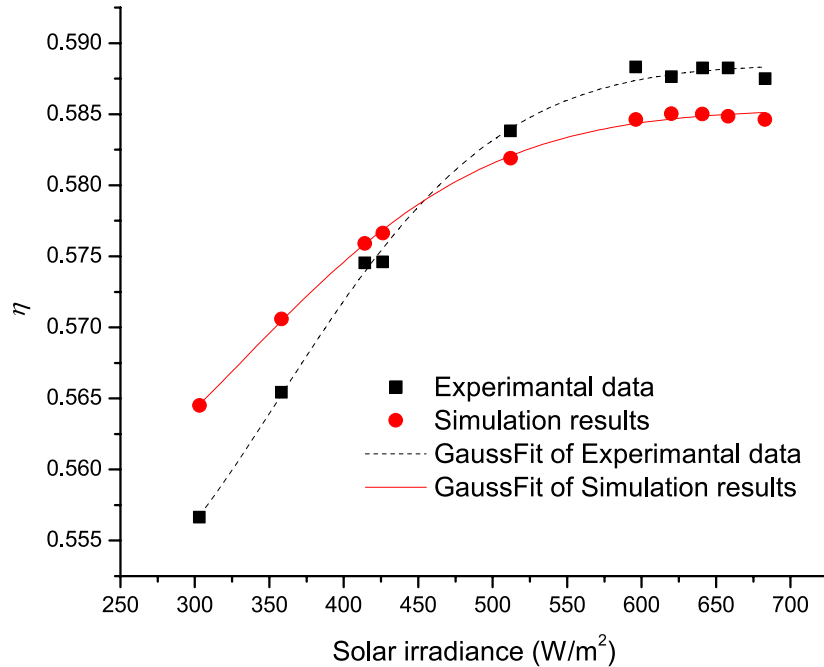


Figure 7-9 Influence of solar irradiance on the thermal efficiency

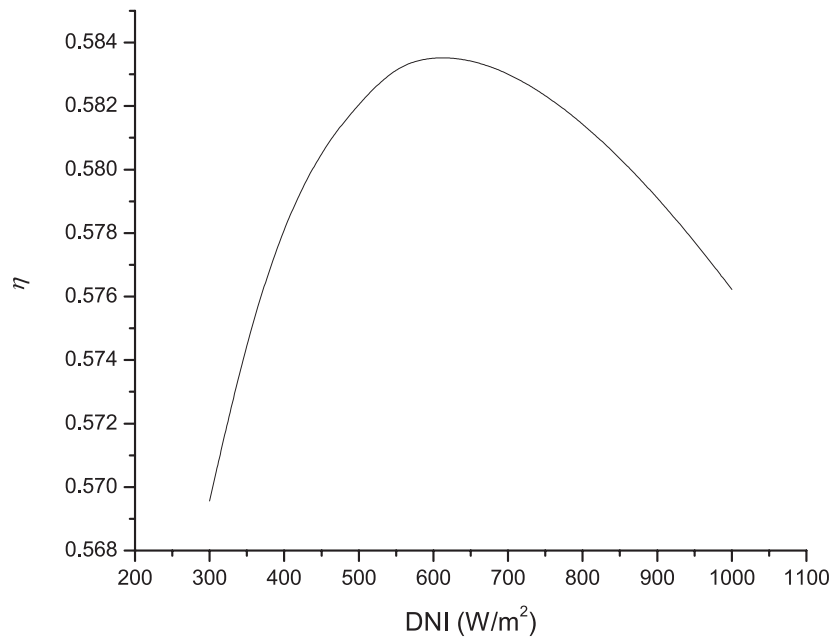


Figure 7-10 Simulation results of influence of solar irradiance on the thermal efficiency

### 7.3.2.2 Influence of $\dot{m}$

Tested results of Case 11 to Case 15 are listed in Table 7.8. Figure 7-11 shows the influence of inlet flow rate on the thermal efficiency of the dish collector. The data points on

Table 7.8 Experiment results of Case 11 to Case 15 of the dish collector

| Case | DNI ( $\text{W}/\text{m}^2$ ) | $\dot{m}$ ( $\text{kg}/\text{s}$ ) | $T_i$ (K) | $T_o$ (K) | $T_{amb}$ (K) |
|------|-------------------------------|------------------------------------|-----------|-----------|---------------|
| 11   | 613                           | 0.01                               | 423.2     | 950.7     | 286.3         |
| 12   | 615                           | 0.02                               | 423.2     | 783.9     | 286.4         |
| 13   | 616                           | 0.03                               | 423.2     | 691.8     | 286.6         |
| 14   | 614                           | 0.04                               | 423.2     | 634.9     | 286.7         |
| 15   | 613                           | 0.05                               | 423.2     | 597.8     | 286.7         |

the figure are collected within a short time, so the irradiance can be regarded as unchanged.

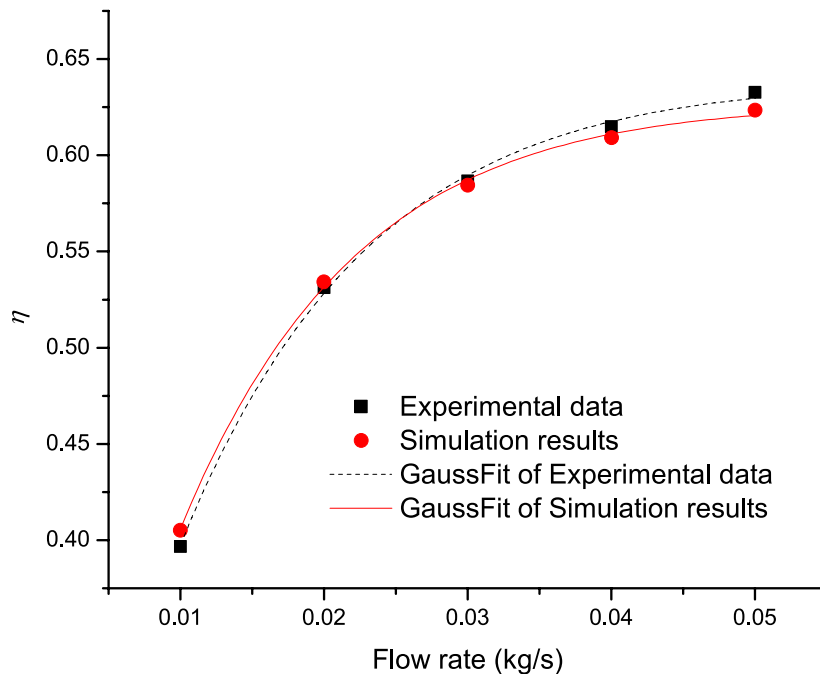


Figure 7-11 Influence of inlet flow rate on the thermal efficiency

It can be found that higher flow rate leads to higher efficiency. This is obvious for higher flow rate takes more heat away from the receiver, leads to lower temperature distribution and hence less thermal losses. The experimental data and simulation result are in good agreement.

### 7.3.2.3 Influence of $T_i$

Table 7.9 Experiment results of Case 16 to Case 20 of the dish collector

| Case | DNI ( $\text{W}/\text{m}^2$ ) | $\dot{m}$ ( $\text{kg}/\text{s}$ ) | $T_i$ (K) | $T_o$ (K) | $T_{amb}$ (K) |
|------|-------------------------------|------------------------------------|-----------|-----------|---------------|
| 16   | 616                           | 0.03                               | 383.2     | 661.9     | 289.0         |
| 17   | 615                           | 0.03                               | 403.2     | 676.4     | 288.8         |
| 18   | 612                           | 0.03                               | 423.2     | 690.6     | 288.8         |
| 19   | 617                           | 0.03                               | 443.2     | 707.8     | 288.9         |
| 20   | 615                           | 0.03                               | 463.2     | 722.2     | 288.9         |

Tested results of Case 16 to Case 20 are listed in Table 7.9. Figure 7-12 shows the influence of inlet flow rate on the thermal efficiency of the dish collector.

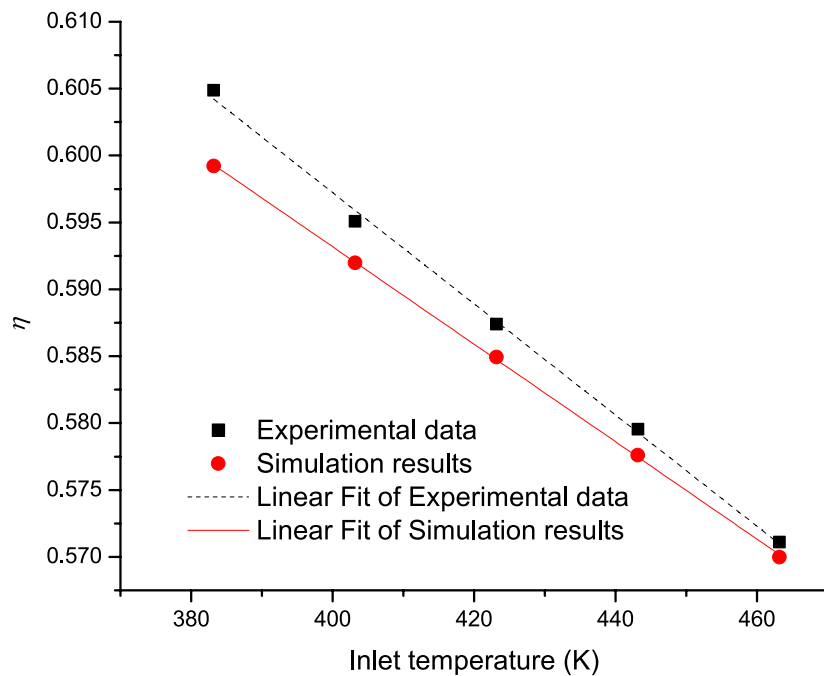


Figure 7-12 Influence of inlet temperature on the thermal efficiency

It can be found that higher inlet temperature leads to lower efficiency, This is obvious

for higher inlet temperature leads to higher temperature distribution and hence more thermal losses. The experimental data and simulation result are in good agreement.

## 7.4 Conclusion

The solar thermal power platform is a good start for the cascade solar thermal system. This chapter introduces the components and the circuits of the platform. According to the features of solar irradiance, special experiment cases are designed to investigate the impact of different factors on the system performance. Experiment steps are carefully arranged. Tests of the trough collector and the dish collector are carried out and the experimental results are collected for analysis.

The influence of solar irradiance, flow rate and inlet temperature of the working fluid on the performance of the collector model is investigated. The established trough collector model and dish collector model are validated by the experimental data.

The analysis of experimental data and simulation results shows that

- (1) The thermal efficiency of trough collectors is between 60.1% and 62.8% and the thermal efficiency of dish collectors is between 39.7% and 63.3% under the experimental conditions.
- (2) With regard to the effect of the considered factors on the performance of the collectors, the experimental data and the simulation results have the same trend. Higher working fluid flow rate leads to higher thermal efficiency, while higher working fluid inlet temperature leads to lower thermal efficiency.
- (3) For a specific dish receiver, there exists an optimum DNI to obtain the highest thermal efficiency.
- (4) The discrepancy of the experimental data and simulation results of the trough collector indicates that the thermal loss coefficient used in the modeling process is not ideal for the trough product used in the platform. It needs to be revised in the future.
- (5) The discrepancy of the experimental data and simulation results of the dish collector indicates that the thermal insulation of the dish collector needs to be inspected and strengthened.

## Chapter 8 Summaries and outlooks

### 8.1 Summaries

This chapter is needed to conclude the overall goals of our research. Considering the advantages and disadvantages of the existing solar thermal power generation technologies, a novel idea of energy cascade collection and energy cascade utilization for solar thermal power generation was put forward. Different types of collectors and thermodynamic cycles were used in the cascade system. The research of the cascade system was carried out with the selection of the system topology, the construction of the system model, the optimization of the system model and parameters, and the comparison with the independent system. The main works are concluded as follow:

- (1) Topological structures of cascade solar thermal power generation systems were proposed. According to the analysis of thermodynamic characteristics and the operating behavior of each component in the system, reasonable arranged topological structures of cascade systems were proposed. These systems use different thermodynamic cycles to harness the energy of different temperature zones. A reasonable cascade generation system can make full use of the mechanism models of power generation system to provide a basis for a more efficient cascade solar thermal generation system. In this thesis, several schemes of feasible topological structures of solar thermal cascade system were set up according to the mechanism model of each component. After system evaluation, parameter selection, preliminary calculation and scheme comparison, two representative typical schemes were determined. In one scheme, both steam Rankine cycle and Stirling cycle are used for power generation. Condensation water of the Rankine cycle is used to cool the hot end of the Stirling engines to recover the released heat. In the other scheme, multiple organic Rankine cycles are used for power generation. Condensation heat of upper cycle is absorbed by lower cycle for energy cascade utilization.
- (2) Mechanism models were established for the components of solar thermal power generation system. The mechanism mathematical models were developed according to the physical equations and operation features of the target object. The key components

in the system, such as collectors, steam generating system, steam turbine and Stirling engine, have been analyzed for detailed modeling. The mathematical model of each component is a model verified by classical theory or a large number of experimental data, which is the basic of a cascade solar thermal power generation system model. Heat loss models were established for the receivers of trough collector and dish collector. For Stirling engine, based on reasonable simplification and hypothesis, a model of the Stirling machine considered various losses and irreversibilities was developed. The component models using object-oriented method were developed in MATLAB. It makes full use of inheritance and polymorphism to ensure both independence and relevance of the components.

- (3) A solar thermal power generation system design software was designed and the cascade solar thermal generation system models were developed. System models of the selected cascade solar thermal thermal generation systems were established based on the model of each component in the systems. The object-oriented features of inheritance, combination and polymorphism were used for the model development. The variation rules and performance indexes of main parameters under the coupling of external and internal factors were studied. The change mechanism was studied and the calculation method of its performance characteristics was established. After component layout, parameter setting and environment selection, the thesis completed the system development of each system scheme, and finally developed the simulation system of cascade solar thermal generation based on MATLAB with the copyright of independent computer software. The system components are relatively independent, easy to replace or improve the component model; calculation results of the system model exist in all objects of the system, so that the key parameters of each component can be clearly and conveniently viewed.
- (4) Simulation and optimization of cascade solar thermal power generation system model were carried out. Based on the research of performance characteristics of cascade solar thermal power generation system, the system was optimized and the structure was rebuilt. In particular, by analyzing the steam generating system of the system, a staged heating method was proposed, which can reduce the temperature difference in the steam generating system during steam generation by changing the mass flow rate of the heat transfer oil and effectively reduce exergy loss during the process. It helps

to improve the efficiency of the whole system. Considering the features of the Stirling engines in the cascade system, five basic arrangements of Stirling engine array were summarized, and the differences of Stirling engine array efficiency and output power under various layouts were analyzed. The best arrangement of Stirling units was given under the condition of given fluid of cold and heat sources.

- (5) Operating parameters of cascade solar thermal power generation system were optimized. According to the specific structure of the program and operation mode, the appropriate stand-alone systems for comparative analysis was selected for performance comparison. Analysis of the influence of various parameters on the efficiency difference between cascade system and its corresponding stand-alone systems was conducted. The results show that cascade solar thermal power generation system has higher overall solar-to-electric conversion efficiency under certain parameter conditions than its corresponding independent system. Under the condition of direct normal irradiance of  $700 \text{ W/m}^2$  and dish collector outlet air temperature of  $800^\circ\text{C}$ , the proposed cascade solar thermal power generation system is 5.2% more efficient than its corresponding stand-alone system.
- (6) A solar thermal power generation test platform was built, and the relevant experimental work was carried out. Special experiment cases considering the features of solar irradiance were designed to investigate the impact of different factors on the system performance. The influences of solar irradiance, flow rate and inlet temperature of the working fluid on the performance of the collectors were investigated. The analysis of experimental data and simulation results shows that, under the relevant test conditions, the thermal efficiency of trough collectors is between 58% and 64%, and that of trough collectors is between 63% and 68%. The experiment also validated the established trough collector and dish collector models.

## 8.2 Innovations

- Usage of different types of collectors and different thermodynamic cycles in one cascade system is proposed in this research. In this way, the working characteristics of different types of solar collectors and thermal cycles can be effectively utilized to overcome the drawbacks of traditional solar thermal power systems. This may provide a new feasible technology for lower cost, higher efficiency, large-scale solar thermal power generation.
- An air-water heat exchanger is applied in the cascade system to increase the temperature of the main steam temperature of the Rankine cycle. This provides a new way to overcome the shortcoming of the upper temperature limit of heat transfer oil in traditional solar trough systems, which helps to achieve higher Rankine cycle efficiency.
- Condensate of Rankine cycle is used to cool the Stirling engine. Rejected heat of the Stirling cycle can be reused by Rankine cycle, which helps to improve the overall system efficiency.
- Multistage exergy loss reduction system is applied to reduce the temperature difference between oil and water in the steam generating system. The solar field can be divided into three independent sectors according to different states (vapor, vapor-liquid two phase, liquid) of water in the steam generating system. This also provides a new space for different types of solar collector technologies applied in different solar fields. For example, linear Fresnel reflectors or flat collectors can be applied for the preheating solar field to reduce costs; molten salt can be used as heat transfer fluid in the superheating solar field to increase the main steam temperature of the Rankine cycle.
- Influence of the arrangement of Stirling engine array in the cascade system is analyzed. In order to investigate the influence of connection types on SEA performance, five basic connection types of SEA were summarized according to the direction-irrelevant feature of Stirling engine. After analyzing different factors on the performance of SEA, it is found that given heating and cooling fluids, using serial flow is the best choice for the connection type of an SEA.

### 8.3 Outlooks

In this research, effective topologies of the proposed cascade system were designed, models of the systems developed based on the detailed component models, simulation of the cascade system and corresponding stand alone systems were carried out and the results were analyzed. However, there are many points valuable for further research.

- Muti-stage exergy loss reduction system deserves more attention for its application of different kinds of collectors.
- Series connection of different collectors, such as flat plate and parabolic trough collectors, needs to be further studied to reduce the cost of solar power system.
- Economical analysis of the cascade system is required for the implement of the technology.
- Stirling engines are required for the platform to investigate the cascade utilization of solar energy.

## Acknowledge

In 2004, I came to Huazhong University of Science and Technology as an undergraduate student. Now, I am over 30. The completion of the doctoral dissertation indicates that my student life here is coming to an end. Although I had discouraged days in the unforgivable life, when I staggering to leave the land that accomplished my grown up years, I am grateful for all the hardships and joys I have experienced. The full harvest of both academic and life will change my life journey.

You miss a place because you miss the people there. Special thanks for professor Huang Shuhong, I learned a lot during those years being with you. I have been deeply infected by your academic attitude, working spirit and personal charisma. Your unique academic insight and acute academic ideas always inspired me.

After he past away, I dreamed about my tutor several times, especially when I was depressed. Recalling your teachings and encouragements, I always re-establish my confidence to overcome the difficulties. Face to face learning is a collection of my memory. Professor's firm academic enthusiasm will continue to guide me.

Many thanks to the teachers who provide guidances and helps in these years. I offer my thanks to Professor Gao Wei, his elegant temperament and broad mind set up a good example for personal relationship and learning approaches. I would like to thank Associate Professor Zhang Yanping for urging me to study and write from time to time, paying close attention to the progress of the papers, and giving many timely wit directions. Special thanks for professor Inmaculada Arauzo, I am lucky enough to follow you to University of Zaragoza to open a new academic perspective. Your easy-going temper, warm attitude make my life in Spain warm and fulfilling. Your rigorous spirit and deep insight influenced me a lot. I also show my thanks to Teacher He and Yang, they concerned about me and helped me. The completion of my study comes with the generous guidance and encouragement of the teachers.

In the academic team, I was fortunate to meet Lv Fangming, Wang Jizhou. We learned a lot from each other and created precious memories. In the days with Rahul and Daniel, I improved my English communication ability and writing skills.

Finally, I thank my family for their understanding and support. I am grateful to my parents for their hard work and strong support. Thank you, my wife, after our daughter

# 华 中 科 技 大 学 博 士 学 位 论 文

---

Tongtong was born, you carried the burden of taking care of this little life. Thank you, Tongtong, your cleverness and cuteness are the flavors of my life and they always make me full of power.

Time to say goodbye. This will be a new starting point for my life. I will stay true to my mission, follow my heart, and manage a new life with gratitude and expectations.

Zhang Cheng

December 14, 2017

## Bibliography

- [1] Babaelahi M, Sayyaadi H. A new thermal model based on polytropic numerical simulation of Stirling engines. *Applied Energy*, 2015, 141:143 – 159.
- [2] MARTINI W R. Stirling engine design manual, 2nd edition. Technical report, Martini Engineering, Richland, WA (USA), 1983.
- [3] International Energy Agency (2014). [http://www.iea.org/publications/freepublications/publication/TechnologyRoadmapSolarPhotovoltaicEnergy\\_2014edition.pdf](http://www.iea.org/publications/freepublications/publication/TechnologyRoadmapSolarPhotovoltaicEnergy_2014edition.pdf). Accessed: 2017-05-04.
- [4] Price H, Lupfert E, Kearney D, et al. Advances in Parabolic Trough Solar Power Technology. *Journal of Solar Energy Engineering*, 2002, 124(2):109–125.
- [5] Dudley V E, Kolb G J, Mahoney A R, et al. Test results: SEGS LS-2 solar collector. Nasa Sti/recon Technical Report N, 1994, 96(4):2506–2514.
- [6] Burkholder F, Kutscher C. Heat Loss Testing of Schott's 2008 PTR70 Parabolic Trough Receiver. May, 2009.
- [7] Reddy K, Kumar K R, Ajay C. Experimental investigation of porous disc enhanced receiver for solar parabolic trough collector. *Renewable Energy*, 2015, 77(Supplement C):308 – 319.
- [8] Li M, Xu C, Ji X, et al. A new study on the end loss effect for parabolic trough solar collectors. *Energy*, 2015, 82(Supplement C):382 – 394.
- [9] Wang J, Wang J, Bi X, et al. Performance Simulation Comparison for Parabolic Trough Solar Collectors in China. *International Journal of Photoenergy*, 2016, 2016(18):1–16.
- [10] Zou B, Yang H, Yao Y, et al. A detailed study on the effects of sunshape and incident angle on the optical performance of parabolic trough solar collectors. *Applied Thermal Engineering*, 2017, 126(Supplement C):81 – 91.
- [11] Lüpfer E, Pottler K, Ulmer S, et al. Parabolic Trough Optical Performance Analysis Techniques. *Journal of Solar Energy Engineering*, 2006, 129(2):147–152.
- [12] Xu C, Chen Z, Li M, et al. Research on the compensation of the end loss effect for parabolic trough solar collectors. *Applied Energy*, 2014, 115:128 – 139.
- [13] Huang W, Hu P, Chen Z. Performance simulation of a parabolic trough solar collector. *Solar Energy*, 2012, 86(2):746 – 755.
- [14] Padilla R V, Fontalvo A, Demirkaya G, et al. Exergy analysis of parabolic trough solar receiver. *Applied Thermal Engineering*, 2014, 67(1-2):579 – 586.
- [15] Padilla R V, Demirkaya G, Goswami D Y, et al. Heat transfer analysis of parabolic trough solar receiver. *Applied Energy*, 2011, 88(12):5097 – 5110.
- [16] Guo J, Huai X, Liu Z. Performance investigation of parabolic trough solar receiver. *Applied Thermal Engineering*, 2016, 95:357 – 364.
- [17] Behar O, Khellaf A, Mohammedi K. A novel parabolic trough solar collector model – Vali-

- dation with experimental data and comparison to Engineering Equation Solver (EES). *Energy Conversion and Management*, 2015, 106(Supplement C):268 – 281.
- [18] Hachicha A, Rodriguez I, Capdevila R, et al. Heat transfer analysis and numerical simulation of a parabolic trough solar collector. *Applied Energy*, 2013, 111:581 – 592.
  - [19] Guo J, Huai X. Multi-parameter optimization design of parabolic trough solar receiver. *Applied Thermal Engineering*, 2016, 98:73 – 79.
  - [20] Boukelia T, Arslan O, Mecibah M. ANN-based optimization of a parabolic trough solar thermal power plant. *Applied Thermal Engineering*, 2016, 107:1210 – 1218.
  - [21] Liu Q, Yang M, Lei J, et al. Modeling and optimizing parabolic trough solar collector systems using the least squares support vector machine method. *Solar Energy*, 2012, 86(7):1973 – 1980.
  - [22] Lobon D H, Valenzuela L, Baglietto E. Modeling the dynamics of the multiphase fluid in the parabolic-trough solar steam generating systems. *Energy Conversion and Management*, 2014, 78:393 – 404.
  - [23] Mohamad A, Orfi J, Alansary H. Heat losses from parabolic trough solar collectors. *International Journal of Energy Research*, 2014, 38(1):20–28.
  - [24] Guo S, Liu D, Chu Y, et al. Real-time dynamic analysis for complete loop of direct steam generation solar trough collector. *Energy Conversion and Management*, 2016, 126:573 – 580.
  - [25] Ashouri M, Vandani A M K, Mehrpooya M, et al. Techno-economic assessment of a Kalina cycle driven by a parabolic Trough solar collector. *Energy Conversion and Management*, 2015, 105:1328 – 1339.
  - [26] Bader R, Pedretti A, Barbato M, et al. An air-based corrugated cavity-receiver for solar parabolic trough concentrators. *Applied Energy*, 2015, 138:337 – 345.
  - [27] Good P, Ambrosetti G, Pedretti A, et al. An array of coiled absorber tubes for solar trough concentrators operating with air at 600°C and above. *Solar Energy*, 2015, 111:378 – 395.
  - [28] Kaloudis E, Papanicolaou E, Belessiotis V. Numerical simulations of a parabolic trough solar collector with nanofluid using a two-phase model. *Renewable Energy*, 2016, 97:218 – 229.
  - [29] Al-Sulaiman F A, Hamdullahpur F, Dincer I. Performance assessment of a novel system using parabolic trough solar collectors for combined cooling, heating, and power production. *Renewable Energy*, 2012, 48:161 – 172.
  - [30] Tan Y, Zhao L, Bao J, et al. Experimental investigation on heat loss of semi-spherical cavity receiver. *Energy Conversion and Management*, 2014, 87(Supplement C):576 – 583.
  - [31] Chaudhary A, Kumar A, Yadav A. Experimental investigation of a solar cooker based on parabolic dish collector with phase change thermal storage unit in Indian climatic conditions. *Journal of Renewable and Sustainable Energy*, 2013, 5(2):023107.
  - [32] Mawire A, Taole S H. Experimental energy and exergy performance of a solar receiver for a domestic parabolic dish concentrator for teaching purposes. *Energy for Sustainable Development*, 2014, 19:162 – 169.
  - [33] Zhu J, Wang K, Wu H, et al. Experimental investigation on the energy and exergy performance of a coiled tube solar receiver. *Applied Energy*, 2015, 156:519 – 527.

- [34] Skouri S, Bouadila S, Salah M B, et al. Comparative study of different means of concentrated solar flux measurement of solar parabolic dish. *Energy Conversion and Management*, 2013, 76:1043 – 1052.
- [35] Thirunavukkarasu V, Sornanathan M, Cheralathan M. An experimental study on energy and exergy performance of a cavity receiver for solar parabolic dish concentrator. *International Journal of Exergy*, 2017, 23(2):129.
- [36] Pavlovic S, Bellos E, Roux W G L, et al. Experimental investigation and parametric analysis of a solar thermal dish collector with spiral absorber. *Applied Thermal Engineering*, 2017, 121(Supplement C):126 – 135.
- [37] Lovegrove K, Burgess G, Pye J. A new 500m<sup>2</sup> paraboloidal dish solar concentrator. *Solar Energy*, 2011, 85(4):620 – 626. SolarPACES 2009.
- [38] Berumen C R, Benítez R R, Mendoza J L, et al. Design and Construction of a Parabolic Dish in Mexico. in: *Proceedings of ASME 2004 International Solar Energy Conference*, 2004, 653-657.
- [39] PAVLOVIĆ S R, STEFANOVIĆ V P, SULJKOVIĆ S H. OPTICAL MODELING OF A SOLAR DISH THERMAL CONCENTRATOR BASED ON SQUARE FLAT FACETS. *Thermal Science*, 2014, 18(3):989 – 998.
- [40] Hijazi H, Mokhiamar O, Elsamni O. Mechanical design of a low cost parabolic solar dish concentrator. *Alexandria Engineering Journal*, 2016, 55(1):1 – 11.
- [41] Ma H, Jin G, Xing Z, et al. Optical Design of a Solar Dish Concentrator Based on Triangular Membrane Facets. *International Journal of Photoenergy*, 2012, 2012(2012):3109–3109.
- [42] Schertz P T, Brown D C, Konnerth I. Facet development for a faceted stretched-membrane dish by Solar Kinetics, Inc. *Parabolic Dish Collectors*, 1991, 91.
- [43] Shuai Y, Xia X, Tan H. Numerical simulation and experiment research of radiation performance in a dish solar collector system. *Frontiers of Energy & Power Engineering in China*, 2010, 4(4):488–495.
- [44] Qianjun M, Ming X, Yong S, et al. Study on solar photo-thermal conversion efficiency of a solar parabolic dish system. *Environmental Progress & Sustainable Energy*, 2014, 33(4):1438–1444.
- [45] Li Z, Tang D, Du J, et al. Study on the radiation flux and temperature distributions of the concentrator-receiver system in a solar dish/Stirling power facility. *Applied Thermal Engineering*, 2011, 31(10):1780 – 1789.
- [46] Wang W, Laumert B. Effect of cavity surface material on the concentrated solar flux distribution for an impinging receiver. *Solar Energy Materials and Solar Cells*, 2017, 161(Supplement C):177 – 182.
- [47] Blázquez R, Carballo J, Silva M. Optical design and optimization of parabolic dish solar concentrator with a cavity hybrid receiver. *AIP Conference Proceedings*, 2016, 1734(1).
- [48] Reddy K, Vikram T S, Veershetty G. Combined heat loss analysis of solar parabolic dish – modified cavity receiver for superheated steam generation. *Solar Energy*, 2015, 121:78 – 93. {ISES} Solar World Congress 2013 (SWC2013) Special Issue.

- [49] Vikram T S, Reddy K. Investigation of convective and radiative heat losses from modified cavity based solar dish steam generator using {ANN}. International Journal of Thermal Sciences, 2015, 87:19 – 30.
- [50] Patil P N, Khandekar M A, Patil S N. Automatic dual-axis solar tracking system for parabolic dish. in: Proceedings of 2016 2nd International Conference on Advances in Electrical, Electronics, Information, Communication and Bio-Informatics (AEEICB), Feb, 2016, 699-703.
- [51] Raturi M P, Deolal M H, Grover J, et al. Parabolic Dish Type Solar Cooking System with Gravity Based Solar Tracking System. 2014, 11(3):34–36.
- [52] Kuang J, Zhang W. Design and Implementation of Tracking System for Dish Solar Thermal Energy Based on Embedded System. Berlin, Heidelberg: Springer Berlin Heidelberg, 2012, pages 31–38.
- [53] Jin X, Xu G, Zhou R, et al. A Sun Tracking System Design for a Large Dish Solar Concentrator. International Journal of Clean Coal & Energy, 2013, 02(2):16–20.
- [54] Shanmugam S, Christraj W. The Tracking of the Sun for Solar Paraboloidal Dish Concentrators. Journal of Solar Energy Engineering, 2005, 127(1):156–160.
- [55] Alexopoulos S, Hoffschmidt B. Advances in solar tower technology. Wiley Interdisciplinary Reviews: Energy and Environment, 2017, 6(1):e217–n/a. E217.
- [56] Montes M, Abánades A, Martínez-Val J. Performance of a direct steam generation solar thermal power plant for electricity production as a function of the solar multiple. Solar Energy, 2009, 83(5):679 – 689.
- [57] Feldhoff J F, Schmitz K, Eck M, et al. Comparative system analysis of direct steam generation and synthetic oil parabolic trough power plants with integrated thermal storage. Solar Energy, 2012, 86(1):520 – 530.
- [58] Steinmann W D, Eck M. Buffer storage for direct steam generation. Solar Energy, 2006, 80(10):1277 – 1282. Solar Power and Chemical Energy Systems (SolarPACES'04).
- [59] Yu Q, Wang Z, Zhu L. Analysis and improvement of the cavity structure of steam receiver of 1MWe solar tower power plant. in: Proceedings of Solarpaces: International Conference on Concentrating Solar Power & Chemical Energy Systems, 2017, 164-174.
- [60] González-Roubaud E, Pérez-Osorio D, Prieto C. Review of commercial thermal energy storage in concentrated solar power plants: Steam vs. molten salts. Renewable and Sustainable Energy Reviews, 2017, 80(Supplement C):133 – 148.
- [61] Toro C, Rocco M V, Colombo E. Exergy and Thermo-economic Analyses of Central Receiver Concentrated Solar Plants Using Air as Heat Transfer Fluid. Energies, 2016, 9(11).
- [62] Roldán M I, Fernándezreche J. CFD analysis of supercritical CO<sub>2</sub> used as HTF in a solar tower receiver. in: Proceedings of Solarpaces: International Conference on Concentrating Solar Power & Chemical Energy Systems, 2016, 2293-2305.
- [63] Joshi A, Wang C, Akinjiola O, et al. Transient analysis of a molten salt central receiver (MSCR) in a solar power plant. 2016, 1734(1):578–592.
- [64] Thalange V C, Dalvi V H, Mahajani S M, et al. Design, optimization and optical performance study of tripod heliostat for solar power tower plant. Energy, 2017, 135(Supplement C):610 –

624.

- [65] Besarati S M, Yogi Goswami D. A computationally efficient method for the design of the heliostat field for solar power tower plant. *Renewable Energy*, 2014, 69:226–232.
- [66] Sassi G. Some notes on shadow and blockage effects. *Solar Energy*, 1983, 31(3):331 – 333.
- [67] Wei X, Lu Z, Wang Z, et al. A new method for the design of the heliostat field layout for solar tower power plant. *Renewable Energy*, 2010, 35(9):1970–1975.
- [68] Kim J, Kim J S, Stein W. Simplified heat loss model for central tower solar receiver. *Solar Energy*, 2015, 116:314 – 322.
- [69] Lara-Cerecedo L O, Moreno-Cruz I, Pitalúa-Díaz N, et al. Modeling of Drift Effects on Solar Tower Concentrated Flux Distributions. *International Journal of Photoenergy*, 2016, 2016:1–9.
- [70] Franchini G, Perdichizzi A, Ravelli S, et al. A comparative study between parabolic trough and solar tower technologies in Solar Rankine Cycle and Integrated Solar Combined Cycle plants. *Solar Energy*, 2013, 98, Part C:302 – 314.
- [71] Xu E, Yu Q, Wang Z, et al. Modeling and simulation of 1 MW DAHAN solar thermal power tower plant. *Renewable Energy*, 2011, 36(2):848–857.
- [72] Xu E, Wang Z, Wei G, et al. Dynamic simulation of thermal energy storage system of Badaling 1 MW solar power tower plant. *Renewable Energy*, 2012, 39(1):455–462.
- [73] Benammar S, Khellaf A, Mohammedi K. Contribution to the modeling and simulation of solar power tower plants using energy analysis. *Energy Conversion and Management*, 2014, 78(Supplement C):923 – 930.
- [74] Suzuki A. Cascade connection of solar collectors for effective energy gain. *Journal of Solar Energy Engineering Transactions of the Asme*, 1986, 108(3):172–177.
- [75] Kribus A, Doron P, Rubin R, et al. A Multistage Solar Receiver:: The Route To High Temperature. *Solar Energy*, 1999, 67(1–3):3 – 11.
- [76] Gordon J M, Saltiel C. Analysis and Optimization of a Multi-Stage Solar Collector System. *Journal of Solar Energy Engineering*, 1986, 108(3):192–198.
- [77] Oshida I, Suzuki A. Optical Cascade Heat-Collection for Effective Solar Energy Gain. *Journal of Solar Energy Engineering*, 1987, 109(4):298–302.
- [78] Desai N B, Bandyopadhyay S. Integration of parabolic trough and linear Fresnel collectors for optimum design of concentrating solar thermal power plant. *Clean Technologies and Environmental Policy*, 2015, 17(7):1945–1961.
- [79] Coco-Enríquez L, Muñoz-Antón J, Martínez-Val J. Integration between direct steam generation in linear solar collectors and supercritical carbon dioxide Brayton power cycles. *International Journal of Hydrogen Energy*, 2015, 40(44):15284 – 15300. The 4th International Conference on Nuclear and Renewable Energy Resources (NURER2014), 26-29 October 2014, Antalya, Turkey.
- [80] Li Y, Yang Y. Thermodynamic analysis of a novel integrated solar combined cycle. *Applied Energy*, 2014, 122:133 – 142.
- [81] Gülen S C. Second Law Analysis of Integrated Solar Combined Cycle Power Plants. *Journal*

- of Engineering for Gas Turbines and Power, 2015, 137(5):51701.
- [82] Shaaban S. Analysis of an integrated solar combined cycle with steam and organic Rankine cycles as bottoming cycles. *Energy Conversion and Management*, 2016, 126:1003–1012.
  - [83] Alqahtani B J, Patiño-Echeverri D. Integrated Solar Combined Cycle Power Plants: Paving the way for thermal solar. *Applied Energy*, 2016, 169:927 – 936.
  - [84] Manente G. High performance integrated solar combined cycles with minimum modifications to the combined cycle power plant design. *Energy Conversion and Management*, 2016, 111:186 – 197.
  - [85] Turchi C S, Ma Z. Co-located gas turbine/solar thermal hybrid designs for power production. *Renewable Energy*, 2014, 64:172 – 179.
  - [86] Mukhopadhyay S, Ghosh S. Solar tower combined cycle plant with thermal storage: energy and exergy analyses. *Advances in Energy Research*, 2016, 4(1):29–45.
  - [87] Li J, Li P, Pei G, et al. Analysis of a novel solar electricity generation system using cascade Rankine cycle and steam screw expander. *Applied Energy*, 2016, 165:627–638.
  - [88] Al-Sulaiman F A. Exergy analysis of parabolic trough solar collectors integrated with combined steam and organic Rankine cycles. *Energy Conversion and Management*, 2014, 77:441 – 449.
  - [89] Dunham M T, Lipiński W. Thermodynamic Analyses of Single Brayton and Combined Brayton–Rankine Cycles for Distributed Solar Thermal Power Generation. *Journal of Solar Energy Engineering*, 2013, 135(3):031008–031008–8.
  - [90] Bahrami M, Hamidi A A, Porkhial S. Investigation of the effect of organic working fluids on thermodynamic performance of combined cycle Stirling-ORC. *International Journal of Energy and Environmental Engineering*, 2013, 4(1):12.
  - [91] Thierry D M, Flores-Tlacuahuac A, Grossmann I E. Simultaneous optimal design of multi-stage organic Rankine cycles and working fluid mixtures for low-temperature heat sources. *Computers & Chemical Engineering*, 2016, 89:106 – 126.
  - [92] Bahari S S, Sameti M, Ahmadi M H, et al. Optimisation of a combined Stirling cycle–organic Rankine cycle using a genetic algorithm. *International Journal of Ambient Energy*, 2016, 37(4):398–402.
  - [93] Abbin J, Leuenberger W. Program CYCLE: a Rankine cycle analysis routine. [For solar-thermal electricity production for Sandia's Solar Community study]. Oct, 1977.
  - [94] Montes M, Rovira A, Muñoz M, et al. Performance analysis of an Integrated Solar Combined Cycle using Direct Steam Generation in parabolic trough collectors. *Applied Energy*, 2011, 88(9):3228 – 3238.
  - [95] Elsafi A M. Exergy and exergoeconomic analysis of sustainable direct steam generation solar power plants. *Energy Conversion and Management*, 2015, 103(Supplement C):338 – 347.
  - [96] Fraidenraich N, Oliveira C, Cunha A F V, et al. Analytical modeling of direct steam generation solar power plants. *Solar Energy*, 2013, 98(Part C):511 – 522.
  - [97] Roschke E J, Wen L, Steele H, et al. A preliminary assessment of small steam Rankine and Brayton point-focusing solar modules. *Nasa Sti/recon Technical Report N*, 1979, 79.

- [98] Bao J, Zhao L. A review of working fluid and expander selections for organic Rankine cycle. *Renewable and Sustainable Energy Reviews*, 2013, 24:325 – 342.
- [99] Bilgen E, Rheault J. Solar chimney power plants for high latitudes. *Solar Energy*, 2005, 79(5):449 – 458.
- [100] Good P, Ambrosetti G, Pedretti A, et al. A 1.2MWth solar parabolic trough system based on air as heat transfer fluid at 500 °C — Engineering design, modelling, construction, and testing. *Solar Energy*, 2016, 139(Supplement C):398 – 411.
- [101] Fernández-García A, Zarza E, Valenzuela L, et al. Parabolic-trough solar collectors and their applications. *Renewable and Sustainable Energy Reviews*, 2010, 14(7):1695 – 1721.
- [102] Giglio A, Lanzini A, Leone P, et al. Direct steam generation in parabolic-trough collectors: A review about the technology and a thermo-economic analysis of a hybrid system. *Renewable and Sustainable Energy Reviews*, 2017, 74:453–473.
- [103] Khenissi A, Krüger D, Hirsch T, et al. Return of Experience on Transient Behavior at the DSG Solar Thermal Power Plant in Kanchanaburi, Thailand. *Energy Procedia*, 2015, 69:1603 – 1612. International Conference on Concentrating Solar Power and Chemical Energy Systems, SolarPACES 2014.
- [104] Romero-Alvarez M, Zarza E. Concentrating solar thermal power. Efficiency and Renewable Energy, 2007.
- [105] Adkins D R. Control strategies and hardware used in solar thermal applications. Nasa Sti/recon Technical Report N, 1987, 88.
- [106] Coronel P, Sandeep K. Heat transfer coefficient in helical heat exchangers under turbulent flow conditions. *International Journal of Food Engineering*, 2008, 4(1).
- [107] Serth R W. Process heat transfer principles and applications. Amsterdam; London: Elsevier Academic Press, 2007.
- [108] Churchill S W, Bernstein M. A Correlating Equation for Forced Convection From Gases and Liquids to a Circular Cylinder in Crossflow. *Journal of Heat Transfer*, 1977, 99(2):300–306.
- [109] Ma R Y. Wind Effects on Convective Heat Loss From a Cavity Receiver for a Parabolic Concentrating Solar Collector. Sandia National Laboratory, 1993, SAND92-7293(September).
- [110] Wu S Y, Xiao L, Cao Y, et al. Convection heat loss from cavity receiver in parabolic dish solar thermal power system: A review. *Solar Energy*, 2010, 84(8):1342 – 1355.
- [111] Leibfried U, Ortjohann J. Convective Heat Loss from Upward and Downward-Facing Cavity Solar Receivers: Measurements and Calculations. *Journal of Solar Energy Engineering*, 1995, 117(2):75–84.
- [112] Koenig A, Marvin M. Convection heat loss sensitivity in open cavity solar receivers. Technical report, Department of Energy, USA, 1981.
- [113] Stine W B, Diver R B. A compendium of solar dish/Stirling technology. Technical report, DTIC Document, 1994.
- [114] Formosa F, Despesse G. Analytical model for Stirling cycle machine design. *Energy Conversion and Management*, 2010, 51(10):1855–1863.

- [115] Juhasz A. A mass computation model for lightweight brayton cycle regenerator heat exchangers. in: Proceedings of 8th Annual International Energy Conversion Engineering Conference, 2010.
- [116] Duan C, Wang X, Shu S, et al. Thermodynamic design of Stirling engine using multi-objective particle swarm optimization algorithm. *Energy Conversion & Management*, 2014, 84:88–96.
- [117] Urieli I, Berchowitz D M. Stirling cycle engine analysis. Bristol: A. Hilger, 1984.
- [118] Heywood, JohnB. Internal combustion engine fundamentals. Amsterdam; London: McGraw-Hill, 1988.
- [119] Strauss J M, Dobson R T. Evaluation of a second order simulation for Sterling engine design and optimisation. *Journal of Energy in Southern Africa*, 2010, 21(2):17–29.
- [120] Timoumi Y, Tlili I, Nasrallah S B. Design and performance optimization of GPU-3 Stirling engines. *Energy*, 2008, 33(7):1100 – 1114.
- [121] Hosseinzade H, Sayyaadi H, Babaelahi M. A new closed-form analytical thermal model for simulating Stirling engines based on polytropic-finite speed thermodynamics. *Energy Conversion and Management*, 2015, 90:395 – 408.
- [122] Der Minassians A. Stirling Engines for Low-temperature Solar-thermal-electric Power Generation: [PhD Dissertation]. Berkeley: EECS Department, University of California, Berkeley, December 20, 2007.
- [123] Cavazzuti M. Optimization Methods: From Theory to Design Scientific and Technological Aspects in Mechanics. Berlin Heidelberg: Springer, 2012.
- [124] Hooshang M, Moghadam R A, AlizadehNia S. Dynamic response simulation and experiment for gamma-type Stirling engine. *Renewable Energy*, 2016, 86:192 – 205.
- [125] Fraser P, Klein P S a. Stirling Dish System Performance Prediction Model. Mechanical Engineering, 2008, Master of:203.

## Appendix A Heat transfer under constant temperature

Assuming  $U, T_c, \dot{m}, c_p$  to be constant, for given  $T_i$ ,

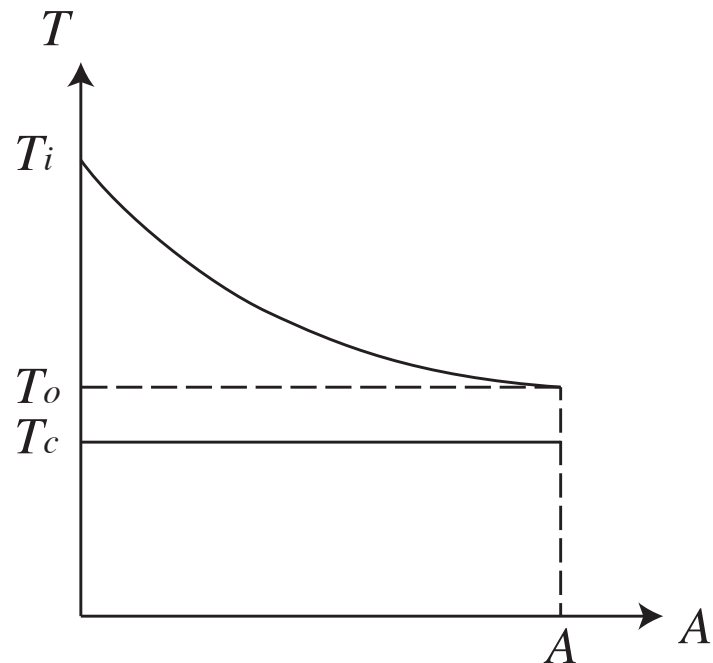


Figure 1-1 Diagram of heat transfer under constant temperature

For  $A(x) = Px$ ,  $x$  from 0 to  $L$ , while  $T(x)$  from  $T_i$  to  $T_o$ ,

$$\dot{m}c_p dT(x) = (T_c - T(x))UPdx \quad (\text{A.1})$$

so

$$\frac{dT(x)}{dx} = -\frac{UP}{\dot{m}c_p}(T(x) - T_c) \quad (\text{A.2})$$

$$T_g(x) = T_p(x) + T_h(x) \quad (\text{A.3})$$

where  $T_g(x)$  is the general solution,  $T_p(x)$  is the particular solution,  $T_h(x)$  is the homogeneous solution.

$$-\frac{UP}{\dot{m}c_p}(T_p(x) - T_c) = 0 \quad (\text{A.4})$$

$$T_p(x) = T_c \quad (\text{A.5})$$

$$\frac{dT_h(x)}{dx} = -\frac{UP}{\dot{m}c_p}T_h(x) \quad (\text{A.6})$$

$$\int_{T_h(x)=T_h(0)}^{T_h(x)=T_h(L)} \frac{dT_h(x)}{T_h(x)} = - \int_{x=0}^{x=L} \frac{UP}{\dot{m}c_p} dx \quad (\text{A.7})$$

$$\frac{T_h(L)}{T_h(0)} = \exp\left(-\frac{UPL}{\dot{m}c_p}\right) \quad (\text{A.8})$$

that is

$$\frac{T_g(L) - T_p(L)}{T_g(0) - T_p(0)} = \exp\left(-\frac{UA}{\dot{m}c_p}\right) \quad (\text{A.9})$$

$$\frac{T_o - T_c}{T_i - T_c} = \exp\left(-\frac{UA}{\dot{m}c_p}\right) \quad (\text{A.10})$$

## Appendix B Thermal gradient under constant heat flux

Assuming  $U, T_c, \dot{m}, c_p, q''$  to be constant, for given  $T_i$ ,

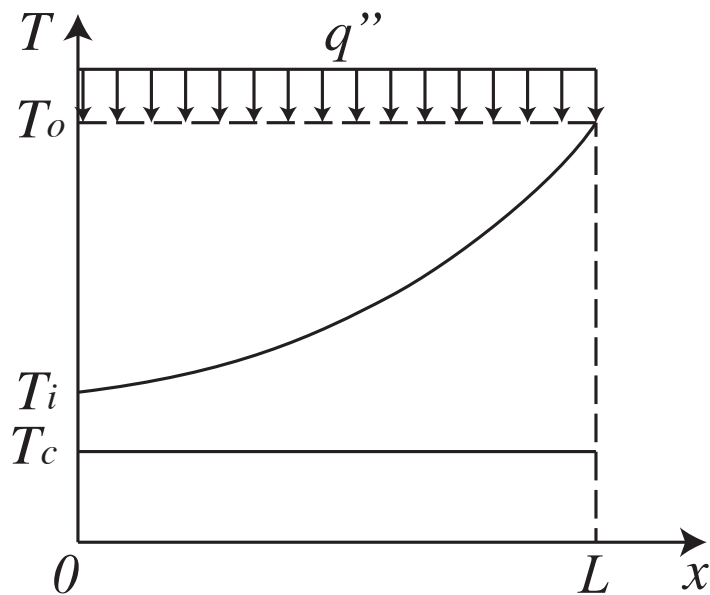


Figure 2-1 Diagram of heat transfer with one constant temperature heat source and constant heat flux

For  $A(x) = Px$ ,  $x$  from 0 to  $L$ , while  $T(x)$  from  $T_i$  to  $T_o$ ,

$$\dot{m}c_p dT(x) = (T_c - T(x))UPdx + q''Pdx \quad (\text{B.1})$$

so

$$\frac{dT(x)}{dx} = -\frac{UP}{\dot{m}c_p}T(x) + \frac{q''P + UPT_c}{\dot{m}c_p} \quad (\text{B.2})$$

$$T_g(x) = T_p(x) + T_h(x) \quad (\text{B.3})$$

where  $T_g(x)$  is the general solution,  $T_p(x)$  is the particular solution,  $T_h(x)$  is the homogeneous solution.

$$-\frac{UP}{\dot{m}c_p}T_p(x) + \frac{q''P + UPT_c}{\dot{m}c_p} = 0 \quad (\text{B.4})$$

$$T_p(x) = T_c + \frac{q''}{U} \quad (\text{B.5})$$

$$\frac{dT_h(x)}{dx} = -\frac{UP}{\dot{m}c_p}T_h(x) \quad (\text{B.6})$$

the same as Equation (A.6), so we have

$$\frac{T_g(L) - T_p(L)}{T_g(0) - T_p(0)} = \exp\left(-\frac{UA}{\dot{m}c_p}\right) \quad (\text{B.7})$$

$$\frac{T_o - T_c - \frac{q''}{U}}{T_i - T_c - \frac{q''}{U}} = \exp\left(-\frac{UA}{\dot{m}c_p}\right) \quad (\text{B.8})$$

## Appendix C MATLAB code of class Stream

```

1 classdef Stream < handle
2     %Stream This class describes a fluid stream that has inherent
3     %properties and dependent properties
4
5     properties
6         fluid;    % Fluid type
7         dot_m;   % Mass flow rate, kg/s
8         T;       % Temperature, K
9         p;       % Pressure, Pa
10        x;      % Quality, [0, 1] for two phase stream; NaN for single
11                % phase stream
12    end
13    properties(Dependent)
14        h;        % Mass specific enthalpy, J.kg
15        s;        % Mass specific entropy, J/kg-K
16        cp;      % Specific heat under constant pressure, J/kg-K
17    end
18
19    methods
20        function obj = Stream
21            obj.T = Temperature;
22            obj.dot_m = Massflow;
23            obj.p = Pressure;
24        end
25        function flowTo(obj, st)
26            st.fluid = obj.fluid;
27            st.dot_m = obj.dot_m;
28        end
29        function st2 = mix(obj, st1)
30            % Get the properties of a stream mixed by two streams
31            % The two streams must have the same fluid type and pressure
32            if obj.fluid == st1.fluid
33                if obj.p.v == st1.p.v
34                    obj.p = st1.p;
35                    st2.fluid = obj.fluid;
36                    st2.p = obj.p;
37                    st2.dot_m.v = obj.dot_m.v + st1.dot_m.v;
38                    h = (obj.dot_m.v .* obj.h + st1.dot_m.v .* st1.h)...
39                        ./ (obj.dot_m.v + st1.dot_m.v);
40                    st2.T.v = CoolProp.PropsSI('T', 'H', h, 'P', st2.p.v);
41                else
42                    error('The two streams have different pressures!');
43                end
44            else

```

```

45         error('The two streams have different fluid types!');
46     end
47 end
48 function convergeTo(obj, st, y)
49     % Get another stream converged (or diverged)
50     % from the original stream state.
51     % If y < 1, the original stream is diverged
52     % If y > 1, the original stream is converged
53     st.fluid = obj.fluid;
54     st.T = obj.T;
55     st.p = obj.p;
56     st.x = obj.x;
57     st.dot_m.v = obj.dot_m.v .* y;
58 end
59 end
60 methods
61     % The dependent properties can be obtained from the inherent
62     % properties
63     % If x is NaN, then the dependent properties are determined
64     % by T and P; otherwise, they are determined by P and x
65     function value = get.h(obj)
66         if isempty(obj.x)
67             value = CoolProp.PropsSI('H', 'T', obj.T.v, ...
68                                     'P', obj.p.v, obj.fluid);
69         else
70             value = CoolProp.PropsSI('H', 'P', obj.p.v, 'Q', ...
71                                     obj.x, obj.fluid);
72         end
73     end
74     function value = get.s(obj)
75         if isempty(obj.x)
76             value = CoolProp.PropsSI('S', 'T', obj.T.v, ...
77                                     'P', obj.p.v, obj.fluid);
78         else
79             value = CoolProp.PropsSI('S', 'P', obj.p.v, 'Q', ...
80                                     obj.x, obj.fluid);
81         end
82     end
83     function value = get.cp(obj)
84         if isempty(obj.x)
85             value = CoolProp.PropsSI('C', 'T', obj.T.v, ...
86                                     'P', obj.p.v, obj.fluid);
87         else
88             value = inf;
89         end
90     end
91 end
92 end

```

## Appendix D Publication

- [1] Cheng Zhang, Yanping Zhang, Inmaculada Arauzo, Wei Gao, Chongzhe Zou. Cascade system using both trough system and dish system for power generation. *Energy Conversion and Management*. 2017.06.15;142:494–503.
- [2] Cheng Zhang, Yanping Zhang, Xiaolin Lei, Wei Gao. Design and Comparison of Solar Thermal Oilfield Steam Production System Plans. *Journal of Solar Energy Engineering*. 2017.01.08;139;004502-4.
- [3] Cheng Zhang, Kun Wang, Jizhou Wang, Shuhong Huang. FEA simulation on the alignment of the shafts of three-fulcrum turbine. *International Conference on Power Engineering*. 2013.
- [4] Chongzhe Zou, Yanping Zhang, Quentin Falcoz, Pierre Neveu, Cheng Zhang, Shuhong Huang, Weicheng Shu. Design and Optimization of a High-temperature Cavity Receiver for a Solar Energy Cascade Utilization System. *Renewable Energy*. 2017.04.01:103; 478-89.
- [5] Chongzhe Zou, Yanping Zhang, Huayi Feng, Quentin Falcoz, Pierre Neveu, Cheng Zhang, Wei Gao. “Effects of Geometrical Parameters on Thermal Performance for a Cylindrical Solar Receiver Using 3D numerical Model.” *Energy Conversion and Management*, 2017.10.1: 126-17.
- [6] Chongzhe Zou, Yanping Zhang, Quentin Falcoz, Pierre Neveu, Cheng Zhang. Thermal modeling of a pressurized air cavity receiver for solar dish Stirling system, Solarpaces: International Conference on Concentrating Solar Power & Chemical Energy Systems. AIP Publishing LLC, 2017:1884-1892.
- [7] A solar thermal cascade system, No. 201610806296.5
- [8] A flow control method used in a multistage heating system, No. 201610805604.2